

University of Nebraska - Lincoln

DigitalCommons@University of Nebraska - Lincoln

Civil Engineering Theses, Dissertations, and
Student Research

Civil Engineering

7-2016

CFD STUDY OF DECAY FUNCTION OF WALL SHEAR STRESS WITH SCOUR AROUND COMPLEX-SHAPE BRIDGE PIER

Chen Li

University of Nebraska, cli01@unomaha.edu

Follow this and additional works at: <http://digitalcommons.unl.edu/civilengdiss>



Part of the [Civil Engineering Commons](#)

Li, Chen, "CFD STUDY OF DECAY FUNCTION OF WALL SHEAR STRESS WITH SCOUR AROUND COMPLEX-SHAPE BRIDGE PIER" (2016). *Civil Engineering Theses, Dissertations, and Student Research*. 94.

<http://digitalcommons.unl.edu/civilengdiss/94>

This Article is brought to you for free and open access by the Civil Engineering at DigitalCommons@University of Nebraska - Lincoln. It has been accepted for inclusion in Civil Engineering Theses, Dissertations, and Student Research by an authorized administrator of DigitalCommons@University of Nebraska - Lincoln.

CFD STUDY OF DECAY FUNCTION OF WALL SHEAR STRESS WITH SCOUR
AROUND COMPLEX-SHAPE BRIDGE PIER

by

Chen Li

A DISSERTATION

Presented to the Faculty of
The Graduate College at the University of Nebraska
In Partial Fulfillment of Requirements
For the Degree of Doctor of Philosophy

Major: Engineering

Under the Supervision of Professor Junke Guo

Lincoln, Nebraska

July, 2016

CFD STUDY OF DECAY FUNCTION OF WALL SHEAR STRESS WITH SCOUR
AROUND COMPLEX-SHAPE BRIDGE PIER

Chen Li, Ph.D.

University of Nebraska, 2016

Advisor: Junke Guo

Pier scour problem is close related to the safety of bridges. The Federal Highway Administration of the United State also has a great interest in studying the relation between hydraulic loadings and scour depth. The current technological problem of directly measuring hydraulic loadings on a dynamic bed using physical experiments and the weak capacity to simulate the real scour processes with CFD methods inspired the development of a hybrid approach by combining them to study pier scour.

This research specifically focuses on the CFD part of the hybrid method. A series of three-dimensional (3-D) CFD models were developed with unsteady Reynolds Averaged Navier-Stokes equations and the $k-\epsilon$ turbulence model to calculate wall shear stress distributions around piers under different kinds of flow conditions. These CFD models were verified and calibrated by comparing wall shear stress distributions with other CFD simulations, which use a DES turbulence model.

The CFD simulation results were applied to develop a decay function of dimensionless wall shear stress with relative scour depth. Combined with the previous physical experimental data, the decay function was updated to be an envelope function to

more accurately describe the decay trend. The results of CFD modeling for water flows around a rectangular pier with a 30° attack of angle were used to verify the decay function and the envelope function.

With surveyed full-scale bathymetries of the Feather River Bridge, this hybrid approach and the decay function were applied to study the pier scour problem. The decay trend and the envelope decay function were verified with the results of CFD modeling for the full-scale models. Using the soil composition of each layer, the application of the decay function was preliminarily developed.

To

My Parents

for their love, understanding and support

Acknowledgements

I would like to express my thanks to the following people, who helped and supported me to finish my research.

First, I want to thank my advisor Prof. Junke Guo. He used his invaluable knowledge, research skills and rich experience to instruct me in the past four years. His strict requirements, positive encourage and detailed guidance benefit me a lot in the period of the dissertation writing.

Second, I want to thank Mr. Oscar Suaznabar, a researcher of FHAW hydraulic laboratory. His excellent work on the physical experiment makes it possible to develop a hybrid approach to study pier scour and creates accurate surveyed bathymetries models for my studies. I am glad to thank Dr. Zhaoding Xie, a researcher of FHAW hydraulic laboratory. He selflessly shares his CFD experience with me and patiently helps me to learn STAR-CCM+.

I also appreciate, Dr. Kornel Kerenyi, Research Manager of FHWA Hydraulics R&D for providing me the right to access to the hydraulic laboratory at Transportation Research and Analysis Computing Center (TRACC). The previous physical experimental data provided by him takes a significant place in this research. I also thank Dr. Steven A.Lottes for allowing me to access the supercomputing facility at Argonne National Laboratory (ANL) to conduct the expensive CFD computation. His guidance and suggestions help me gain enough CFD knowledge to conduct this research.

I also want to thank all members of my graduate committee: Dr. David Admiraal, Dr. Yusong Li, Dr. Yaoqing Yang and Dr. Jingying Zhu for their support, suggestion and

encourage. In addition, I would like to thank Dr. Jerry Shen, Dr. Haoyin Shan, Dr. Chao Huang and Mr. Zhengyang Cheng for their help and suggestions.

Finally, I want to thank my parents. Their encouragement and support are my inexhaustible energy source to overcome all difficulties and reach who I am today.

Table of Contents

List of Figures	xii
List of Tables	xv
List of Abbreviations	xvii
 CHAPTER 1 Introduction	 1
1.1 Overview	1
1.2 Introduction of Bridge Safety and Scour	1
1.3 Development of A Computational Fluid Dynamics Method and Introduction of STAR-CCM+	6
1.4 Research Background	8
1.5 Objectives of Research	12
1.6 Dissertation Outline	13
 CHAPTER 2 Literature Review	 15
2.1 Overview	15
2.2 Pier Scour	15
2.3 Critical Shear Stress	16
2.4 Boundary Flow	18
2.5 Decay Function of Hydraulic Loading	19

2.6 CFD Modeling for Open Channel Flow	21
CHAPTER 3 Description of Physical Experiments	29
3.1 Overview	29
3.2 Physical Models	29
3.2.1 Physical Experiment Devices	30
3.2.2 Scaled Flow Conditions	32
3.2.3 Additional Information	33
3.3 Physical Experimental Results.....	36
3.4 Summary	39
CHAPTER 4 Development of the CFD models	40
4.1 Overview.....	40
4.2 CFD Geometry	41
4.2.1 Approaches to Modify Original CAD Models.....	42
4.2.2 Influence of Perturbations.....	46
4.3 Mesh.....	50
4.4 Physical Models	53
4.5 Necessary Setup	56
4.6 Validation and Calibration of CFD Models.....	59
4.6.1 Influence of Size of Mesh Cell	59
4.6.2 Quasi-Steady State	67

4.6.3 Validation and Calibration of CFD Models.....	71
4.7 Summary.....	76
CHAPTER 5 Development of Decay Function of Wall Shear Stress	77
5.1 Overview.....	77
5.2 Development of Decay Function of Wall Shear stress	77
5.2.1 Wall Shear Stress Distributions	78
5.2.2 Decay Function	90
5.3 Calibration of the Decay Function.....	93
5.3.1 Approach to Calculate Potential maximum Scour Depth	93
5.3.2 Envelope Decay Function	96
5.4 Validation of the Decay Function.....	98
5.5 Summary.....	100
CHAPTER 6 Preliminary CFD Study of Pier Scour of the Feather River Bridge	101
6.1 Overview.....	101
6.2 Development of CFD Models.....	101
6.2.1 Geometry.....	102
6.2.2 Mesh.....	106
6.2.3 Flow Conditions, Physical models and Necessary Setup	111
6.3 CFD Simulation Results	113
6.3.1 Physical Time.....	113
6.3.2 Wall Shear Stress Distributions	115

6.4 Application of Decay Function of Wall Shear Stress	122
6.4.1 Validation of Decay Function	122
6.4.2 Applications of the Decay Function	126
6.5 Summary	131
Chapter 7 Conclusion and Future Work	132
7.1 Overview	132
7.2 Conclusions	132
7.2.1 CFD Modeling for Physical Experiments	133
7.2.2 Decay Function and Envelope Function	133
7.2.3 CFD modeling for full-scale Feather River Bridge	134
7.3 Limitations	135
7.4 Future Work	135
References:	137
APPENDIX A. Scour Bathymetries around Piers	146
APPENDIX B. Wall Shear Stress Distribution of Cases of the Physical Experiment ...	159
Glossary	172

List of Figures

Figure 1.1 Relative contributions of factors of bridge failure (Annandale, 1993).....	2
Figure 1.2 Schoharie Creek Bridge, New York, failed by bridge pier scour in glacial till in 1987 (National Transportation Safety Board, 1988)	3
Figure 1.3 Hydraulic loading decay function (Suaznabar et al., 2014).....	5
Figure 1.4 Cross-sections of Feather River surveyed in 2007 and March 2011	9
Figure 1.5 Geometries of the original Pier and the retrofitted pier	11
Figure 2.1 Flow at the boundary	18
Figure 2.2 An illustration of CFD simulation by using VOF.....	23
Figure 2.3 Differences between DNS and LES	25
Figure 2.4 Contour of the instantaneous vorticity magnitude (Squires, 2004).....	27
Figure 3.1 Tilting flume in FHWA hydraulic laboratory (http://www.fhwa.dot.gov/publications/research/infrastructure/hydraulics/12022/004.cfm).....	30
Figure 3.2 Point laser distance sensor	31
Figure 3.3 Comparison between Feather River and experimental scour hole shapes.....	36
Figure 3.4 Original CAD models of MF_O	38
Figure 4.1 Procedure of development of CFD model in STAR-CCM+	41
Figure 4.2 Bathymetries of an original CAD model and its final CFD geometry.....	43
Figure 4.3 Bathymetries of an initial CAD model and its extruder mesh result.....	44
Figure 4.4 Final CFD geometry of Case Q100_O_50	45
Figure 4.5 Meshes of the flat bed with and without perturbations	47
Figure 4.6 Location of the plane and state of the free surface	48

Figure 4.7 Velocity distributions on the plane	49
Figure 4.8 Volumetric controls of Case MF_O_50	52
Figure 4.9 Mesh of Case MF_O_50	53
Figure 4.10 Physical continua models	54
Figure 4.11 Initialize solution for the Case Q100_O_50.....	57
Figure 4.12 Coarse mesh	62
Figure 4.13 Fine mesh and very fine mesh.....	63
Figure 4.14 Wall shear stress distributions of these two cases	65
Figure 4.15 Mesh of the case MF_O_75.....	66
Figure 4.16 Wall shear stress distribution of Case Q100_R_0.....	67
Figure 4.17 Wall shear stress distributions of Case Q100_R_50.....	69
Figure 4.18 Bathymetries around the rectangle pier	72
Figure 4.19 Wall shear stress distributions (RANS)	74
Figure 4.20 Wall shear stress distributions (DES).....	75
Figure 5.1 Wall shear stress distributions of MF_O.....	79
Figure 5.2 Decay Trend of wall shear stress of Group MF_O.....	83
Figure 5.3 Geometries and wall shear stress distributions of cases in Group MF_R.....	85
Figure 5.4 Decay trends of MF_O and MF_R	87
Figure 5.5 Wall shear stress distributions of MF_O and MF_R	88
Figure 5.6 Wall shear stress distributions of Q100_O and Q100_R.....	89
Figure 5.7 Decay function of wall shear stress	92
Figure 5.8 Common shapes of pier noses	94
Figure 5.9 Shear stress amplification vs relative depth.....	97

Figure 5.10 Decay function of wall shear stress of Annandale data and CFD data.....	98
Figure 5.11 CFD data of rectangular pier with Annandale data and CFD data	99
Figure 6.1 Original CAD model of B2011	103
Figure 6.2 Final CFD geometry of B2011	104
Figure 6.3 Bathymetries of B2007 and B2011.....	105
Figure 6.4 Final geometry of O_B2011_MF	105
Figure 6.5 Core area of CFD model	107
Figure 6.6 Volumetric Controls	108
Figure 6.7 Mesh of Case O_B2011_MF	109
Figure 6.8 Comparison of different wall functions.....	111
Figure 6.9 Initial free surface.....	112
Figure 6.10 Wall shear stress distributions around Pier 22 at different moments.....	114
Figure 6.11 Wall shear stress distribution of Case O_B2007_MF.....	116
Figure 6.12 Wall shear stress distributions of O_B2007_MF and O_B2011_MF.....	118
Figure 6.13 Wall shear stress distributions of O_B2007_MF and O_B2007_Q100.....	119
Figure 6.14 Wall shear stress distribution of O_B2007_MF and R_B2007_MF.....	121
Figure 6.15 Validation of decay function	126
Figure 6.16 Erodibility of the soil at Pier 22	130
Figure 6.17 Erodibility of the soil at Pier 22 in the emergency study.....	130

List of Tables

Table 1.1 Flow conditions.....	10
Table 3.1 Flow conditions.....	33
Table 3.2 Physical experiment cases	35
Table 4.1 Boundary conditions.....	45
Table 4.2 User field defined for the initial flow condition	56
Table 4.3 User fields defined for wall shear stress	58
Table 4.4 Estimation of wall distance.....	61
Table 4.5 Number of mesh cells	61
Table 4.6 Maximum RMS of wall shear stress of MF_O.....	71
Table 5.1 Hydraulic radiuses of MF and Q100.....	81
Table 5.2 Wall shear stress data of MF_O.....	82
Table 5.3 Wall shear stress data of MF_R.....	84
Table 5.4 Wall shear Stress Data	90
Table 5.5 K1 values of some common pier nodes	94
Table 5.6 K3 values	95
Table 6.1 CFD models of full-scale Feather River Bridge.....	102
Table 6.2 Boundary conditions.....	106
Table 6.3 Estimation of wall distance.....	109
Table 6.4 Flow conditions.....	112
Table 6.5 User defined function of CFD models of full-scale Feather River Bridge.....	113
Table 6.6 Wall shear stress data.....	123
Table 6.7 Manning n of sand	124

Table 6.8 Approach wall shear stress	125
Table 6.9 Wall shear stress amplification and relative scour depth.....	125
Table 6.10 Erodibility of the soil at Pier 22.....	127
Table 6.11 Estimated local wall shear stress with the envelope function.....	128

List of Abbreviations

2-D: Two-dimensional;

3-D: Three-dimensional;

CAD: Computer Aided Design;

CISS: Cast-in-Steel-Shell;

DES: Detached Eddy Simulation;

CFD: Computational Fluid Dynamics;

DNS: Directly Numerical Simulation;

FHWA: Federal Highway Administration;

FLIC: Fluid-In-Cell;

FVM: Finite Volume Method;

LES: Large Eddy Simulation;

MAC: Marker-And-Cell;

PIC: Particle-In-Cell;

RANS: Reynolds-Average Navier-Stokes;

uRANS: unsteady Reynolds-Average Navier-Stokes;

TFHRC: Turner-Fairbank Highway Research Center;

VOF: Volume of Fluid;

WSEL: Water Surface Elevation;

CHAPTER 1 Introduction

1.1 Overview

The primary purpose of this research is to develop a hybrid approach by combining physical experimental methods and computational fluid dynamics methods (CFD) to study scour around complex-shaped piers. Based on the results of hydraulic loadings of the developed hybrid method, the relation between hydraulic loadings (wall shear stress) and scour (scour depth) is developed and applied to study the pier scour of the Feather River Bridge. In this Chapter, the significance of scour is demonstrated. A short history of CFD and a brief introduction of STAR-CCM+ are given. The background of this research is introduced. The objectives of this research are described. The outline of this dissertation is listed at the end of this chapter.

1.2 Introduction of Bridge Safety and Scour

The safety of bridge is close related to human society activities. Therefore, reasons of bridge failure always attract researchers to study. Generally speaking, these reasons include overtopping, structural failure, debris accumulation, embankment erosion and scour (Annandale, 1993), which can be separated into two groups: functional and physical failures. For example, overtopping and debris accumulation lead to functional failures, which make bridges impassible. This kind of bridge failure is temporary and easily repaired at a relative low cost. Other factors like scour and embankment erosion, cause physical failures, which may seriously damage the structure of a bridge or have a serious negative influence on the capacity of stability of a bridge. This kind of bridge

failure is difficult to repair. Moreover, such repair is always requires expensive and time-consuming.

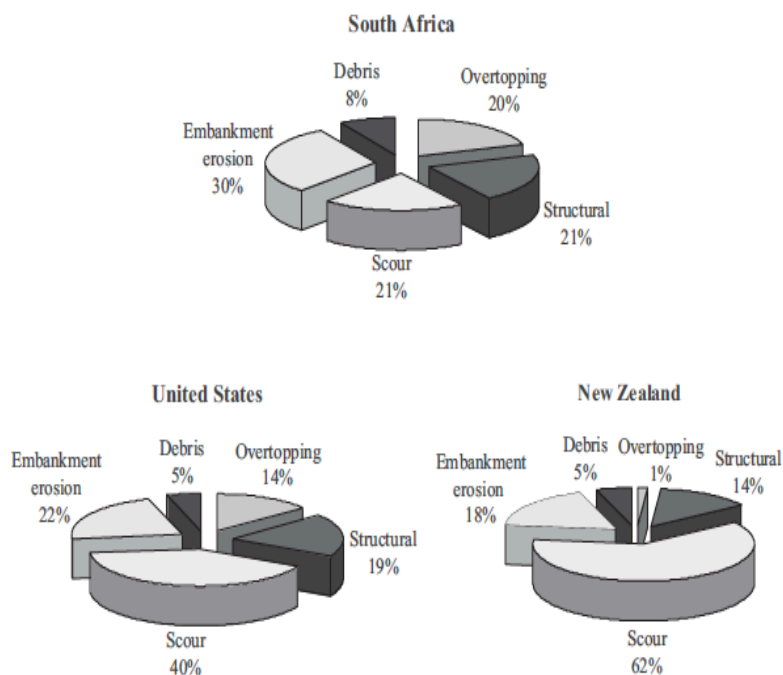


Figure 1.1 Relative contributions of factors of bridge failure (Annandale, 1993)

Figure 1.1 shows the relative contributions of different factors of bridge failure in South Africa, New Zealand and United States. Among the factors of bridge failure, scour is one of the most significant. In this research, the term “scour” is defined as follows. The earthen material in the immediate vicinity of hydraulic structures of a bridge, such as bridge piers, is removed when water flows around them, producing scour holes around them. If the amount of earthen material removed is large enough, a potential bridge failure may happen to threaten the safety of users. From 1989 to 2000, 15.51% of over 500 studied failures of bridge structures were associated to scour (Wardhana, 2003). The

data of the implementation of a nationwide bridge scour assessment program in the United States revealed that 141,405 river bridges in the United States are susceptible to scour with unknown foundations or are scour critical (Pagan-Ortiz, 2002). Scour is the biggest single reason of bridge failure in the United States. In this research, pier scour is mainly considered. An example of bridge failure caused by scour is the collapse of the Schoharie Creek Bridge (Figure 1.2). The center span and east center span of the 540-ft-long bridge over Schoharie Creek failed during a flood event in New York on April 5th, 1987. This accident killed nine people with one person missing. This tragedy is the main reason that leads to the implementation of a nationwide bridge scour assessment program.



Figure 1.2 Schoharie Creek Bridge, New York, failed by bridge pier scour in glacial till in 1987 (National Transportation Safety Board, 1988)

Because of the serious negative influence of scour on the stability and hydrodynamic performance of bridges, the study of scour around the hydraulic structure elements of a bridge is a primary focus of hydraulic studies. Such studies have two main applications. First, model bridge design is required to consider the vulnerability of the bridges to scour, no matter what kind of foundations it is on. Second, the replacement design of old bridges also requires a detailed assessment of its potential future scour, because an effective way to reduce the cost is to reduce the length of each pier.

Scour caused by water flow is a type of erosion. There are three kinds of basic necessary information to analyze scour: the quantification of the hydraulic loading on the riverbed, the quantification of the ability of the earthen material to resist this erosion capacity and the threshold relationship between them. Figure 1.3 shows the relation between hydraulic loading and scour. In Layer 1, the hydraulic loading is larger than the critical soil resistance. Therefore, earthen material is removed by the water flow and scour happens. In Layer 2 and Layer 3, hydraulic loading is still larger than the critical soil resistance, even though the hydraulic loading decays. Scour keeps going in these two layers. The hydraulic loading is not larger than the critical soil resistance in Layer 4, scour stops there and the maximum scour depth is approached.

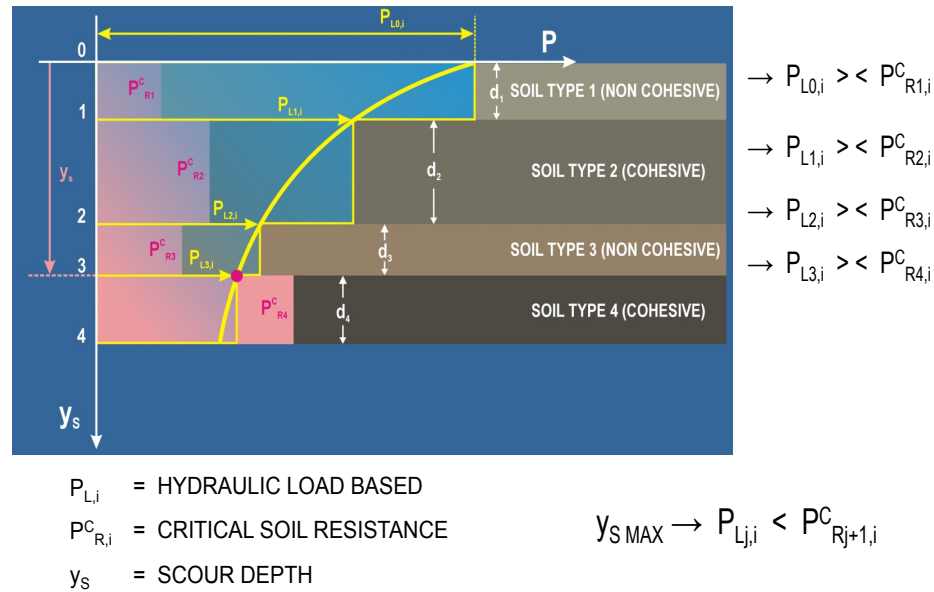


Figure 1.3 Hydraulic loading decay function (Suaznabar et al., 2014)

The quantification of the resistive capacity of the earthen material is complex and is dependent on many physical and chemical properties. In this research, the riverbed was formed with clean, non-cohesive and coarse-grained sand. The critical shear stress, τ_c , is a widely used physical quantity to indicate the capacity of the sand to resist erosion capacity. τ_c is the shear stress on the surface of the soil, at which particles of earthen material begin to move. There are several approaches to estimate its value, such as Guo's relation (2002). Practicing Engineers often use wall shear stress, average velocity and stream power as indicators to quantify the capacity of water erosion.

1.3 Development of A Computational Fluid Dynamics Method and Introduction of STAR-CCM+

The computational fluid dynamics (CFD) method is developed to numerically solve fluid dynamic problems by using numerical methods and algorithms. The fundamental basis of CFD is to solve the Navier-Stokes equations with defined boundary conditions and initial flow conditions. A typical procedure of a classical CFD code includes the following five steps. First, the physical boundaries are defined, which constitute the CFD geometry. Then the volume of the geometry occupied by the fluid is divided into a mesh of small cells. After meshing the geometry, appropriate physical models are activated to simulate fluid flow, like turbulence models, wall functions, equations of motion and special conservation and boundary conditions. Initial flow conditions are then applied to resolve the initial flow field. The time step and physical time (unsteady case) or number of iterations (steady case) is defined as the conditions to finish the CFD simulation. After successfully finishing the steps above, the CFD code begins to iteratively solve the given fluid dynamics problem. The postprocessor is used to visualize and analyze CFD simulation results.

CFD methods were first developed to solve the linearized potential equations. In the 1930s, two-dimensional (2-D) CFD methods were developed by using conformal transformations of the flow around a cylinder to the flow around an airfoil (Milne-Thomson, 1973). From 1957 to 1960, a series of CFD methods to simulate transient 2-D fluid flows were developed in the Los Alamos National Laboratory. In 1957, the Particle-In-Cell method (PIC) was developed by Harlow to treat transient, compressible flows of multiple materials with no restrictions on interfacial deformation (Harlow, 1957 and

Evans et al., 1957). In 1966, the Fluid-In-Cell method (FLIC) was developed to address particle fluctuations and large memory requirements (Gentry et al., 1966). In 1963, Fromms and Harlow developed vorticity and stream function methods to resolve problems of strongly incompressible contorting (Fromms and Harlow, 1963). In 1965, the Marker-And-Cell method (MAC) was developed to simulate incompressible, free surface flows (Harlow and Welch, 1965). The development of CFD methods is associated with growth of computer technology. The powerful computer capacity to deal with floating point numbers and huge storage space of contemporary computers make it possible to develop three-dimensional (3-D) CFD methods. The first 3-D CFD method is the panel method (Hess and Smith, 1967). Today, many kinds of CFD methods based on this method have already been fully developed and are commercially available. The ultimate target of a CFD method developer is to find out a better approach to accurately resolve Navier-Stokes equations. Now, there are a number of commercial CFD programs with 2-D and 3-D CFD codes, like Flow3D, FLUENT, ANSYS-Fluid and STAR-CCM+. These commercial CFD codes offer an economic way to calculate parameters of a fluid field and obtain details to analyze it.

STAR-CCM+ developed by CD-adapco Inc. is one of the most advanced commercial CFD codes. The “CCM” stands for “computational continuum mechanics”. It is based on the finite volume method (FVM) and applied to simulate fluid flows in and around objects. There are many special functions in STAR-CCM+, which make it friendly to users. One of the most significant advances is the client-server architecture, which reduces the need for expensive computers by allowing users to prepare a CFD model and do postprocessor on a normal computer while doing expensive math on a

remote super computer. Another outstanding function of STAR-CCM+ is the world's first commercially available polyhedral meshing algorithm, which has a stronger capacity to obtain accurate results for fluid-flow problems than other kinds of meshes with a similar number of cells, even though it increases the cost of time to mesh geometry (Brezzi et al., 2007). Another advanced function of STAR-CCM+ is the built-in surface repair tools, which can cut down the time of geometry preparation. For example, “surface wrapper” can automatically repair surfaces of CAD geometries by filling any holes, overlaps and cracks. Currently, STAR-CCM+ has already been widely used for a range of industrial and research applications including heat transfer, multiphase flows, reacting flows, discrete element modeling, aero-acoustics, optimization and fluid-structure interaction. In this research, STAR-CCM+ 8.04 and 9.06 was applied to simulate water flows around complex-shaped piers under different flow conditions to study the decay function of wall shear stress.

1.4 Research Background

An emergency study of the pier scour problem of the Feather River Bridge conducted by Kevin Flora inspired this research. This bridge was also used as an example to verify the results of this research and to develop the approach to apply the results.

The Feather River Bridge (Br. No. 18-0009) is on Route 20 in Sutter County, California. Pier 22 of this bridge in the main channel, as shown in Figure 1.4, has experienced scour and has been considered to be scour critical since 2001. This pier was also believed to be more vulnerable than other piers (like Piers 21 and 23) along the main channel banks, as shown in Figure 1.4. Moderately high releases from upstream Oroville

Reservoir in 2011 produced water flows that flowed out of the banks of the channel, especially the east bank. The peak discharge of this flow was estimated to be 44500 cfs and the maximum water surface elevation (WSE) was about 56.4ft. The bathymetry from about 1500ft upstream of the bridge to about 2700 feet downstream of the bridge was surveyed to reveal a substantial scour hole around Pier 22.

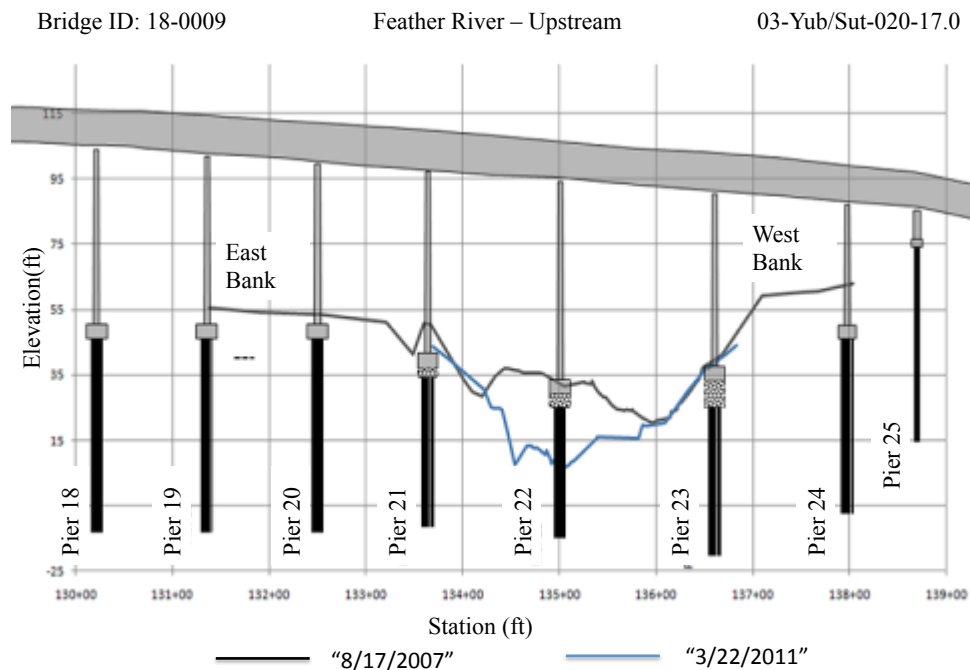


Figure 1.4 Cross-sections of Feather River surveyed in 2007 and March 2011

A 2-D hydraulic model for this pier has already been done for an emergency scour study conducted by Flora. The water flow was modeled by using March 2011 flow rate and the downstream WSE. Additionally, an estimated Q100 flow rate and downstream WSE were modeled with the 2007 topography. Table 1.1 shows these two kinds of flow

conditions. MF stands for “March Flow” and is assumed as the normal flow condition. Q100 is the flow condition of the flood event.

Table 1.1 Flow conditions

Event	Name	Flow Rate (ft^3/s)	Flow Depth (ft)
March 2001	MF	44,500	31.4
Q100	Q100	160,800	51

As shown in Figure 1.5, the left one is the original Pier 22. This pier includes four parts. From top to bottom, they are a small elliptic cylinder, a large elliptic cylinder, a rectangular foundation and 90 square H-piles. To restore the capacity of the stability to Pier 22, a pier retrofit scheme (the right one in Figure 1.5) was taken. This design was to surround the existing pile cap with 10 4-foot diameter CISS piles. They were tied into the existing pile cap with a new pile cap, which covers the previous one. The serious scour problem forced prompted the retrofitted design was taken and finished in December, 2011

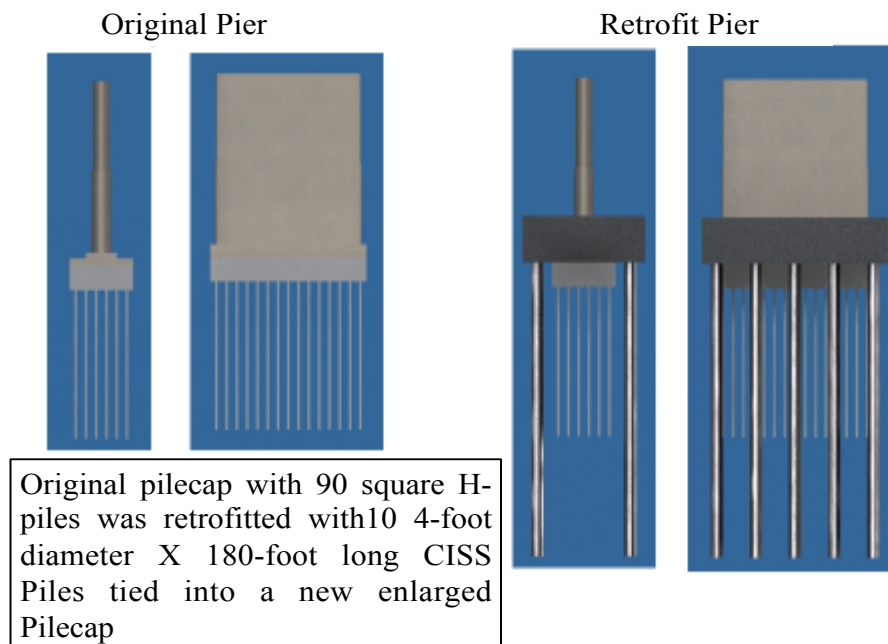


Figure 1.5 Geometries of the original Pier and the retrofitted pier

A series of physical experiments using 1:60 scaled pier models of the original Pier 22 and the new retrofitted design were conducted to surveyed scoured bathymetries around these piers under scaled flow conditions in the hydraulic laboratory of the Federal Highway Administration (FHWA), Mclean, Virginia. CFD methods were applied to simulate these physical experiments to develop a hybrid approach to study the relation between hydraulic loading and scour. The bathymetric data surveyed in 2007 (before the flood event) and in 2011 (after the event) was used to construct full-scale CFD models. A decay function was applied to study the pier scour problems of the Feather River Bridge.

1.5 Objectives of Research

The current physical experimental method confronts problems to directly measure any of the three indicators of water erosion capacity, especially wall shear stress on a dynamic bed. In other words, it is almost impossible to precisely survey wall shear stress in time or space due to the dynamic nature of the channel response to the scour and transport of the material. At the same time, since the mechanism and the theoretical solutions of scour are not yet fully developed, the CFD method has a weak capacity to simulate the real process of scour. Currently, a model to simulate scour process was conducted by using CFD methods to calculate wall shear stress and developing the dynamic bed with the empirical correlation of critical shear stress to iteratively deform the bathymetry under supercritical shear stress conditions (Tulimilli et al., 2011). But this approach does not yet represent the real scour process and the simulated flow is one-phase flow.

In this research, the physical experimental method and CFD method were combined to develop a hybrid method to study scour and to reveal the relation between wall shear stress and scour. The objectives of this research include the following major parts.

- (1) The whole scour process is separated into five parts in the physical experiments and the scoured bathymetries around piers are surveyed to create the original CAD models for CFD simulations.
- (2) CFD models are developed to simulate three-dimensional (3-D) two-phase (air and water) laboratory models and to calculate wall shear stress

distributions and values around complex-shape piers under different kinds of flow conditions;

- (3) A decay function or an envelope function of wall shear stress around complex-shape piers is developed by combining CFD wall shear stress data and previous physical experimental data (Annandale 2006);
- (4) CFD simulation results of water flows around a rectangle pier with 30° attack angle are used to verify the decay function;
- (5) CFD models are developed to simulate water flows in full-scale Feather River Bridge models to obtain wall shear stress distributions around Pier 22, verify the decay function and find out the applications of this function in the real world.

1.6 Dissertation Outline

The dissertation consists of seven chapters. The background of this research is described in Chapter 1, in which the significance of studying bridge scour and development of the CFD method are also introduced. Chapter 2 is the literature review about the related knowledge about pier scour, decay function of hydraulic loading and CFD modeling for open-channel flows. Chapter 3 briefly introduces the physical experiment section of the hybrid approach. Chapter 4 discusses the CFD section of the hybrid approach, which includes the development, validation and calibration of CFD models of all cases in the physical experiment section. The simulation results of wall shear stress are also represented in this chapter. The development, calibration and validation of the decay function of wall shear stress are discussed in chapter 5. CFD

modeling for the full-scale Feather River Bridge is discussed in detail in Chapter 6, which also preliminarily discusses the application of the developed decay function. The conclusions of this research and suggested future works are given in Chapter 7.

CHAPTER 2 Literature Review

2.1 Overview

In order to develop a decay function of wall shear stress with the hybrid approach of a physical experimental method and a CFD method, the literature review about the decay function of hydraulic loading, the physical experimental method and CFD method for open-channel flows is beneficial. In this chapter, current work about the decay function of hydraulic loading is summed up and the CFD method for open-channel flow is reviewed. This chapter also does a brief overview about the physical experimental method to study local pier scour.

2.2 Pier Scour

The process of scour around a bridge pier is time dependent. The maximum scour depth will be attained when the erosion capacity of the water flow and the resistance capacity of the earthen material to erosion are in equilibrium (Melville B W and Chiew, 1999). In the past several decades, research of pier scour mechanism was mainly about water flows around regular-shape piers by using physical experimental methods or data collected in the field. The physical experiment study of pier scour conducted by Chabert (1956) was considered to be the oldest and most complete research on this field (Oliveto and Hager, 2002). A series of physical experiments modeling water flows around a circular cylinder with a sandy bathymetry were conducted to study the scour mechanism (Melville, 1999). In order to have a better understanding of pier scour process, physical experiments were designed to study the local scour around a cylindrical pier with beds composed of uniform and layers of uniform sediments (Ettema, 1980). With these

outstanding studies, many equations were developed to estimate the maximum scour depth (Breusers et al., 1977; Richardson and Davis, 2001; Melville and Sutherland, 1988). Moreover, the significant influence of the foundation of a pier on the scour began to be noticed by some researchers, like Shen et al. (1966). The methods to estimate the scour depth for piers with foundations were developed (Jones et al., 1992 and Parola et al., 1996). The physical experimental method to study scour around a pier with a live-bed were developed as a powerful approach to study pier scour mechanism (Melville, 1984). However, current studies mainly rely on physical experimental methods and data collected in the field and their focuses are to understand the scour mechanism and estimate the maximum scour depth. Hence, there is a lack of study of the relation between hydraulic loading and scour.

2.3 Critical Shear Stress

The capacity of earthen material to resist water flow erosion is one of the three kinds of basic information to study scour. Since critical shear stress is used by many numerous erosion models as an important soil parameter governing detachment by runoff (Léonard et al., 2004), it was used as the indicator of the capacity of earthen material to resist water flow erosion.

There are two major types of earthen material, physical gels and chemical gels. Thus, the quantification of the resistive capacity of the earthen material has a complex relation with many physical and chemical properties itself. There are many studies to estimate or measure the critical shear stress. For example, Gilley et al. (1993) developed a method to identify critical shear stress and critical flow rate required to initiate rilling

on selected sites. Physical experiments were conducted to measure critical shear stress for entraining fine sediments in a boundary layer (Vanoni, 1964). A simple function to calculate critical shear stress for cohesive bottom sediments was developed with a series of physical experiments (Otsubo and Muraoka, 1988). An approach to calculate critical shear stress for sand and mud mixtures was developed by Ahmad et al. (2011).

In this research, the earthen material of the riverbed is clean, coarse-grained sand. This material is a typical kind of non-cohesive physical gel. There are several reasonable approaches to estimate the value of the critical shear stress. The first time in history to study the critical shear stress of this kind of earthen material is the work by Shields in 1936. After that, his work was developed by other researchers, such as Papanicolaou et al. (2002), Dancey et al. (2002) and Dey (2003). An approach to calculate the critical shear stress, τ_c , of non-cohesive sediment on a flat bed was given by Guo (2002), as shown in Eq.2.1 and Eq.2.2

$$\frac{\tau_c}{(\rho_s - \rho)gd_{50}} = \frac{0.23}{d_*} + 0.054[1 - \exp(-\frac{d_*^{0.85}}{23})] \quad (2.1)$$

$$d_* = \left[\frac{(\rho_s/\rho - 1)g}{v^2} \right]^{1/3} d_{50} \quad (2.2)$$

where d_{50} is mean diameter of sediment, ρ_s is density of sediment, ρ is density of water, g is gravity acceleration, d_* is the dimensionless diameter and v is kinetic viscosity of water. The critical shear stress of non-cohesive particles on a slope also has relation with the slope and flow direction.

2.4 Boundary Flow

The interaction between water flow and earthen materials occurs in the boundary region. And it determines whether particles move or remain in place. So the water flow in the boundary region plays a significant role, which heavily affects the magnitude of wall shear stress. For a smooth riverbed, the viscous sub-layer facilitates the interaction between water flow and the fixed boundary. For a rough bed, because of the phenomenon known as bursting (Einstein and Li, 1956; Kim et al., 1971; Offen and Kline, 1974 and Offen and Kline, 1975), the viscous sub-layer is less stable in a rough turbulence flow and the value of wall shear stress is obvious larger than the value calculated with Newton's law of viscosity, $\tau = \mu \frac{du}{dy}$. Moreover, the water flow around piers is often complex, which increases turbulence intensity and the erosion capacity of the water. And this results in the scour around the pier, which may causes bridge failures.

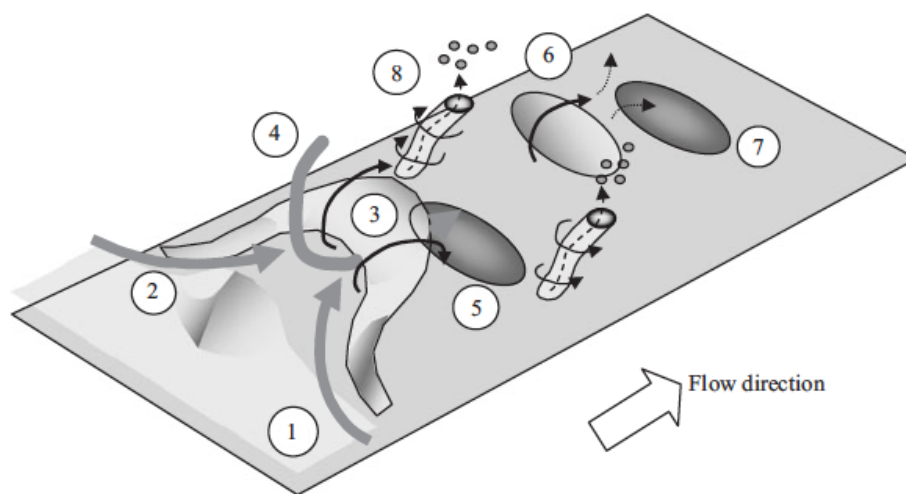


Figure 2.1 Flow at the boundary

Figure 2.1 shows the water flow process in the boundary region for a turbulence flow (Annandale, 2006). It separates the boundary flow in a turbulence flow into eight parts: (1) one assumes there is a stable viscous sub-layer at first; (2) a perturbation is imported into the laminar sub-lawyer because of the rough bed and the viscous sub-layer becomes instable; (3) the hairpin vortices are developed and their most downstream ends lifted upwards;(4) the high-velocity sweeps of water flow into the space below the hairpin vortices; (5) this water flow interacts with the bed and leads to a high-pressure zone; (6) at the same time, the developed hairpin vortex moves downstream and the central part breaks loose and creates an eddy, whose flow direction cannot be predicted; (7) the eddies which flow toward the bed collide with it and lead to a low-pressure zone (Hofland et al., 2005);(8) the two remaining legs of the hairpin vortex temporarily attach to the low-pressure zone of the bed created by the vortex itself. The small vertices are low-velocity streaks. The negative pressure within these vortices can suck sediment upward and make it easy for the sediment to be removed by the water flow.

2.5 Decay Function of Hydraulic Loading

A study conducted by FHWA expressed the decay trend of the erosion capacity of the water flow with the increase of scour depth (Smith and Annandale, 1997). The results of the FHWA research (Annandale and Smith, 2001) identifies that the magnitude of the erosion capacity of water can be estimated as a function of scour depth.

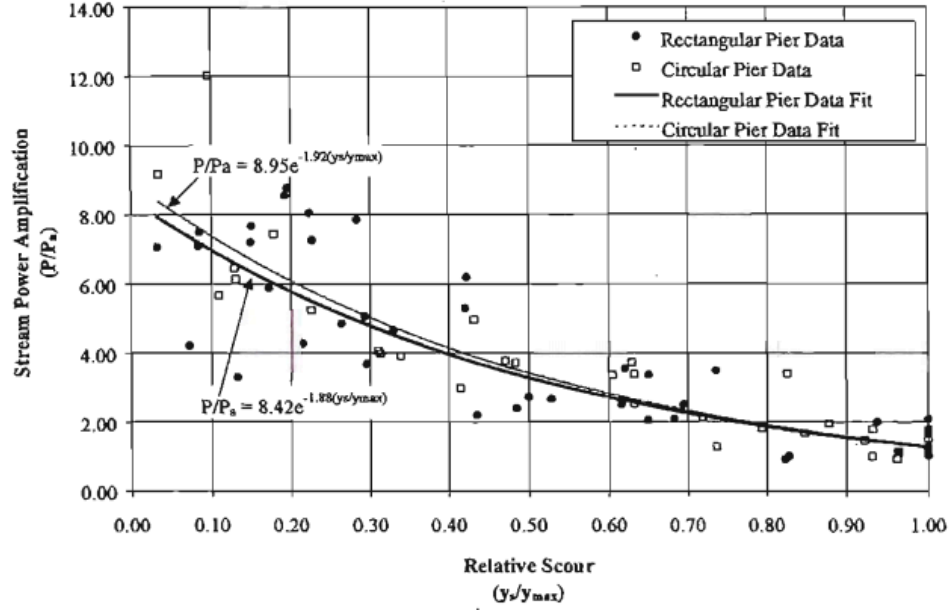


Figure 2.2 2-D stream powers at the base of a scour hole versus dimensionless scour depth from FHWA

As shown in Figure 2.2, P is the local stream power on the bed, which is equal to $\bar{U}\tau_w$. \bar{U} is the average velocity in the channel and τ_w is the wall shear stress. y_s is variable scour depth. P_a is the approach stream power, which can be estimated with Eq.2.3 and Eq.2.4.

$$P_a = 7.853\rho\left(\frac{\tau_a}{\rho}\right)^{1.5} \quad (2.3)$$

$$\tau_a = \rho g R_h s \quad (2.4)$$

where R_h is the hydraulic radius(in a wide channel, R_h is the flow depth) and s is the energy slope. The maximum possible scour depth, y_{max} , around a pier under the given

initial flow condition can be estimated with the bridge scour depth equation, Eq.2.5 (Arneson et al., 2012).

$$\frac{y_{max}}{y} = 2K_1K_2K_3\left(\frac{a}{y}\right)^{0.65}Fr^{0.43} \quad (2.5)$$

where y_{max} is the maximum scour depth, y is the approach flow depth, a is the width of the bridge and Fr is the Froude number. K_1 is a correction factor associated with the pier nose shape. K_2 is a correction factor associated with water flow with the flow attack angle (θ). K_3 is a correction factor associated with the bed condition. This means the maximum scour depth for a live bed with given clean-water flow conditions is a constant. Moreover, the average flow velocity, \bar{U} , is a constant for a uniform flow, while the energy slope s , density of water ρ and the hydraulic radius R_h (or water depth y) are also constant. Therefore, the decay function of stream power with relative scour depth can also be treat as the decay function of wall shear stress with relative scour depth. Since the indicator of non-cohesive particles to resist the erosion capacity is critical shear stress, the wall shear stress is a better indicator of the water erosion capacity, which can be directly obtained by using CFD method. Another important conclusion based on Figure 2.2 is that when the value of the local stream power decays to the approach stream power, scour stops and maximum scour depth is attained.

2.6 CFD Modeling for Open Channel Flow

The open-channel flows, which are turbulent, have two prominent characteristics: they are always turbulent and the motion of the free surface is one of the most complex

natural processes. In order to develop an accurate CFD model for open-channel flow, it should include appropriate mathematical models to simulate the free surface and the turbulent flow. The Volume of Fluid method (VOF) is a free surface technique of the CFD method, which can model two or more immiscible fluids by solving a single set of momentum equations and tracking the volume fraction of each kind of these fluids (ANSYS-Fluent user guide). Noh and Woodward (1976) first gave out the initial VOF method based on the earlier Mark-And-Cell (MAC) and it was developed further by Chen et al. (1997). Currently, the most widely used VOF method was developed by introducing a Piecewise-Linear Interface Calculation (PLIC). The VOF method developed by Hirt and Nichols (1981) is utilized in STAR-CCM+ to capture the motion of the free surface. The details of the VOF in STAR-CCM+ were discussed by Samir and Milovan (2013) in Star Japanese Conference. Figure 2.3 is an example of the application of VOF method, which simulates the process of a droplet falling on a water free surface. The black area is water and the white area is air (http://en.wikipedia.org/wiki/Volume_of_fluid_method).

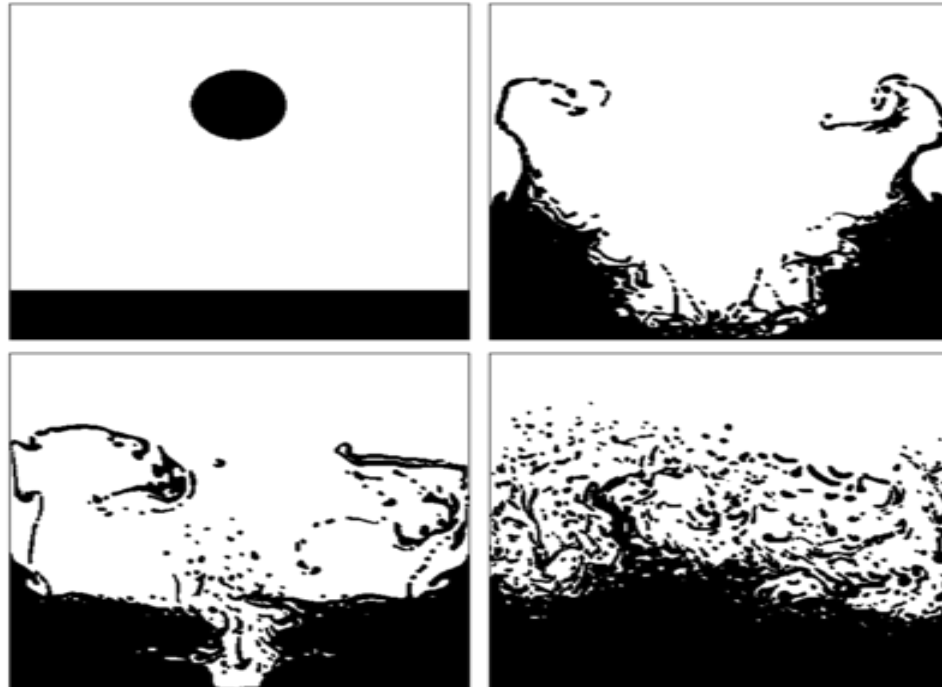


Figure 2.2 An illustration of CFD simulation by using VOF

Even though the physical experimental research about turbulence in air flows began in the 1950s by using hot-wire anemometry, the difficulties in applying anemometry to typical water flows led to the start of basic research on open channel turbulence in the 1970s (Nezu, 2005). The current experimental techniques to study open channel flow are expensive, tedious and sometimes unfeasible. Even though there have been many new methods in this area, CFD is still an inexpensive alternative, that reduces the time and cost to study open-channel. There are two main sources of difficulties of numerical open channel flow: (1) the proper recognition of the complex physical flow processes; (2) and the mathematic descriptions of this process and the solution of the derived equations (Szymkiewicz, 2010).

One of the core parts of a CFD modeling for open-channel flow is to resolve or simulate turbulence. Turbulence is often considered to be formed with a wide range of eddies with different length scales (Pope, 1962). The energy of turbulence translates from large-scale eddies to smaller ones, which is well known as the Richardson energy cascade. According to Kolmogorov's hypothesis (1941), most of the energy is stored in the large eddies, which is transferred to smaller eddies by the nonlinear mechanism of vortex stretching. Finally, the energy is dissipated by viscous forces in the smallest eddies, whose length can be estimated with Eq. 2.6 (Landahl and Mollo-Christensen, 1992)

$$\eta = \left(\frac{v^3}{\epsilon}\right)^{1/4} \quad (2.6)$$

where ϵ is the average rate of dissipation, and ν is the kinetic viscosity of the fluid.

The direct numerical simulation (DNS) is a kind of CFD method, in which the Navier-Stokes equations are numerically solved by resolving all of the spatial scales of the turbulence, from the Kolmogorov scale to the integral scale (Orszag, 1970). This also requires the size of mesh cell to be very small so that the number of mesh cells is very large. Therefore, DNS models have very high requirements for storage space and computational time cost, even though the Reynolds number of the simulated fluid flow is very small. To reduce the storage requirement and computational time cost, the large eddy simulation method (LES) was developed. In 1963, this mathematical model for turbulence was initially used to simulate atmospheric air currents (Smagorinsky, 1963). LES imports a filter size Δ to separate eddies in two groups: large eddies and smaller eddies. LES directly resolves large eddy, whose scales are between the domain size L and

Δ . LES models smaller eddies, whose scales are smaller than Δ . Figure 2.4 shows the differences between DNS and LES (Rodi et al., 2013), $E(k)$ is the energy spectrum and k is the wavenumber. The main obvious difference between LES and DNS is caused by the different approaches to handle smaller eddies, which are considered to be homogeneous in LES. The advantage of LES is that it has the capacity to capture complex flows with a relative small computational time cost and storage space than DNS.

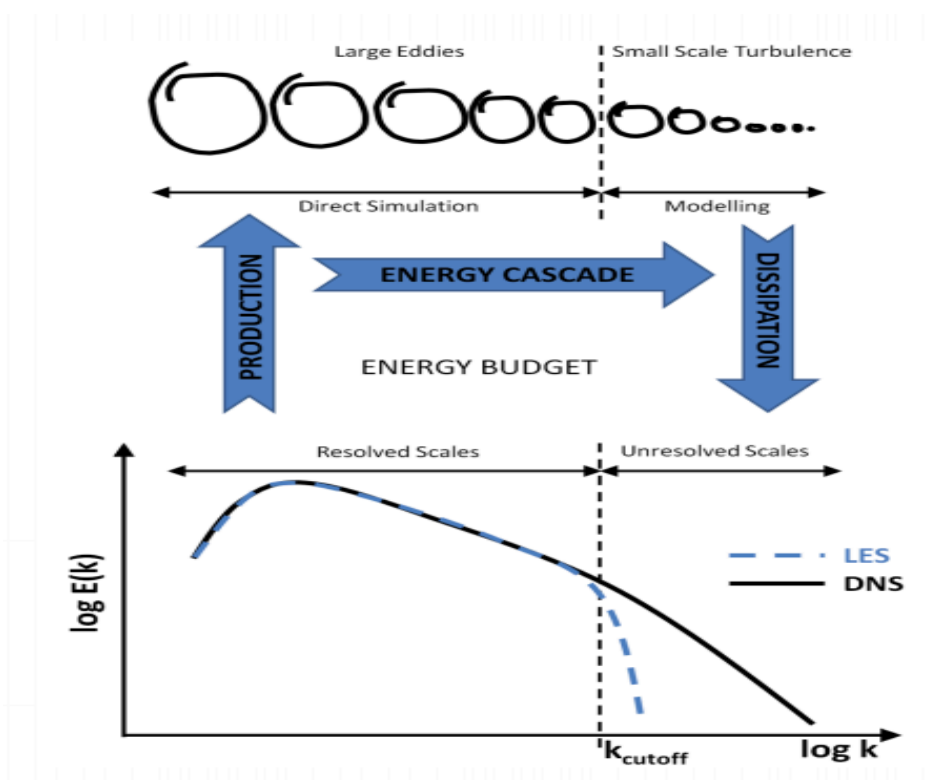


Figure 2.3 Differences between DNS and LES

Many engineering studies require, however, little knowledge of the instantaneous turbulent flow features. These features means of semi-empirical formulations, rather requiring a detailed characterization of the time averaged spatial flow structure equations,

such as Reynolds-averaged Navier-Stokes (RANS) equations (Ferreira et al., 2011) can be used to do this. The RANS equations are time-average equation of motion for fluid flows. Reynolds decomposition is the foundation of this numerical method, which separates the time-average and fluctuating parts of a physical quantity (Müller, 2006). RANS equations are often used to describe turbulence flows by offering approximate time-average solutions to Navier-Stokes equations. The unsteady RANS (uRANS) model is a kind of CFD method, which is an alternative approach to LES for industrial flows (Davidson, 2006). The uRANS equations are the usual RANS equations, but with the transient (unsteady) term retained. Despite the time dependence, and large vertical structures, uRANS is not a simulation of the turbulence, only of its statistics (Iaccarino, 2003). In the RANS model, the resulting equations for the mean quantities are essentially identical to the original equations, except that an additional term now appears in the momentum transport equation. This additional term is a tensor quantity, which is known as the Reynolds stress tensor (Eq.2.7).

$$\mathbf{T}_t \equiv -\rho \overline{v'v'} = -\rho \begin{bmatrix} \overline{u'u'} & \overline{u'v'} & \overline{u'w'} \\ \overline{u'v'} & \overline{v'v'} & \overline{v'w'} \\ \overline{u'w'} & \overline{v'w'} & \overline{w'w'} \end{bmatrix} \quad (2.7)$$

The detached eddy simulation method (DES) is a hybrid model to simulate turbulence by combining RANS and LES, which was first developed by Spalart et al. (1997). In near-wall regions and where the turbulence length is less than the grid dimension (size of mesh cell), RANS is used to simulate the turbulence there. And in the

regions with fine enough mesh, LES is activated to resolve the flow field. The advantage of this method is that some eddies are still resolved even with a coarse mesh. In Figure 2.5, the mesh of the left frame is coarse and the right frame is much finer. Therefore, more details of the airflow are captured on the right side. Some eddies close to the wing are still captured on the left side and the simulation results of both side are general symmetry.

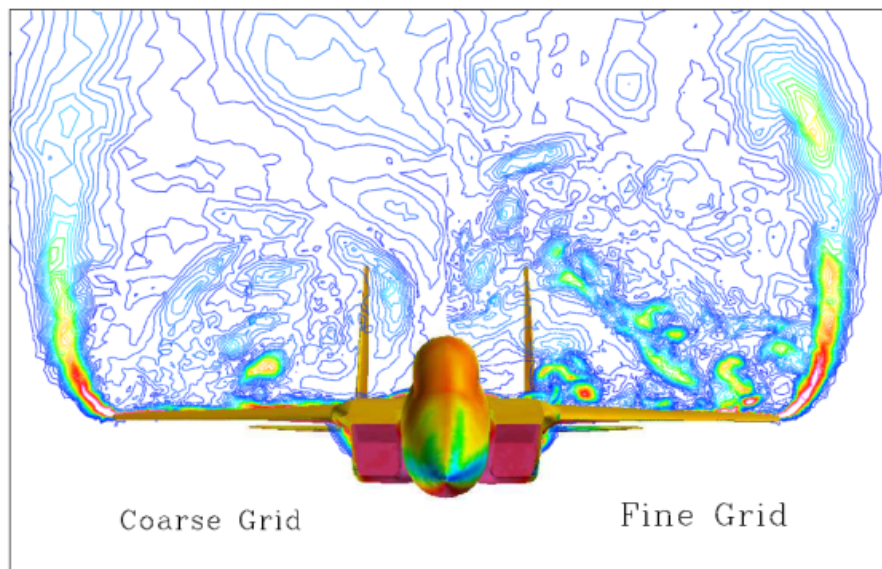


Figure 2.4 Contour of the instantaneous vorticity magnitude (Squires, 2004)

Among DNS, LES, DES, and RANS/uRANS, the high requirements for computer capacity of DNS, LES and DES make them unsuitable to simulate industrial flows. The previous studies prove that the results of 3-D CFD models with uRANS models and appropriate free surface models to simulate open channel flow general agree with the measured data (Wu et al., 2000). In STAR-CCM+, the combination of a uRANS model

and the VOF model is widely utilized to simulate open-channel flows, like Xie (2011) and Zhai (2012).

CHAPTER 3 Description of Physical Experiments

3.1 Overview

The main task of the physical experiments in this research is to obtain scoured bathymetries around different piers under different flow conditions. In this chapter, the experimental arrangements and devices are described. The method to scaled the flow conditions of March Flow (MF) and Q100 is introduced. The scoured bathymetries were surveyed with a laser point distance sensor. These surveyed data of bathymetries and models of piers are combined to create the original CAD models in SOLIDWORKS for CFD simulations. All physical experiments were conducted by Mr. Oscar Suaznabar in TFHRC Hydraulics Research Laboratory.

3.2 Physical Models

A series of physical experiments were designed to represent the scour process around the scaled original pier of Feather River Bridge under flow conditions of the normal state (MF) and the flood event (Q100). The experiments with the scaled retrofitted pier were conducted to simulate the future scour process around it. Each of the whole scour process was separated into five parts to obtain bathymetries with different scour depths. The shape of the bathymetry with the maximum equilibrium scour hole around the scaled original pier under the scaled normal flow condition (MF) of the physical experiment should be similar to the one observed in the field, which is also the standard to verify and calibrate the design of the physical experiment.

3.2.1 Physical Experiment Devices

These physical experiments were conducted in the tilting flume in the FHWA J. Sterling Jones Hydraulics Research Laboratory. As shown in Figure 3.1, the title flume is 1.82-m-wide by 21.3-m-long (6-ft-wide by 70-ft-long) with a sediment recess in the middle for local scour modeling. It has a total pumping capacity of 22,712L/min with variable-frequency drives capable of simulating in-flow hydrographs. The automated flume carriage is an automated three-axis positioning system, which is instrumented to position probes at any location with suitable sensors to measure physical quantities of interest.



Figure 3.1 Tilting flume in FHWA hydraulic laboratory

(<http://www.fhwa.dot.gov/publications/research/infrastructure/hydraulics/12022/004.cfm>).

In this research, a point laser distance sensor was instrumented on the automated flume carriage to survey the distance between the bed and the sensor, as shown in Figure 3.2. These data are automatically converted into the elevation of each point on the bed. The original bed elevation was set prior to the test run and maintained the same for all cases of the same pier model under the same flow condition. Therefore, the difference between the surveyed elevation and the original one is the final bathymetric change, which was converted into the bathymetry CAD model in SOLIDWORKS. In order to eliminate the negative influence of water on the laser distance sensor, these elevation data was surveyed after the water was drained.



Figure 3.2 Point laser distance sensor

The piers in these experiments are 1:60 scaled pier models of the original Feather River Bridge pier and the retrofitted one, which were created with a 3-D printing technique. To simplify this research, the bed was formed with coarse non-cohesive clean sand ($d_{50}=1\text{mm}$). And the original shape of the bed of all cases was flat.

3.2.2 Scaled Flow Conditions

In these physical experiments, Froude similarity was applied to calculate the flow conditions. The Froude number (Fr) was maintained the same for these two kinds of flow conditions, $Fr_M = Fr_P$, where suffix M is for model and suffix P means prototype. The flow rate (average velocity) and the flow depth are two main flow conditions in this research. The physical experimental flow conditions were calculated as Eq.3.1 and Eq.3.2 (a)(b).

$$\text{Flow Depth: } D_M = \lambda D_P \quad (3.1)$$

$$\text{Flow rate: } Q_M = Q_P \lambda^{5/2} \quad (3.2a)$$

$$\text{Average Velocity: } V_M = V_P \lambda^{1/2} \quad (3.2b)$$

where λ is the length scale factor. Since the geometry scale factor of the piers was 1:60, λ was set as $\lambda = \frac{L_M}{L_P} = \frac{1}{60}$. D_P is the prototypic flow depth, whose reference is the top of the pile cape of the original pier. It is necessary to point out that the flow depth here is not the depth from the water surface to the deepest point of the bathymetry. From Table 1.1,

the depth of March 2011 is 31.4 *ft* (9.6*m*), so the depth of March 2011 in the experiment is $\frac{9.6m}{60} = 0.16m$. The depth of Q100 is 51 *ft* (15.5*m*), so the depth of March 2011 in the experiment is $\frac{15.5m}{60} = 0.26m$. The inlet average velocities of MF and Q100 in these experiments are different from the calculated ones. The reasons are that the earthen material of the physical experiments is different from the Feather River and the width of the tilting flume is fixed as 1.82m. Thus the average inlet velocities of these two kinds of flow conditions need some necessary adjustments to ensure these physical experiments work well. The final data of the flow depth and average flow velocity of scaled flow conditions are shown in Table 3.1.

Table 3.1 Flow conditions

Flow Condition Name	Depth (m)	Average Velocity (m/s)
MF	0.16	0.34
Q100	0.26	0.41

3.2.3 Additional Information

The scour process around a given pier under certain flow conditions was separated into five parts by observing: flat bed, 25% scour, 50% scour, 75% scour and maximum equilibrium scour. Since the bathymetries of cases with a flat bed are known, there are 16 cases need to do physical experiments to surveyed the scoured bathymetries (2 flow conditions X 2 kinds of piers X 4 kinds of bathymetries). In this research, there are four groups and totally 20 cases, as shown in Table 3.2. The relative scour depth of

each case was defined as $Y_* = \frac{Y_s}{Y_{max}}$, where Y_s is the scour depth of each case and Y_{max} is the maximum scour depth under a certain flow condition around a given pier.

Table 3.2 Physical experiment cases

Group	Case Name	Pier	Flow Condition	Relative scour depth
MF_O	MF_O_0	The original pier	MF	0%
	MF_O_25			29.04%
	MF_O_50			45.19%
	MF_O_75			60.49%
	MF_O_100			100%
MF_R	MF_R_0	The retrofitted pier	MF	0%
	MF_R_25			44%
	MF_R_50			57.58%
	MF_R_75			76.38%
	MF_R_100			100%
Q100_O	Q100_O_0	The original pier	Q100	0%
	Q100_O_25			32.97%
	Q100_O_50			50.14%
	Q100_O_75			60.08%
	Q100_O_100			100%
Q100_R	Q100_R_0	The retrofitted pier	Q100	0%
	Q100_R_25			42%
	Q100_R_50			65.24%
	Q100_R_75			74.49%
	Q100_R_100			100%

3.3 Physical Experimental Results

Figure 3.3 is a comparison of the shape of the scour hole between the Feather River and the physical experiment. The two upper graphs are Feather River bathymetry surveyed by sonar and the bottom two graphs are the experimental ones. The shape of the scour hole of the maximum equilibrium scour, which was obtained in the flume, is close to the one observed in the Feather River. In both of them, the depth of the scour hole is larger in the area around the leading edge of the pier and relative small in the area around the tailing edge. This is the evidence that the physical experiment design does a good job of representing the scour process around the original pier of the prototype Feather River Bridge. Thus, to a certain degree the scour, process around the retrofitted pier in the experiments is reliable to study the future scour around it.

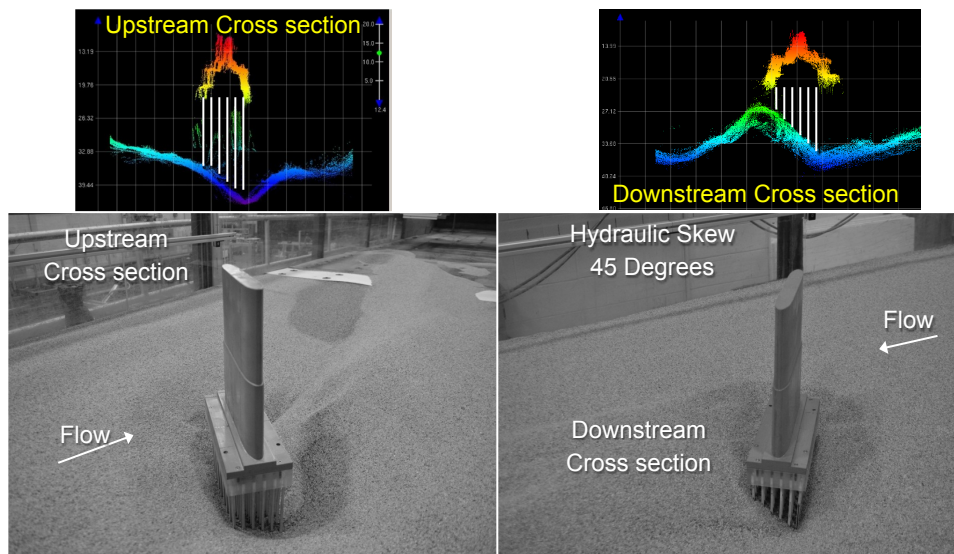


Figure 3.3 Comparison between Feather River and experimental scour hole shapes

SOLIDWORKS was applied to create original CAD models by importing the surveyed bathymetry elevation data and pier models. Figure 3.4 shows the original CAD models of Group MF_O. The other surveyed scoured bathymetries around piers are in Appendix A. The original CAD model is not a closed volume, but the CFD method requires that the geometry of the model has closure. Therefore, five extra surfaces (four walls around the surveyed bathymetry and the top) were added to each original CAD model to create a closed volume.

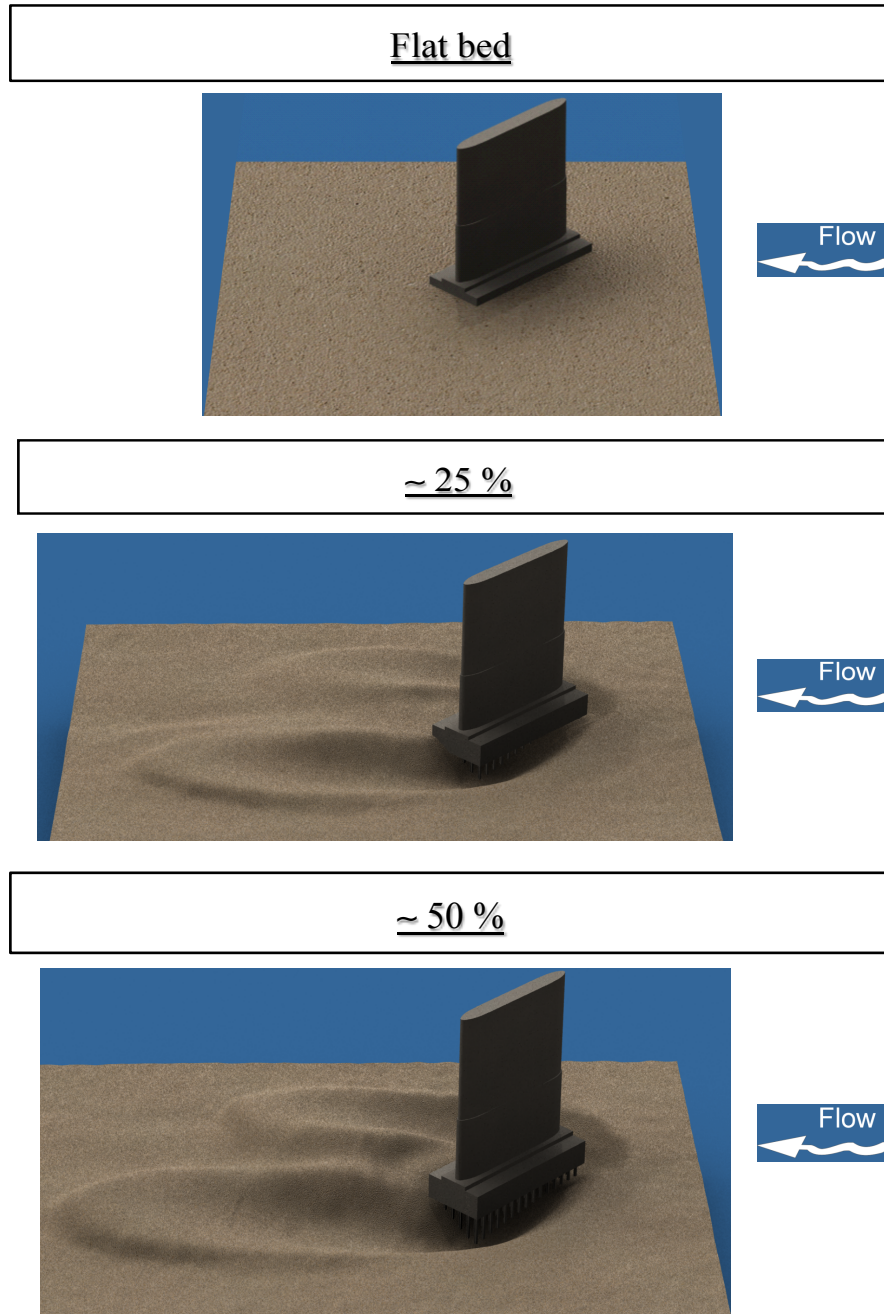


Figure 3.4 Original CAD models of MF_O

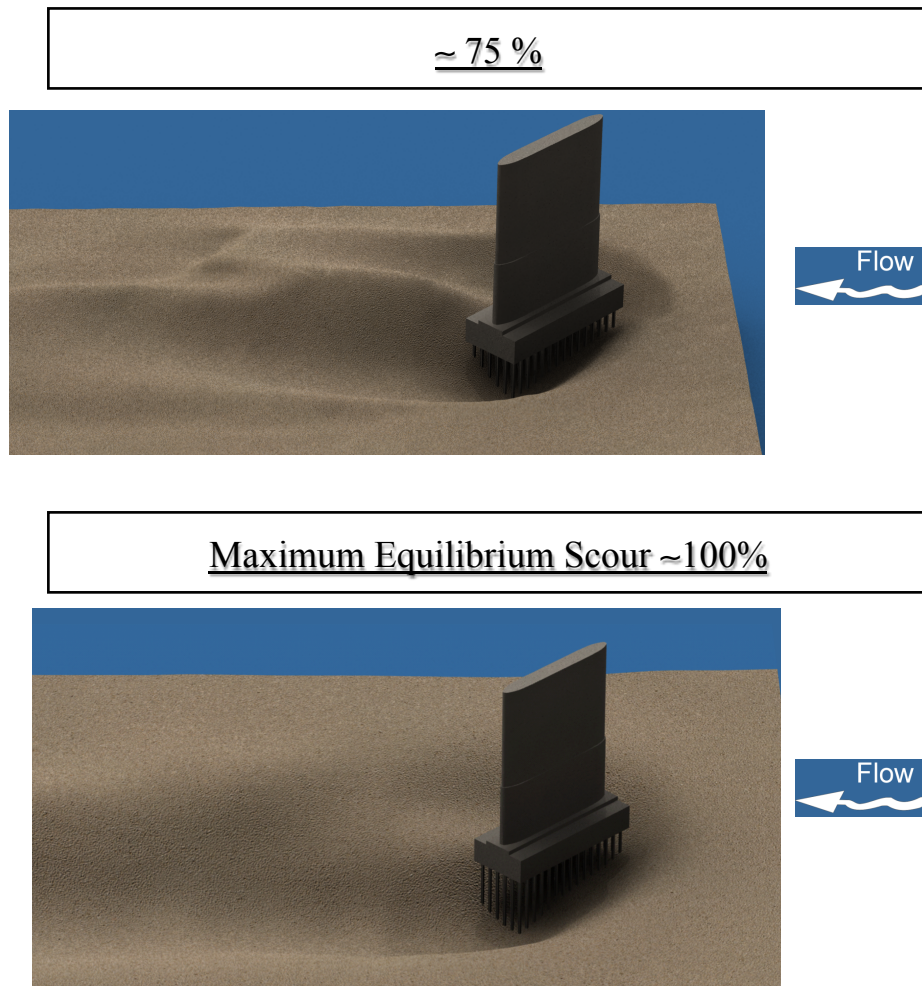


Figure 3.4 (continue) Original CAD models of MF_O

3.4 Summary

The physical experiments conducted by Mr. Oscar Suaznabar accurately represent the scour process around Pier 22 of the Feather River Bridge and represent a credible scour process around the retrofitted design. The scoured bathymetry of each case was surveyed and used to create an original CAD model for CFD simulations. In Chapter 4, the approach of using these original CAD models to develop CFD models is detailed. The validation and calibration of these CFD models are also discussed in the next chapter.

CHAPTER 4 Development of the CFD models

4.1 Overview

The greatest advantage of the CFD method is that it provides information of indicators of water erosion capacity. With the original CAD models, which are based on the data of the surveyed bathymetries, a series of three-dimensional (3-D) CFD models was developed to simulate water flows of cases in the physical experiment and directly quantify the water erosion capacity in STAR-CCM+, especially wall shear stress distributions. Figure 4.1 is a general procedure of the development of a CFD model in STAR-CCM+. In this chapter, these steps are discussed in detail. Moreover, the validation and calibration of CFD models are also included in this chapter. Before discussing the development of CFD models, there are two nouns must be defined. “Physical time” is the time that the CFD model simulates. “Computational time” is the time that the CFD model takes to finish the simulation.

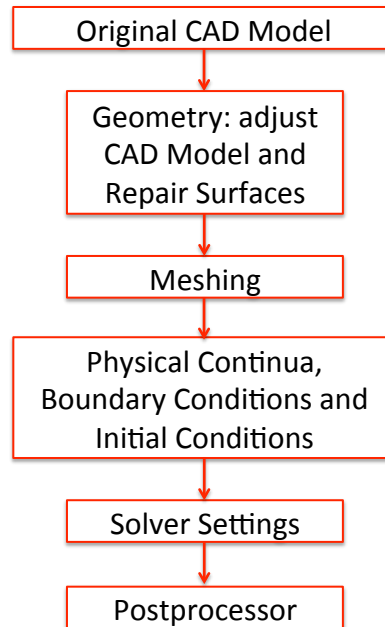


Figure 4.1 Procedure of development of CFD model in STAR-CCM+

4.2 CFD Geometry

The geometry of STAR-CCM+ defines the flow domain of a CFD model. It must be a closure volume and as close to the simulated object as possible. In the physical experiments of this research, since the range of measurement of the automated three-axis positioning system does not cover the whole area of the sediment recess, researchers mainly surveyed the bathymetry around the pier. Therefore, the width and the length of the original CAD models are different from the size of the tilting flume. Additionally, extra inlet and outlet channels are necessary to eliminate the potential influence of the boundary conditions on the inlet and outlet surfaces. Also, the height of the final CFD geometry should be large enough to allow air and water to flow through the domain. Only after these necessary adjustments on the original CAD model, does it satisfy the requirements of STAR-CCM+ and is close to the physical experiments. These necessary

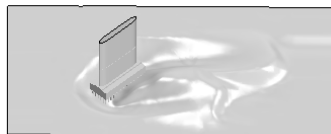
adjustments on the original CAD model inevitably cause some small perturbations, which cause the bathymetry of the final CFD geometry to be different from that of the physical experiment. Hence, additional CFD simulations were designed to analyze and eliminate the influence of these perturbations.

4.2.1 Approaches to Modify Original CAD Models

In STAR-CCM+, there are two approaches to adjust the imported original CAD model to the target one. One approach is the built-in CAD function, which allows users to directly modify the CAD model. The other approach is “extruder”, which is a kind of mesh model and does not change the original CAD model.

With the built-in CAD function, the face sketch of a selected surface can be created and extruded to a body. The size of the extruded body is thoroughly under the control of users to approach the target size. The advantage of this approach is that all the necessary adjustments work on the original CAD model. Therefore, the adjusted CAD model can be exported for other studies in other software. While, based on the capacity of the computer and the complexity of the shape of the surface sketch, this approach takes a relatively long time and requires a large amount of storage. At the same time, the final CFD geometry also increases the workload to mesh it. As shown in Figure 4.2, the upper model is the bathymetry of an original CAD model and the lower one is the bathymetry of the final CFD geometry of this CAD model. It is obvious that the width of this initial CAD model was enlarged to match the size of the tilting flume.

Original CAD model



Adjusted CAD model

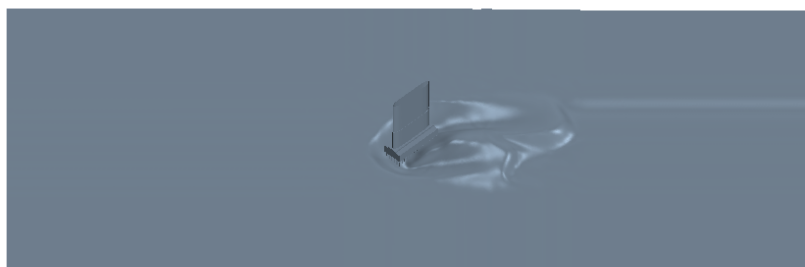


Figure 4.2 Bathymetries of an original CAD model and its final CFD geometry

The “extruder” is a newly developed approach to adjust the imported original CAD model. The introduction of extruder in STAR-CCM+ User Guide is quoted as following. “When one activates and enables the extruder meshing model for the selected specific boundaries, it performs an additional volume meshing step to enlarge the model when the core mesh and, optionally, prism layer mesh has been generated.” This approach requires users to set the supplied values for the number of layers, extrusion magnitude and stretching, and determine the direction of extending, either in the normal or a specified direction. Then, based on the given information, the volume mesh is extruded and extends the original domain to the target one. The main advantage of this approach is that it allows users to control the number of cells of mesh in the extended zones. Moreover, this approach requires the imported CAD model to be meshed first and

then extruded. Therefore, it does not require extra time to modify the imported CAD model. However, this approach does not work on the CAD model, so the final CFD geometry cannot be used by other software. As shown in Figure 4.3, the upper one is an original CAD model and the lower one is its extruded mesh result. The mesh result enlarges the imported original CAD model to the target size. Compared with the CFD geometry in Figure 4.2, this approach actually expands the mesh of the original CAD model instead of the CAD model itself.

Original CAD model



Adjusted CAD model

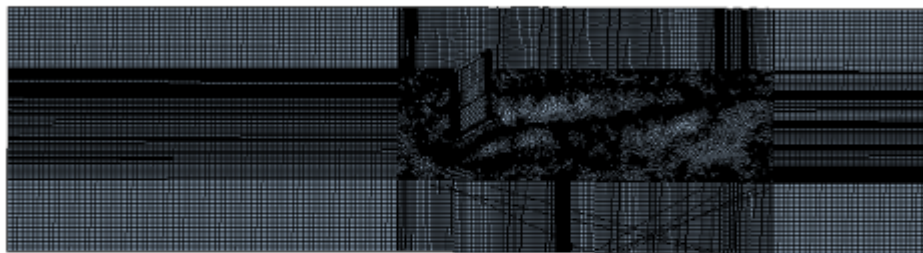


Figure 4.3 Bathymetries of an initial CAD model and its extruder mesh result

Since the flow domain of CFD simulation essentially determined by the mesh, these two kinds of approaches are equivalent. Both of them were applied in this research to optimize each case. Figure 4.4 is an example of the final CFD geometry with the name of each surface (top surface is hidden). It also clearly shows the extra perturbations on the

bathymetry, which were imported by modifying the original CAD model. The earthen material in the physical experiments is sand ($D_{50} = 1mm$). So the roughness height of the bathymetry of CFD geometry was empirically set as 2 mm. The boundary type of each face specified in the CFD model is shown in Table 4.1.

Table 4.1 Boundary conditions

Boundary Name	Type	Note
inlet	Velocity Inlet	-
outlet	Pressure Outlet	-
Top	Symmetry Plane	-
sides	Wall	Non-slip; Smooth
pier	Wall	Non-slip; Smooth
bed	Wall	Non-slip; Rough; Roughness Height = 2mm;

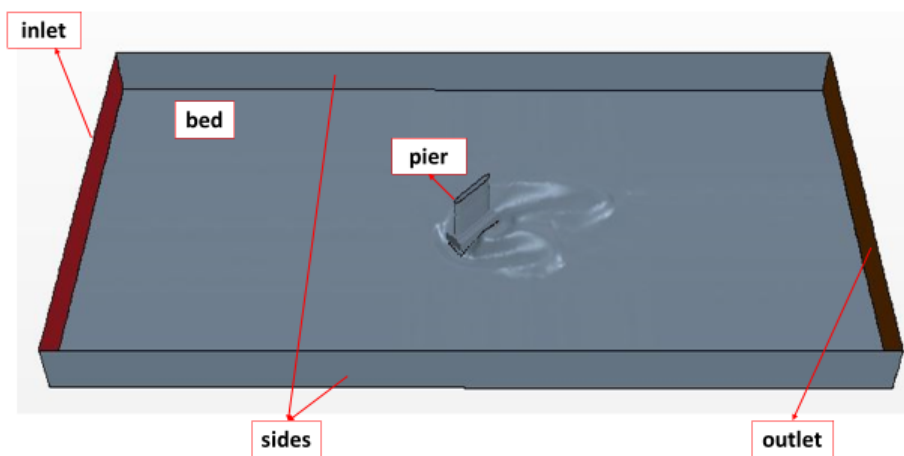


Figure 4.4 Final CFD geometry of Case Q100_O_50

4.2.2 Influence of Perturbations

The main source of these little perturbations is those necessary adjustments on the original CAD models, because the shape of the bathymetry of the extruded area is determined by the shape of the boundary of the bathymetry of the original CAD model. Since the shape of the bathymetry of the upstream may cause the water flow to be different from that in the physical experiment, it is possible that these perturbations have a serious negative influence, which may causes these CFD models to have a weak capacity to simulate the physical experiments. Thus additional CFD simulations were designed to analyze and eliminate the influence of these perturbations.

To simplify the study about these perturbations, a comparison between CFD models with a flat bathymetry with and without these perturbations was conducted. As shown in Figure 4.5, bathymetry of the right panel has some perturbations and that of the left is a completely flat bed. Since these perturbations are not obvious in the geometric diagram, a mesh diagram is an alternative. For the complete flat bed, the size and shape of the mesh cell in the non-near-wall region (the region in the red rectangle) are uniform, while this uniformity does not exist in the mesh of the case with perturbations.

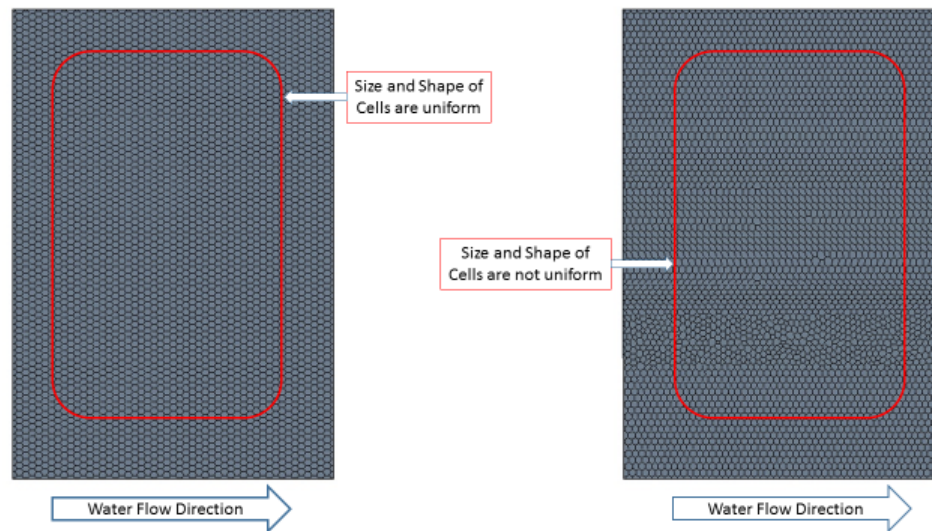


Figure 4.5 Meshes of the flat bed with and without perturbations

The roughness height of these two cases is 2 mm. The turbulence model used for these two CFD models is the unsteady RANS K-Epsilon model, and the physical time was set to 20s. The VOF model was selected to simulate the free surface. As shown in Figure 4.6, the velocity distribution of this plane and the values of the points on this plane are used to analyze the influence of these perturbations. This figure also represents the states of the free surfaces of these two cases. There is not an obvious difference between them.

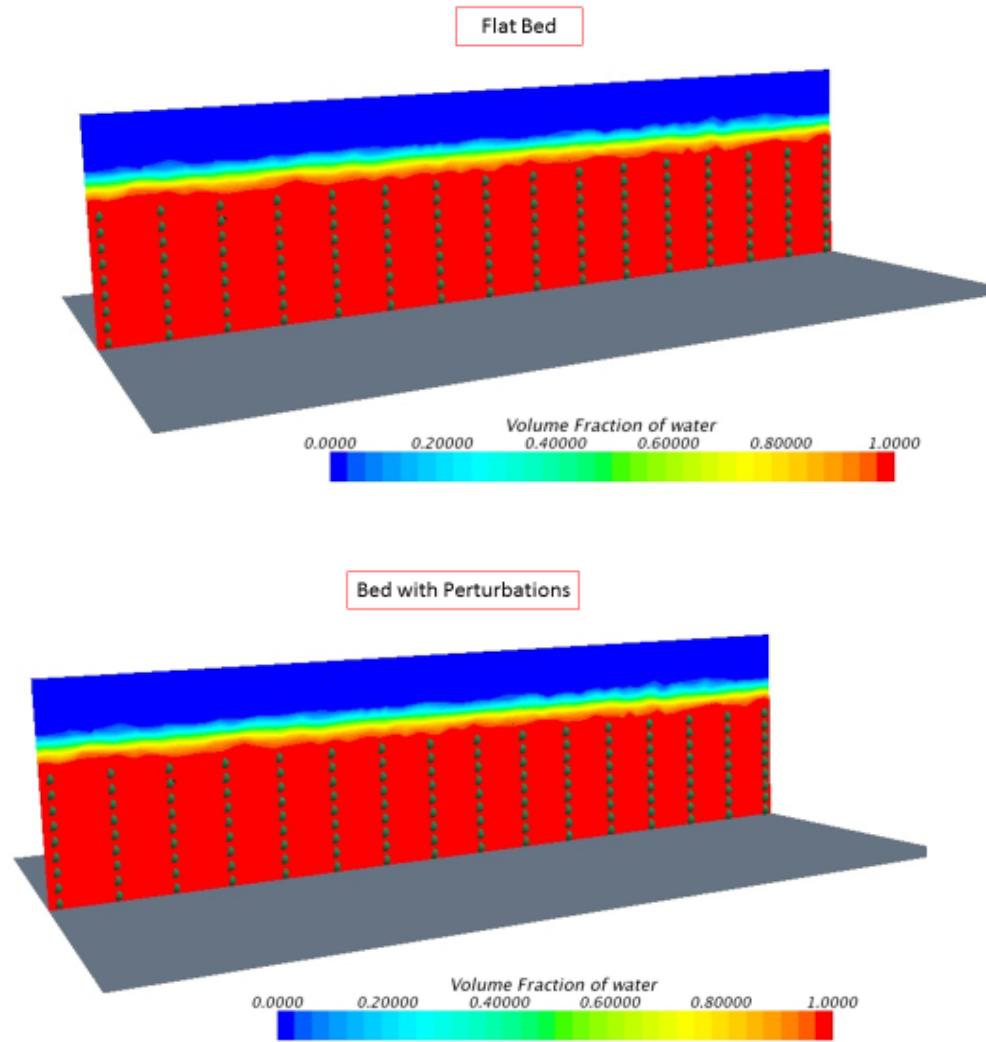


Figure 4.6 Location of the plane and state of the free surface

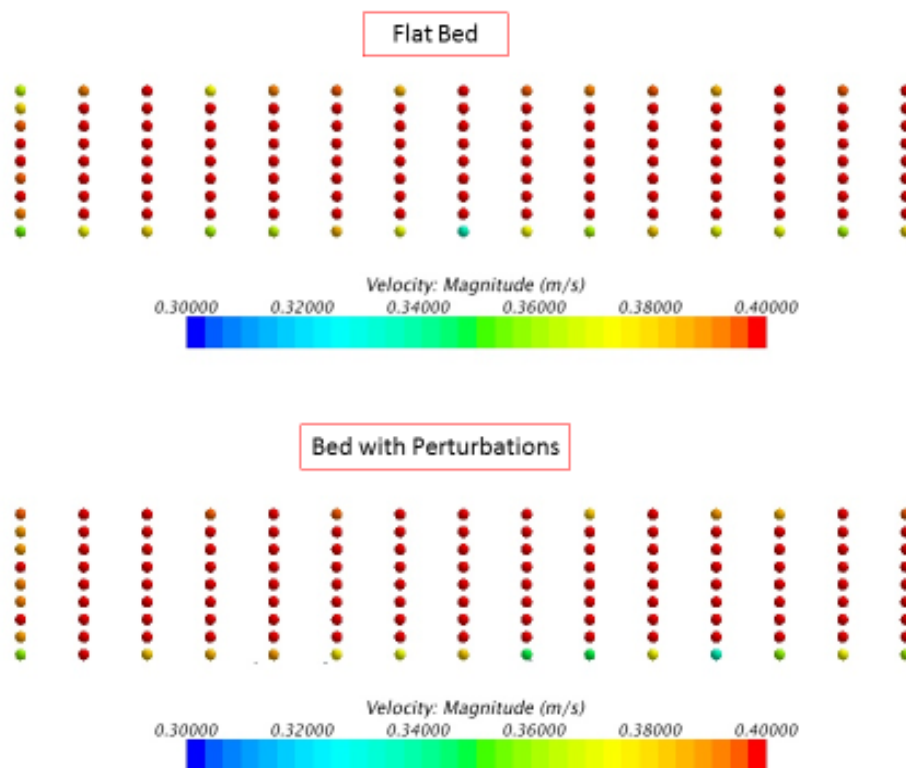


Figure 4.7 Velocity distributions on the plane

Figure 4.7 is a comparison of the velocity distribution between the case with a completely flat bed and the case for a bed with small perturbations. The main differences of these two cases are in the near-wall region and in the region close to the free surface. The difference in the region near the free surface is mainly caused by the VOF model and size of the mesh cell. The average velocity of these points for the case with the flat bed (\overline{U}_f) is 0.4082 m/s and the average velocity of the other case (\overline{U}_p) is 0.4087 m/s. The percent error is about 0.119% ($\text{error} = \left| \frac{(\overline{U}_p - \overline{U}_f)}{\overline{U}_f} \right| * 100\%$). The average of the error of velocity of each point is 3.60% and the standard deviation is 0.0317. The velocity error is larger than 10% for approximately 2.78% of the points. Moreover, about 50% of such

points are in the region close to the free surface. Based on the statistical analysis of the velocity distributions of these two cases, the influence of the perturbations is limited and negligible. Therefore, the bathymetry of the final CFD geometry does a good job of representing the physical experiment, even though the necessary adjustments import unwanted perturbations.

4.3 Mesh

There are two main challenges to mesh these CFD geometries. First, the irregular shapes of the scour hole and pier have a strong requirement for the shape and size of cells to maintain the shape with an appropriate number of mesh cells. Another problem is that there is a major difference among the sizes of different parts of the geometry. For example, the width of the tilting flume is 1.82 m and the thickness of the square H pile is only 0.2 mm. Therefore, denser meshes in regions around those small-size parts and near walls were necessary to maintain the shape of the CFD geometry and relatively coarse meshes in the regions far from the pier were necessary to restrict the number of mesh cells. Moreover, in order to avoid the negative influence of rapidly changing sizes of mesh cells, a smooth transform from large cells to small cells was strongly recommended.

The procedure of meshing in STAR-CCM+ has two steps: (1) creating a surface mesh for the CAD model or optimizing imported surface mesh; (2) creating the volume mesh based on the surface mesh. STAR-CCM+ offers three kinds of surface mesh models, “Surface Wrapper”, “Surface Remesher” and “Automatic Surface Repair”. Based on the quality of the imported geometry, one or more of them are activated to mesh the surface of the geometry to provide a quality discretized mesh that is suitable for CFD. In

this research, the quality of the imported original CAD models created by SOLIDWORKS was good enough, so only “Surface Remesher” was activated to generate the surface mesh. To do volume mesh for these CFD models, “Thin Mesher” and “Prism Layer Mesher” were activated. The “Thin Mesher” generates a prismatic layered volume mesh for thin geometries, where good quality cells are required to capture the solid material thickness adequately. Even though this mesh model increases the computational time and requires storage space more than other mesh models, like “trimmer”, it has a better capacity to mesh the complex shape of the scour hole around the pier and obtains more accurate results than other mesh models with a similar number of mesh cells. The “Prism Layer Mesh” was selected as an optional model, because the function of this model can generate a denser (or coarser) mesh in near-wall regions and set a specific cell size to satisfy the requirements of wall function and roughness function. The volumetric control was activated to set a specific size of mesh cell to maintain the shape of the leading and trailing edges of the pier, the interjection of the upper half and lower half of the pier and the shape of the H piles. The volumetric control was also applied to ensure the transform of size of mesh cells smooth. As shown in Figure 4.8, Cylinder 1 and Cylinder 2 define the pier regions and Block 1 covers the H piles, in which a denser mesh is needed to maintain the shape of the geometry. Block 2 covers the imported original CAD model. The mesh in these areas is denser enough to maintain the shape of the scour hole and interjection of the upper half and lower half of the pier.

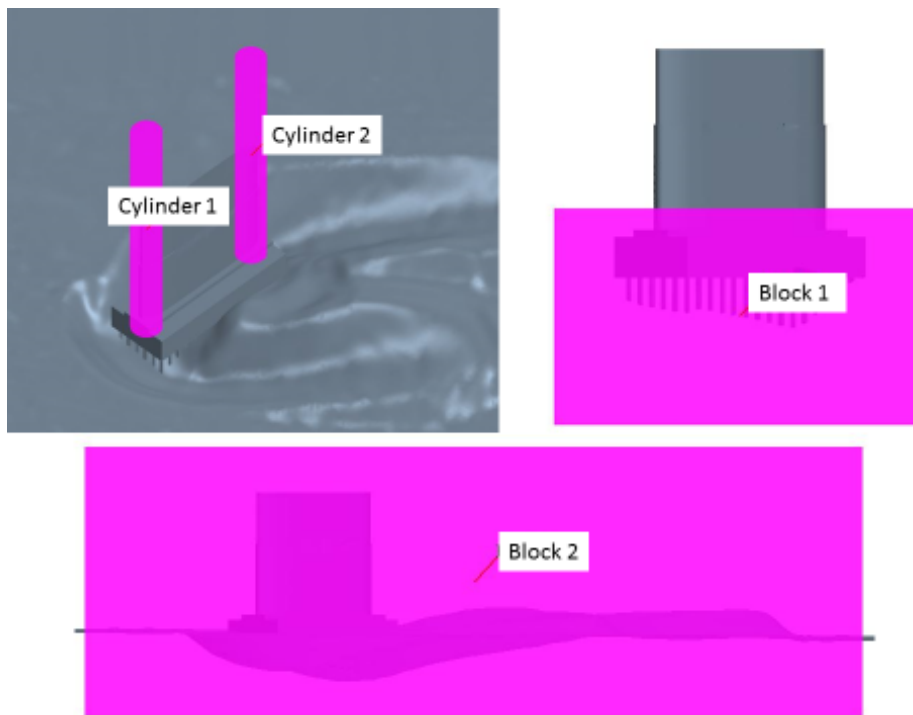


Figure 4.8 Volumetric controls of Case MF_O_50

The base size of these CFD models is set as 2 cm. In Cylinder 1, Cylinder 2 and Block 1, the custom size is 10% of the base size and the custom size of Block 2 is 50% of the base size. The size of the refined cells are 5%~25% of the base size. The number of mesh cells is about 12.3 million. Since the geometries of these CFD models are complex, it is possible that there are some potential problems in the mesh results, which may lead to the CFD simulation crash. Therefore, the procedure called “remove invalid cells” in STAR-CCM+ was taken to avoid these problems before running the simulation.

Figure 4.9 is an example of mesh under the setup described above. This mesh has a good capacity to capture the shapes of the leading and tailing edges of the pier and the H piles. There are three kinds of sizes of mesh cells: the smallest mesh cells around the pier; the middle-size mesh cells mesh the original CAD model; and the largest mesh cells

in the regions distant from the pier. With this kind of mesh cell distribution, the transform of the sizes of the mesh cells is relative smooth. Even though this kind of mesh satisfies the requirements of the geometry, the physical models also have additional requirements for the cell size. This will be discussed in the following sections.

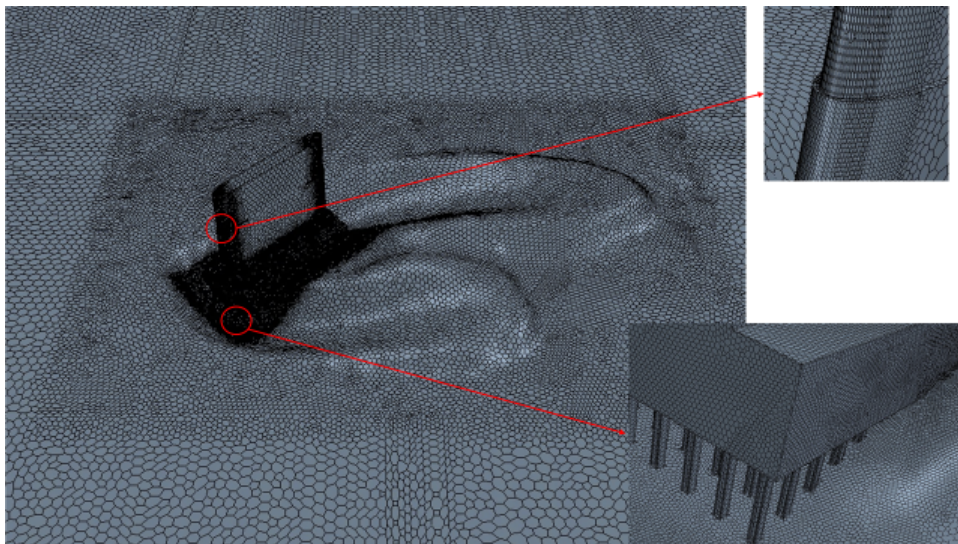


Figure 4.9 Mesh of Case MF_O_50

4.4 Physical Models

The CFD models were developed to simulate the open-channel flows of the physical experiments. Using an appropriate turbulence model, free surface model and wall function is the most significant task to ensure the accuracy of these models. All active physical continua models are shown in Figure 4.10. These physical models can be separated into four groups: (1) free surface model; (2) turbulence models; (3) wall function and (4) others. The models of the first three groups are the main physical models

to simulate water flows. The models in the fourth group are required or strongly recommended by models in the first three groups.

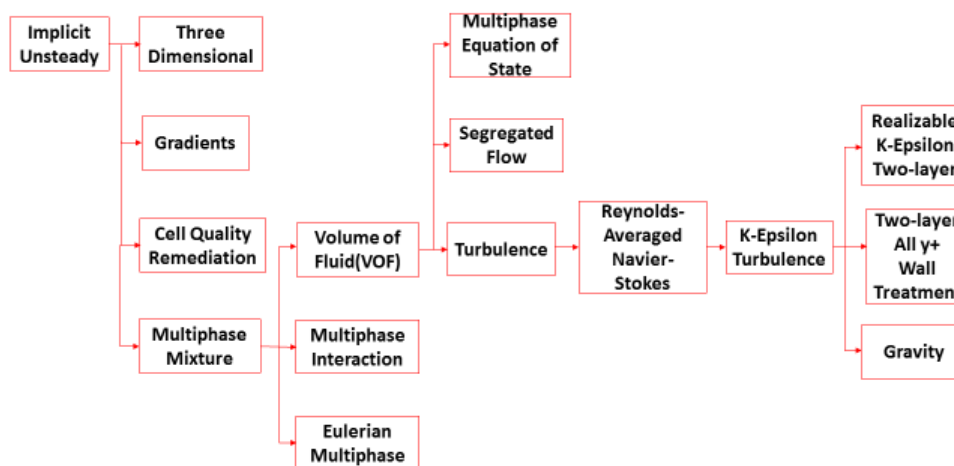


Figure 4.10 Physical continua models

“Volume of Fluid” (VOF) was activated to simulate the free surface. Since the focus of the CFD model is to obtain wall shear stress distributions and values around the pier and the water depth is large enough to eliminate the influence of the motion of the free surface on the bed, the most significant purpose of VOF is to guarantee the water flow in the geometry is open-channel flow. VOF in STAR-CCM+ (version 9.06 and before) is only available for unsteady simulations. This leads to a conflict between the physical experiment and the CFD model. In the physical experiment, the shape of the bathymetry actually is the state of the bathymetry at a certain moment. While, the unsteady CFD simulation is generally used to model a process of the fluid flow. Thus a long physical time is required for these CFD models to approach a quasi-steady state.

In this research, the realizable K-Epsilon model and RANS mode were activated to simulate turbulent flow. The Realizable K-Epsilon model is a successfully recent developed turbulence model (Shih, 1994), which is recommended for use with RANS to simulate unsteady turbulent flow (STAR-CCM+ user guide, 2012). This model was developed from the standard K-Epsilon model. The main advantage is that a critical coefficient of this model is expressed as a function of mean flow and turbulence properties, which was assumed as a constant in the standard K-Epsilon model. Therefore, this model satisfies certain mathematical constraints on the normal stresses consistent with the physics of real turbulence.

“Two-layer All y^+ Wall Treatment” was applied to simulate water flows in near-wall regions. The wall functions are a set of semi-empirical functions used to satisfy the physics of water flows in near-wall regions. It has a close relation with the distribution of wall shear stress. In STAR-CCM+, there are three kinds of wall functions: (1) high y^+ wall treatment for coarse mesh (2) low y^+ wall treatment for fine mesh and (3) all y^+ wall treatment. The third wall function is a hybrid treatment that attempts to emulate both the first and second functions. With this model, one does not have to go through the simulations and specify which walls need to use the low y^+ wall treatment and which walls need to use the high y^+ wall treatment. Moreover, the velocity vectors given by combining the two-layer model and any turbulence model are physically meaningful (Kim J Y et al., 2005).

There are also some other physical models in Figure 4.10. Some of them are preconditions of the physical models in the first three groups or auto-selected by STAR-CCM+ itself after activating other physical models. For example, “Multiphase Mixture”

is a precondition of VOF and “Multiphase Equation of State” was auto-selected with VOF. Some of them were strongly recommended to ensure these CFD models work. For example, “Cell Quality Remediation” is a physical model to eliminate the cells whose volume is zero or even negative, which causes the simulation to crash or the discrete governing equations to not converge.

4.5 Necessary Setup

The flow condition of each CFD simulation came from the physical experiments. Before running the CFD simulations, there are still some necessary steps. One of the most important settings of the CFD model to simulate the open-channel flow is to define the initial regions of water and air. STAR-CCM+ allows users to define field functions, which are powerful for accessing field data and sharing a particular set of properties. The initial regions of air and water and the inlet velocity values of air and water need to be separately defined. Table 4.2 shows these user field functions and Figure 4.11 shows the initial solution of Case Q100_O_50.

Table 4.2 User field defined for the initial flow condition

Name	Function	Definition
water	Define water domain	$\$Position [1] \leq water_depth? 1: 0$
air	Define air domain	$1-\$water$
v	Define velocity	$[\$Position[1]<water_depth?average_inlet_velocity:0,0,0]$

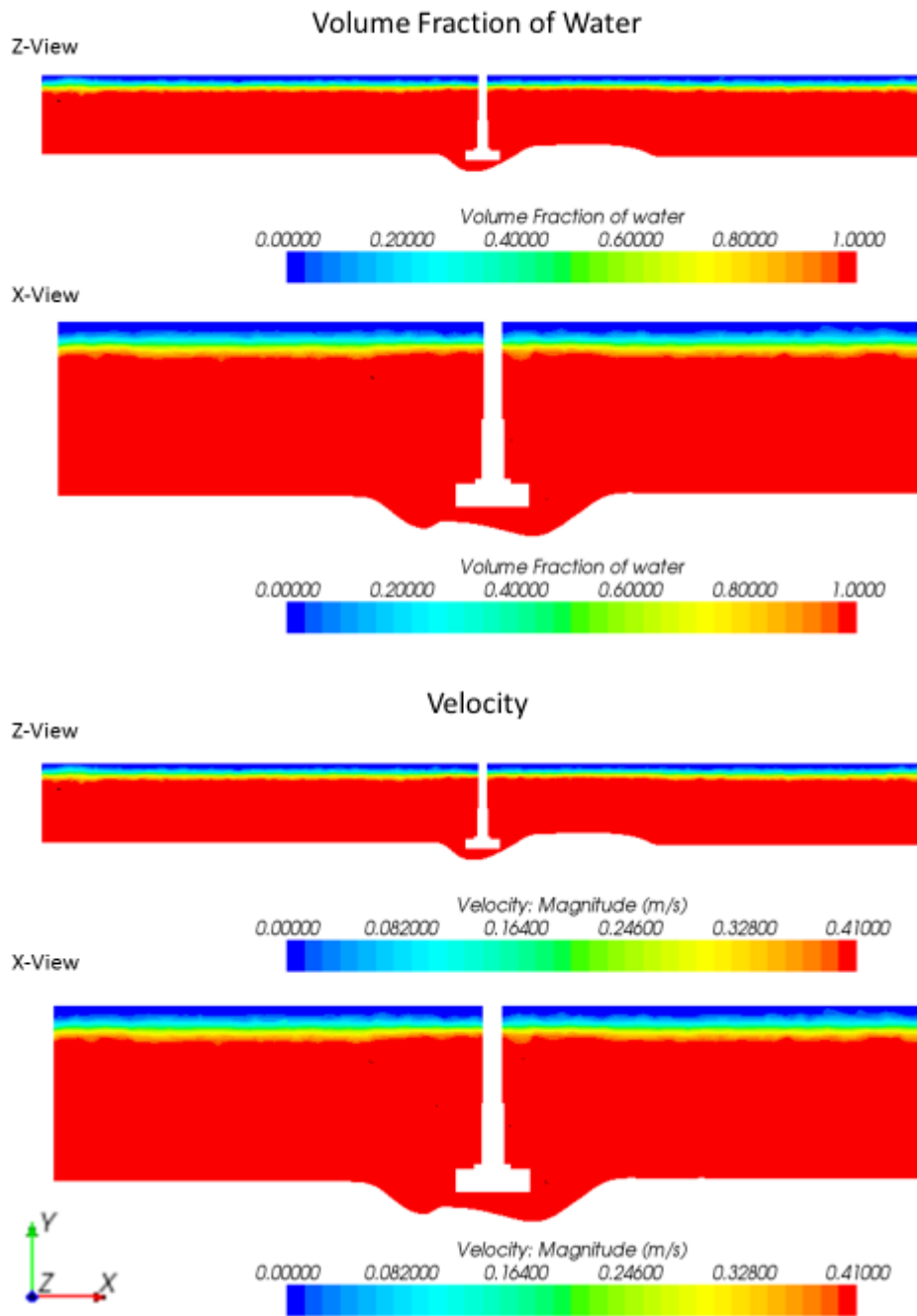


Figure 4.11 Initialize solution for the Case Q100_O_50

Another problem is that the wall shear stress result calculated with the built-in STAR-CCM+ wall shear stress field function always contains a non-zero component

normal to the wall. So the function is more appropriately called “Wall Stress”, which also widely exists in other commercial CFD codes. CD-adapco technical states that the quantity of wall shear stress is more appropriately to be calculated with Eq.4.1.

$$\tau_w = \tau \frac{dA}{|A|} \quad (4.1)$$

where dA is the area vector, $|A|$ is the area of the mesh cell and τ is the stress tensor on the wall. In turbulent flows using wall functions, the tangential component of τ is subtracted off and replaced with the tangential component computed from wall functions (https://wiki.anl.gov/tracc/STAR-CCM%2B_Technical_Notes). Table 4.3 shows the calibration of wall shear stress by using user field functions, part (a) of which calculates the normal component of wall shear stress and part (b) calculates the tangential component of wall shear stress. The tangential component was used as the CFD modeling result.

Table 4.3 User fields defined for wall shear stress

(a) Normal component of wall shear stress

Property	Value
Type	Vector
Dimensions	Stress
Function Name	sigmaW
Definition	$\text{dot}(\$ \$ \text{WallShearStress}, \text{unit}(\$ \$ \text{Area})) * \text{unit}(\$ \$ \text{Area})$

Table 4.3 (continue) User fields defined for wall shear stress

(b) Tangential component of wall shear stress

Property	Value
Type	Vector
Dimensions	Stress
Function Name	tauWS
Definition	\$\$WallShearStress-\$\$tauWS

4.6 Validation and Calibration of CFD Models

There are still three major questions that need to be answered. First, the size of mesh cell needs to be analyzed to optimize these CFD models. Second, since these CFD simulations are unsteady, an appropriate physical time is needed not only to make sure these cases become quasi-steady, but also to take a relatively short computational time. Finally, the activated mesh and physical models need to be verified and calibrated to ensure the CFD models accurately represent the physical experiments.

4.6.1 Influence of Size of Mesh Cell

The realizable K-Epsilon model of RANS does not specify a required for mesh size. However, there are still some requirements that need to be satisfied. First, the shape of the CFD geometry must be maintained, which has already been discussed in detail in Section 4.3. Moreover, STAR-CCM+ requires the height of the first cell on the surface edge to be larger than the roughness height of this surface. Therefore, the size of these cells in the CFD models should be larger than 2 mm, because the roughness height of the

bathymetry is 2 mm. Additionally, “All y^+ Wall Treatment” of STAR-CCM+ is recommended to be used in the range of y^+ is between 20 and 200 by users, out of which the results may not be guaranteed to be accurate. The following equations were applied to estimate the height of the first cells next to the bathymetry.

$$Re = \frac{\rho U_{\infty} R_h}{\mu} \quad (4.2a)$$

$$C_f = [2 \log_{10}(Re) - 0.65]^{-2.3}; \text{ where } Re < 10^9 \quad (4.2b)$$

$$\tau_w = C_f * \frac{1}{2} \rho U_{\infty}^2 \quad (4.2c)$$

$$u^* = \sqrt{\frac{\tau_w}{\rho}} \quad (4.2d)$$

$$h = \frac{y^+ \mu}{\rho u^*} \quad (4.2e)$$

where ρ is the density of water, U_{∞} is the average inlet velocity, μ is the dynamic viscosity, R_h is the hydraulic radius, y^+ is the dimensionless wall distance of the first cell on the bathymetry and h is the height of this cell. Since the width of the flume (18.3 m) is much larger than the water depth (0.16m or 0.26m), the hydraulic radius here was replaced with water depth. Table 4.4 shows the estimation of wall distance for these two kinds of flow conditions. The roughness height is in the estimated range. The h value of the current mesh is 2.5 mm, which is acceptable.

Table 4.4 Estimation of wall distance

Flow Condition	Inlet Velocity (m/s)	Water Depth (m)	y^+	Re	H (mm)
MF	0.34	0.16	20~200	61000	0.92~9.2
Q100	0.41	0.26	20~200	120000	0.82~8.2

Other CFD simulations with two other kinds of meshes were conducted to analyze the influence of cell size. The current mesh is called a “fine mesh”. One kind of mesh was generated by doubling the base size of the “fine mesh”, called a “coarse mesh”. Another one was generated by halving the base size of the “fine mesh”, called a “very fine mesh.” Therefore, the h values of the coarse mesh and very fine mesh are about 5 mm and 1.25 mm, both of which are in estimated the range. Table 4.5 gives the amount of cells of these three kinds of mesh.

Table 4.5 Number of mesh cells

-	coarse mesh	fine mesh	very fine mesh
Number	237259	1239933	2427206

Even though a small number of mesh cells reduces the computational time and required storage space, the coarse mesh has poor capacity to capture the shape of the CFD geometry. As shown in Figure 4.12 (A), the original shape of the leading edge of the pier is elliptical, while there is an obvious shape change after meshing. Figure 4.12 (B)

shows the shapes of the H piles after meshing become irregular and some unwanted sharp curves are imported. Moreover, as shown in Figure 4.12 (C), the transition from large cells to small cells is not as smooth as for the fine mesh. Therefore, this kind of mesh is not an ideal mesh for these CFD models and the simulation results based on this mesh are doubtful and unacceptable.

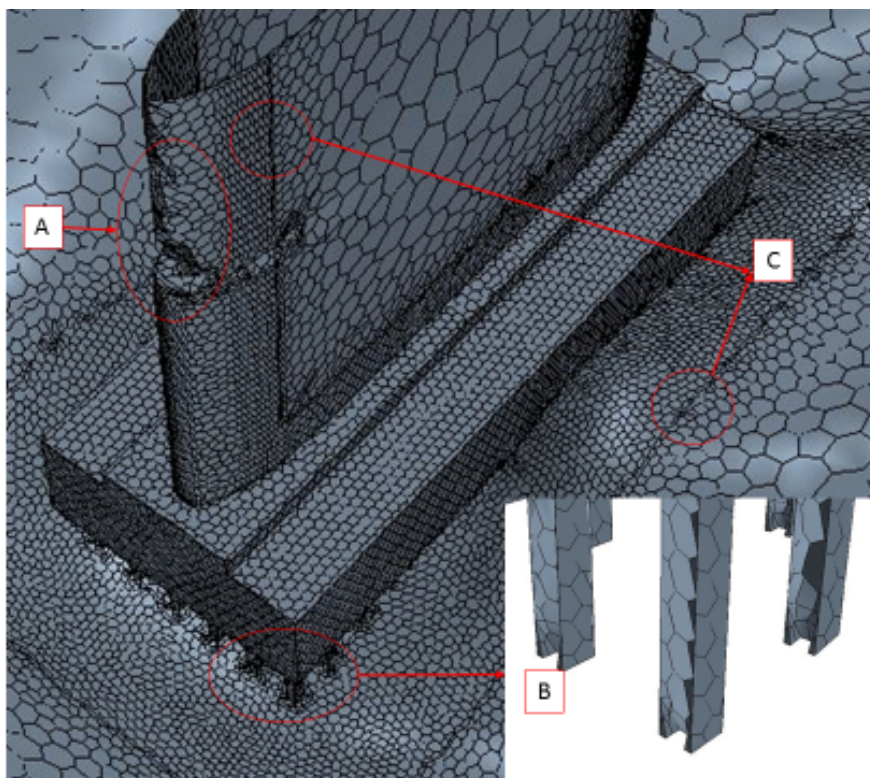


Figure 4.12 Coarse mesh

Generally speaking, the smaller size of mesh cell is, the more accurate the CFD simulation is. The “fine mesh” and the “very fine mesh” are compared in Figure 4.13. Both of them have a good capacity to capture the complex shape of the CFD geometry. The number of mesh cells of the “very fine mesh” is almost two times of that of the “fine

mesh”. Thus, the “very fine mesh” has higher requirements for storage space and takes a longer computational time for the CFD model to approach a quasi-steady state.

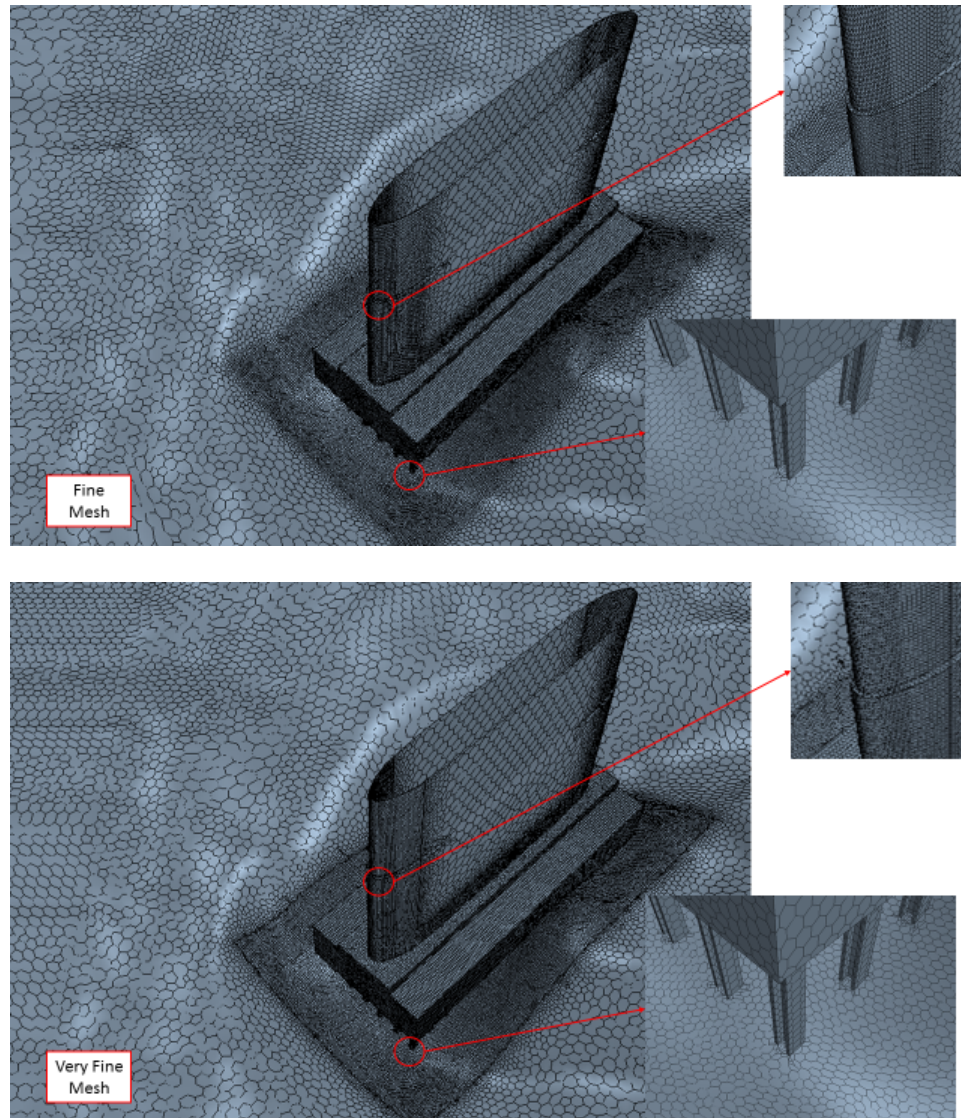


Figure 4.13 Fine mesh and very fine mesh

In Figure 4.14, the wall shear stress distributions of these two cases are very close to each other. So the influence of the size of these two kinds of mesh cells on the

accuracy of the CFD model is not very obvious. But the file size of the “very fine mesh” is about 1.9 GB, while that of the “fine mesh” is only about 1.4 GB. And with the same physical time, the computational time of the case with the “very fine mesh” is 48020 seconds, which is more than twice that of the case with the “fine mesh” (22942 seconds). There are still some differences between the computed wall shear stress distributions in some areas. One of the main reasons is the influence of the height of the first cells next to the bathymetry. The minimum height of the cells next to the bathymetry must be larger than the roughness height. In this research, the roughness height is 2 mm. The height of the cells next to the bathymetry of the “very fine mesh” is only about 1.25 mm. Thus the “very fine mesh” has a relatively weak capacity to accurately calculate the wall shear stress distribution and values. Therefore the “very fine mesh” is not an appropriate mesh for these CFD models, yet.

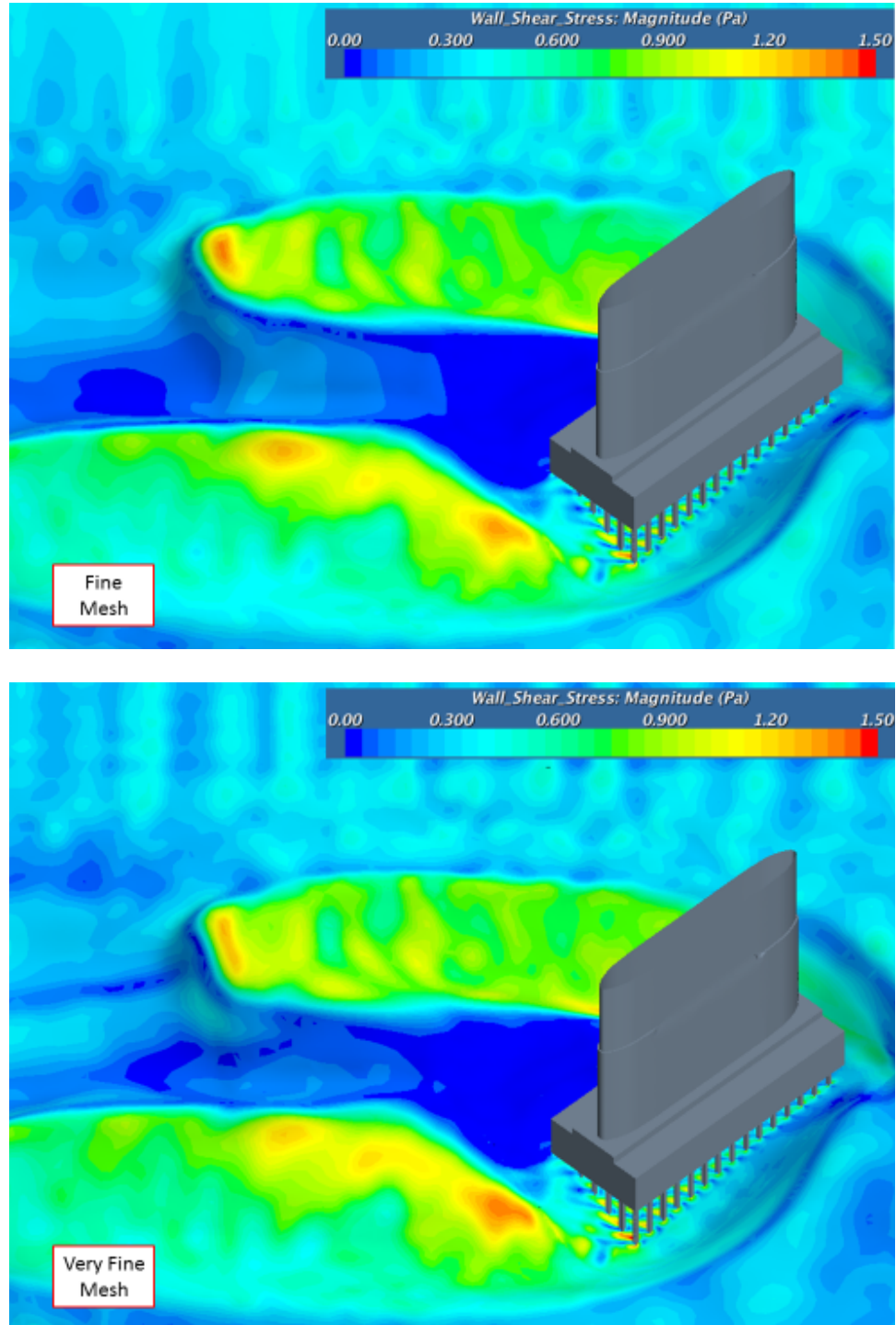


Figure 4.14 Wall shear stress distributions of these two cases

Even though the “fine mesh” was taken for these CFD models, it is still possible to have another kind of mesh, which not only satisfies all requirements but also has a relative low requirement for computer capacity. Because the “fine mesh” has a good capacity to capture the CFD geometry and accurately calculate wall shear stress distributions with an acceptable computational time, to find out the most appropriate mesh does not make too much sense. Figure 4.15 is another example of the fine mesh.

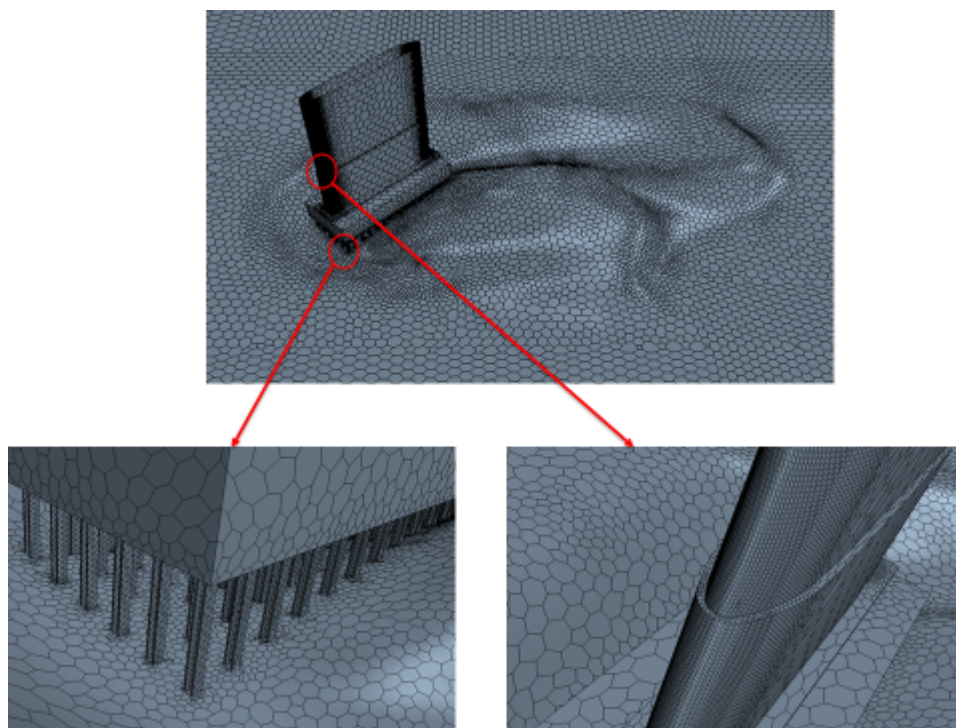


Figure 4.15 Mesh of the case MF_O_75

4.6.2 Quasi-Steady State

As discussed above, there is an inconsistency in these CFD models: the VOF model requires the CFD simulation to be unsteady, and the surveyed bathymetry is the state at a certain moment, for which a steady CFD model is more suitable. Therefore, a long physical time is necessary for these CFD models to approach quasi-steady state. The preliminary simulation results show that the shear stress distribution regularly vibrates with time under the quasi-steady state. This vibration can be explained with the well-known Karman vortex stress theory. For cases with a flat bed, this phenomenon is more obvious, as shown in Figure 4.16. Even though there are some differences among the wall shear stress distributions at different moments, the shear stress distribution around the pier are very similar to each other. So 20 seconds is a long enough physical time for cases with a flat bed to become quasi-steady.

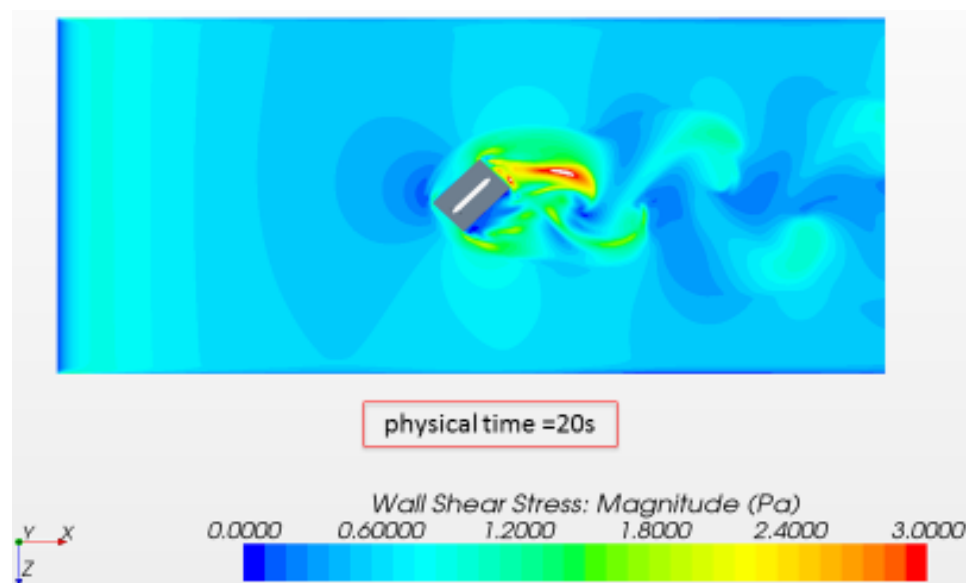


Figure 4.16 Wall shear stress distribution of Case Q100_R_0

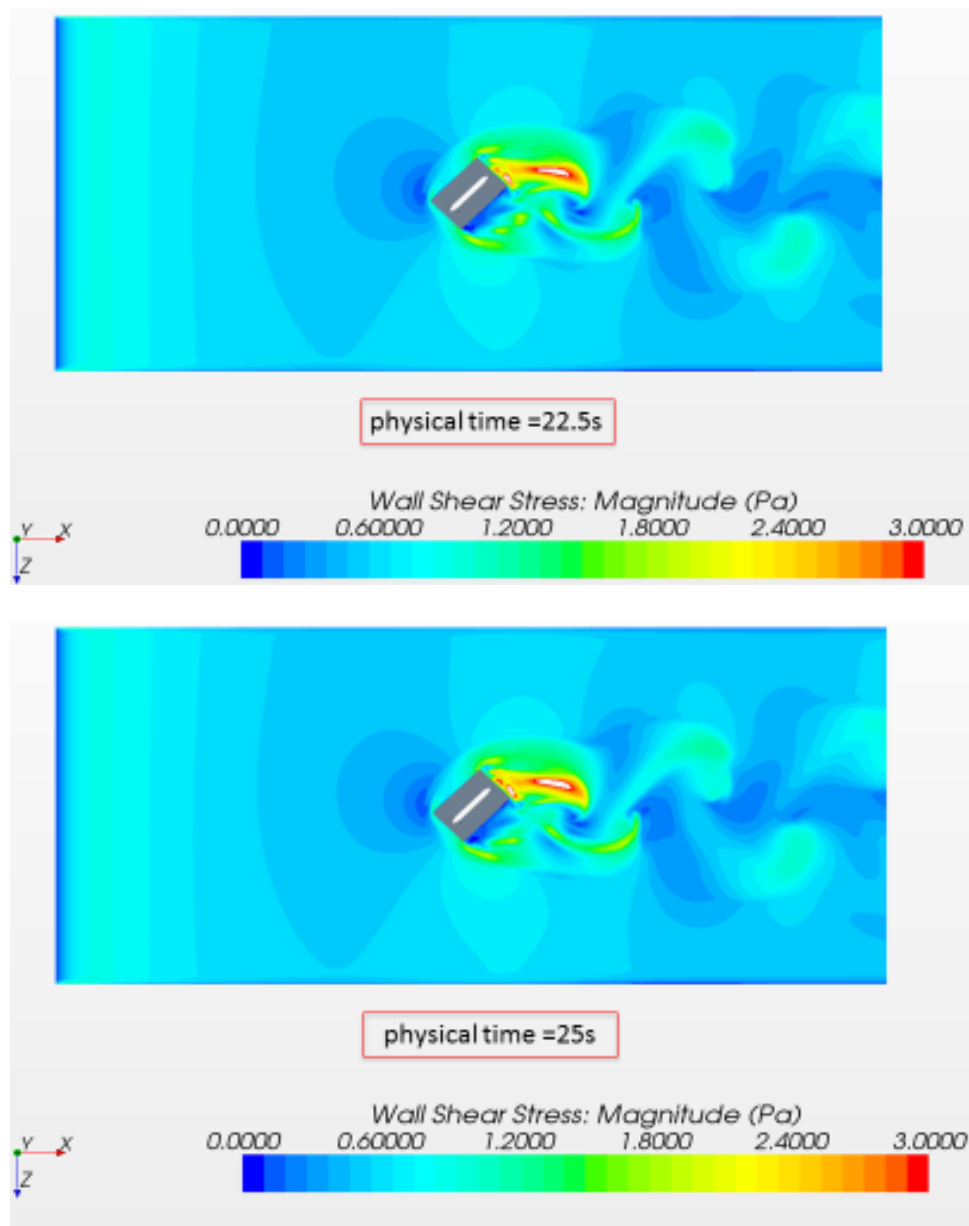


Figure 4.16 (continue) Wall shear stress distributions of Case Q100_R_0

For cases with a surveyed bathymetry, the scour hole around the pier inhibits this phenomenon, as shown in Figure 4.17. After 20 seconds of physical time, the wall shear stress distribution around the pier does not have an obvious difference at different moments.

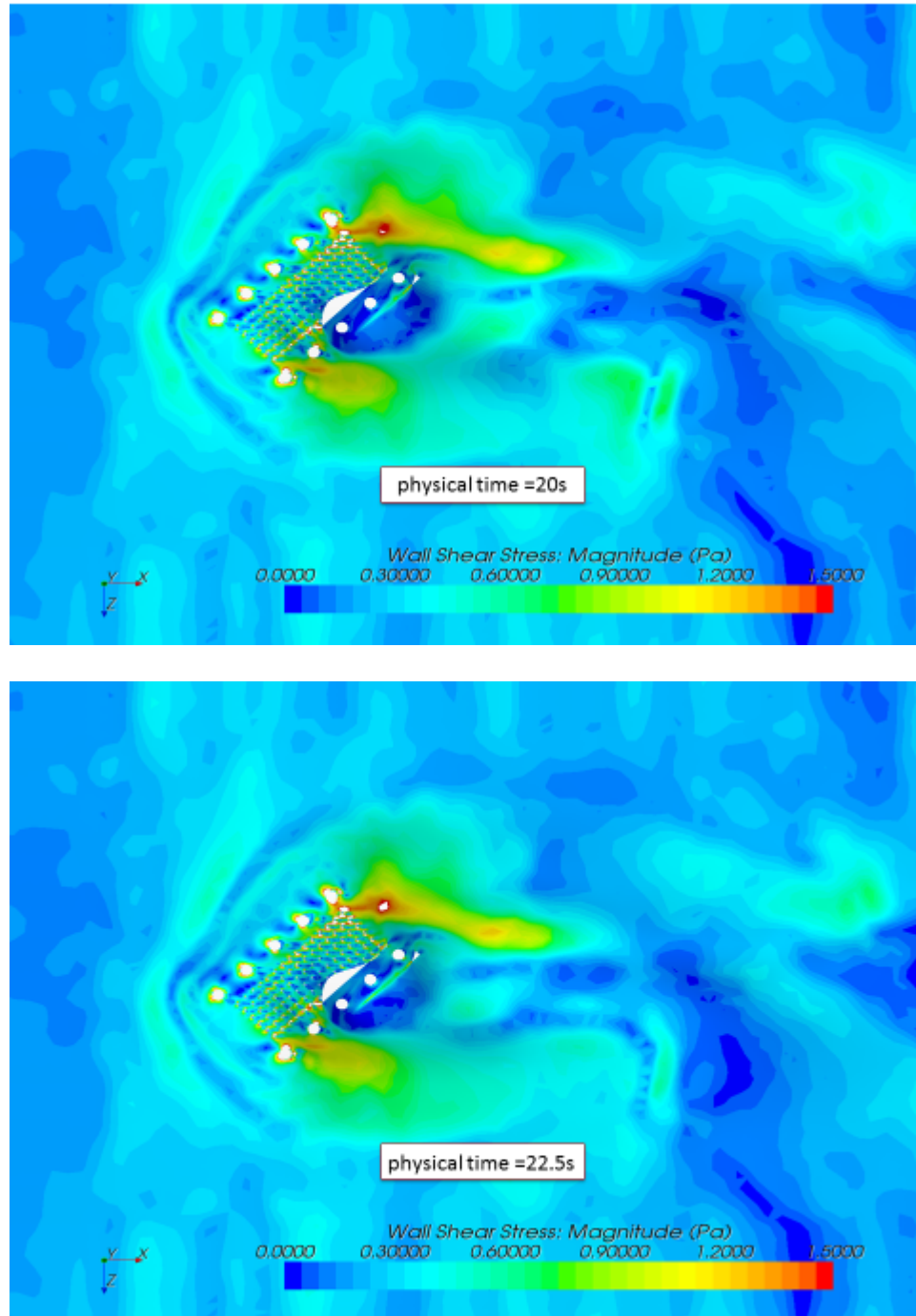


Figure 4.17 Wall shear stress distributions of Case Q100_R_50

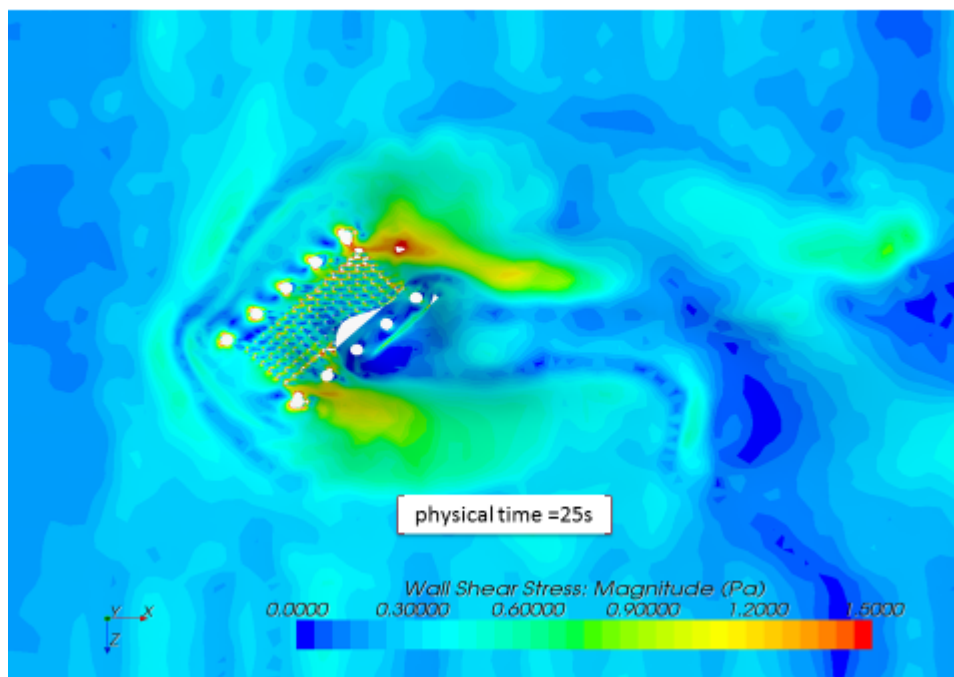


Figure 4.17 (continue) Wall shear stress distributions of Case Q100_R_50

Based on Figure 4.16 and Figure 4.17, after 20 seconds physical time, these unsteady cases become quasi-steady and the wall shear stress distribution around pier is relative steady and reflects the state of the case in the physical experiment. In order to further prove 20 of seconds physical time is long enough for CFD models to become quasi-steady, the wall shear stress values around the pier of five cases of Group MF_O were exported every 0.1 second from 20s (physical time) to 25s (physical time). The time-averaged wall shear stress and the root mean squares (RMS) were calculated to analyze whether these CFD simulations have already been quasi-steady after 20s (physical time). Table 4.4 shows that the maximum RMS of each of these five cases is

very close to zero. Therefore, these simulations have already been quasi-steady, and the wall shear stress distributions and values were taken as the final simulation results.

Table 4.6 Maximum RMS of wall shear stress of MF_O

Case	Max RMS of Wall Shear Stress
MF_O_0	5.70023×10^{-7}
MF_O_25	3.86178×10^{-7}
MF_O_50	3.86×10^{-7}
MF_O_75	8.6474×10^{-7}
MF_O_100	1.38748×10^{-7}

4.6.3 Validation and Calibration of CFD Models

The combination of unsteady RANS model and VOF model is widely used by hydraulic researchers to simulate open-channel flow. There are many examples listed in Chapter 2. To verify and calibrate the physical models of these CFD simulations, they were applied to simulate the open-channel flow around a rectangle pier with 30° attack angle. And the simulation results were used to compare with the previous CFD models, which were developed by using DES models in Argonne National Laboratory. The bathymetries of these cases were surveyed from previous physical experiments. The properties of DES code determine that it has a better capacity to capture eddies and simulate the turbulent flow than unsteady RANS model. The geometries of these simulations are shown in Figure 4.18.

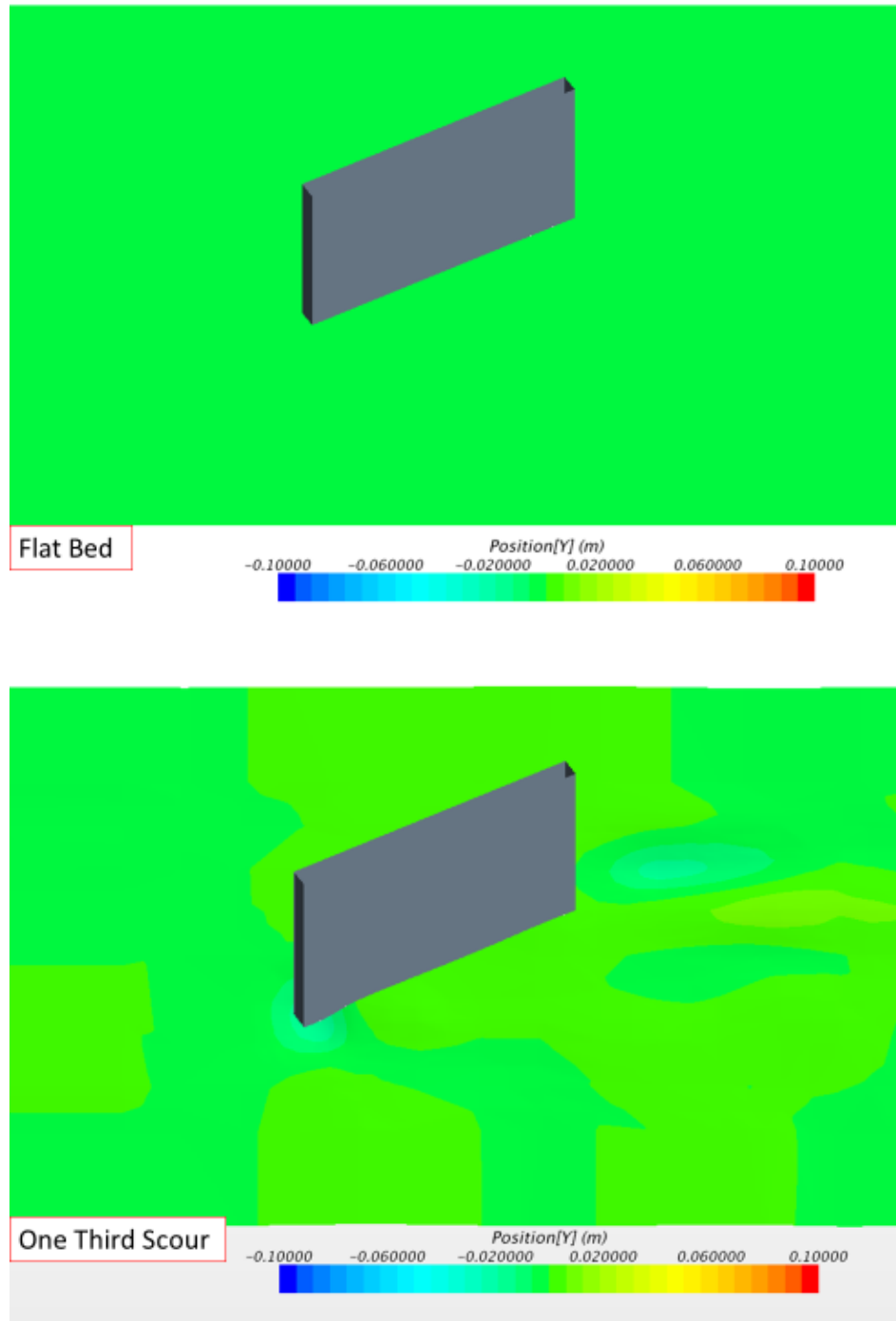


Figure 4.18 Bathymetries around the rectangle pier

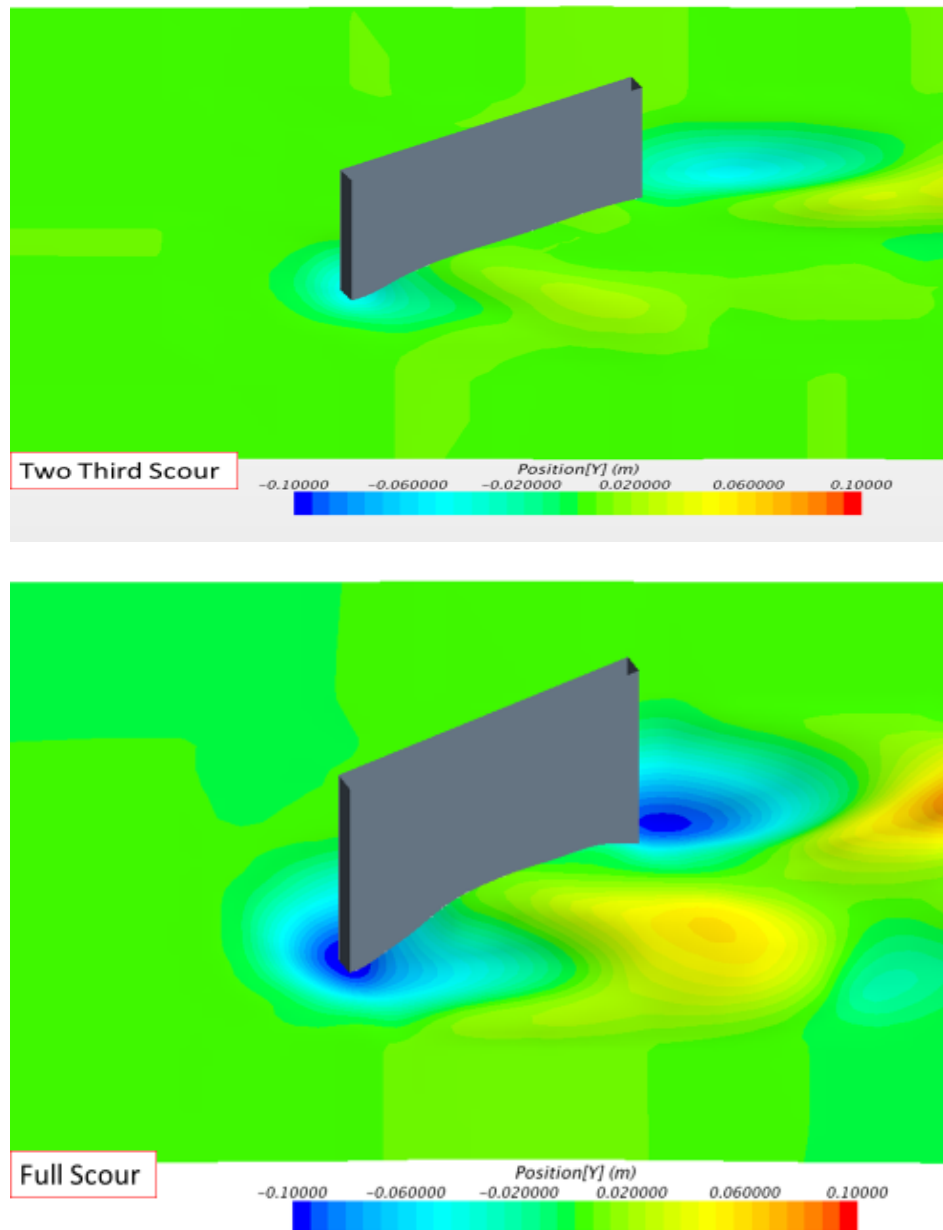


Figure 4.18 (continue) Bathymetries around the rectangle pier

Since the shape of this pier is regular and the shapes of the scour holes are not as complex as those around the Feather River Bridge pier model, “Trimmer” was activated as the volume mesh model to simplify the simulation and restrict the time cost. After 20 seconds of physical time, the CFD simulations become quasi-steady. The wall shear

stress distributions around the pier of these cases are shown in Figure 4.19. The wall shear stress distributions of CFD simulations with DES are in Figure 4.20.

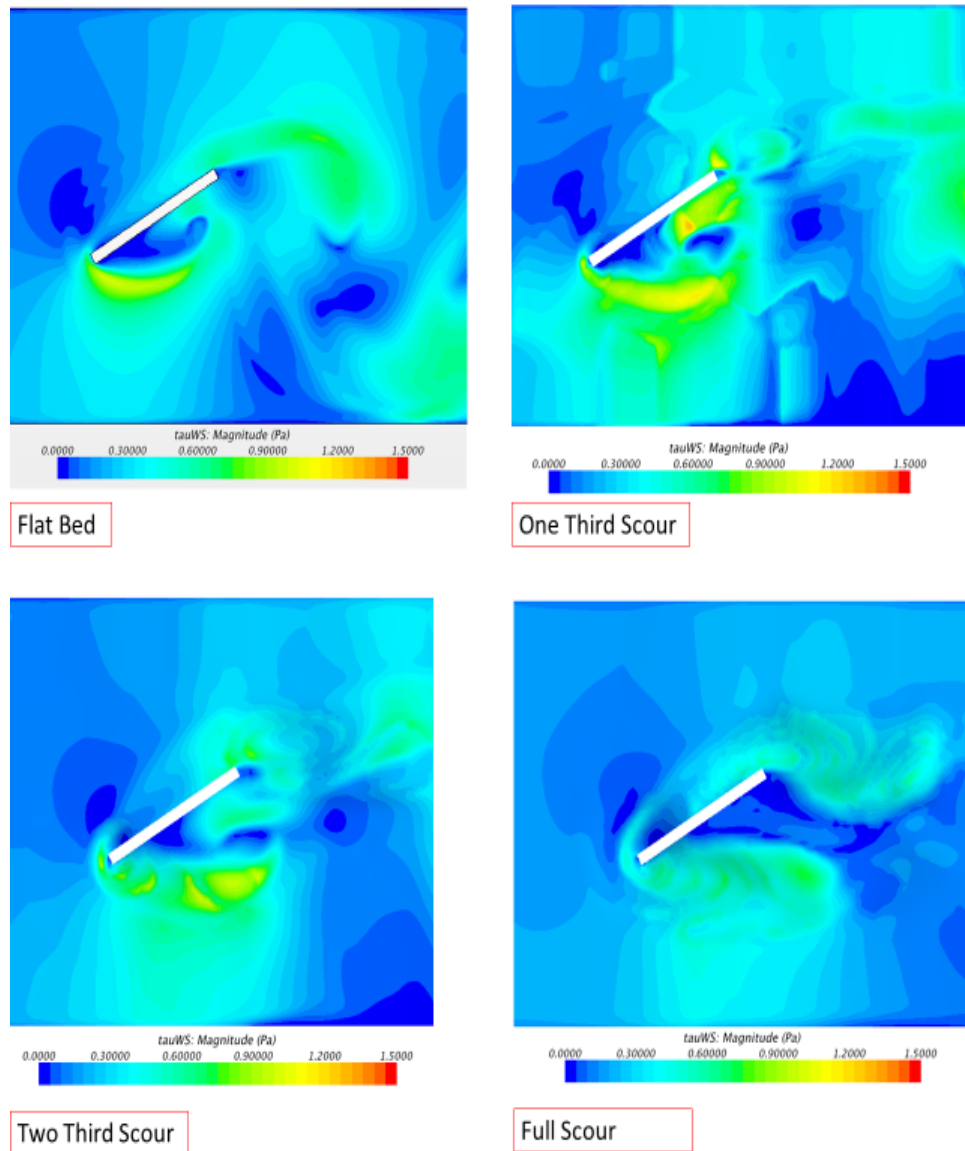


Figure 4.19 Wall shear stress distributions (RANS)

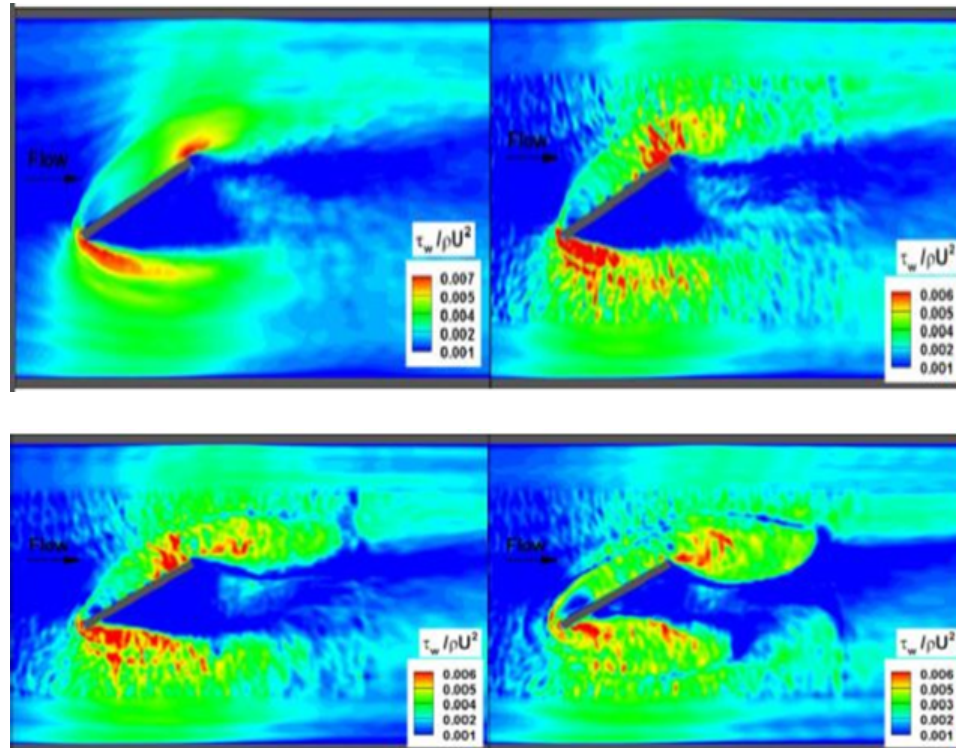


Figure 4.20 Wall shear stress distributions (DES)

Compared with the results simulated by using RANS model and DES model, the wall shear stress distributions around the pier are similar to each other. Since DES resolves eddies whose lengths are larger than the filter size, the wall shear stress distribution calculated with this model reflects the fluctuation of the turbulent flow. This leads to the differences between shear stress distributions in some areas in detail. The differences of wall shear stress values mainly come from the difference between the algorithms of these two turbulence models and wall functions. This difference can be calibrated with an appropriate numerical method in the postprocessor. Therefore, the activated unsteady RANS models of these CFD models can simulate the open-channel

flows around the scaled original pier and the scaled retrofitted design in the physical experiments.

4.7 Summary

In this Chapter, the development of CFD models for this research was described in detail by following the general procedure of the CFD method in STAR-CCM+. Related problems, which may occur during the development of CFD models, were discussed and resolved to eliminate potential mistakes. The influence of different kinds of mesh was analyzed to optimize these CFD models. Compared the simulation results using unsteady RANS model and DES model, the open-channel flow simulated with unsteady RANS model is reliable. All CFD simulations were conducted with the mesh models and physical models described in this chapter. The simulation results are listed in Chapter 5. And the development of the decay function of wall shear stress is discussed in the next chapter.

CHAPTER 5 Development of Decay Function of Wall Shear Stress

5.1 Overview

In this chapter, all simulated wall shear stress distributions of the physical experiments are presented to study the decay trend of wall shear stress with scour. Based on the simulation results of these CFD models, a decay function was developed to describe the relation between wall shear stress and scour depth. In order to calibrate this function to more accurately describe this trend, an envelope decay function was developed by combining the CFD data and the data of the previous physical experiments conducted by Annandale (Annandale and Smith, 2001). The simulation results of the CFD modeling for water flows around the rectangular pier, which were used to verify the physical models in Chapter 4, were used to verify these two decay functions.

5.2 Development of Decay Function of Wall Shear stress

The wall shear stress distribution on the bathymetry of each case, which was calibrated with the approach in Section 4.5, were directly exported from STAR-CCM+ after finishing the CFD simulation. The five wall shear stress distributions of each group listed in Table 3.2 were put together to analyze the trend of wall shear stress with scour. The wall shear stress values of selected points around the pier were taken to develop an appropriate function to describe this trend. Furthermore, the wall shear stress distributions on a flat bed under the same flow conditions around the scaled original and retrofitted piers were used to analyze the influence of the retrofitted design. The wall shear stress distributions around a given pier under the flow conditions of MF and Q100

were taken to verify the rapid increase of the water erosion capacity when a flood event occurs.

5.2.1 Wall Shear Stress Distributions

Figure 5.1 exhibits the wall shear stress distributions of Group MF_O. For the case with a flat bed (MF_O_0), the area with large shear stress is around the foundation of the pier. Therefore, scour first begins in this area. The particles of the earthen material in this area are removed by the water flow and a small scour hole forms in this area. For Case MF_O_25, the scour hole imparts shape-change, which increases wall shear stress values in some areas. But the shear stress values around the pier are smaller than those of MF_O_0. In Case MF_O_50, both the area and the depth of the scour hole become larger, while the area with large wall shear stresses become smaller and the values around the pier also become smaller. For Case MF_O_75, both of the area with large wall shear stresses and the values around the pier become even smaller. Finally, the wall shear stress distribution of Case MF_O_100 shows that there is not an area with obvious large wall shear stresses around the pier. Thus, it is very possible that scour stopped there, which These distributions reflect a clear decay trend of wall shear stress with scour, which is the expected result based on the literature review in Chapter 2.

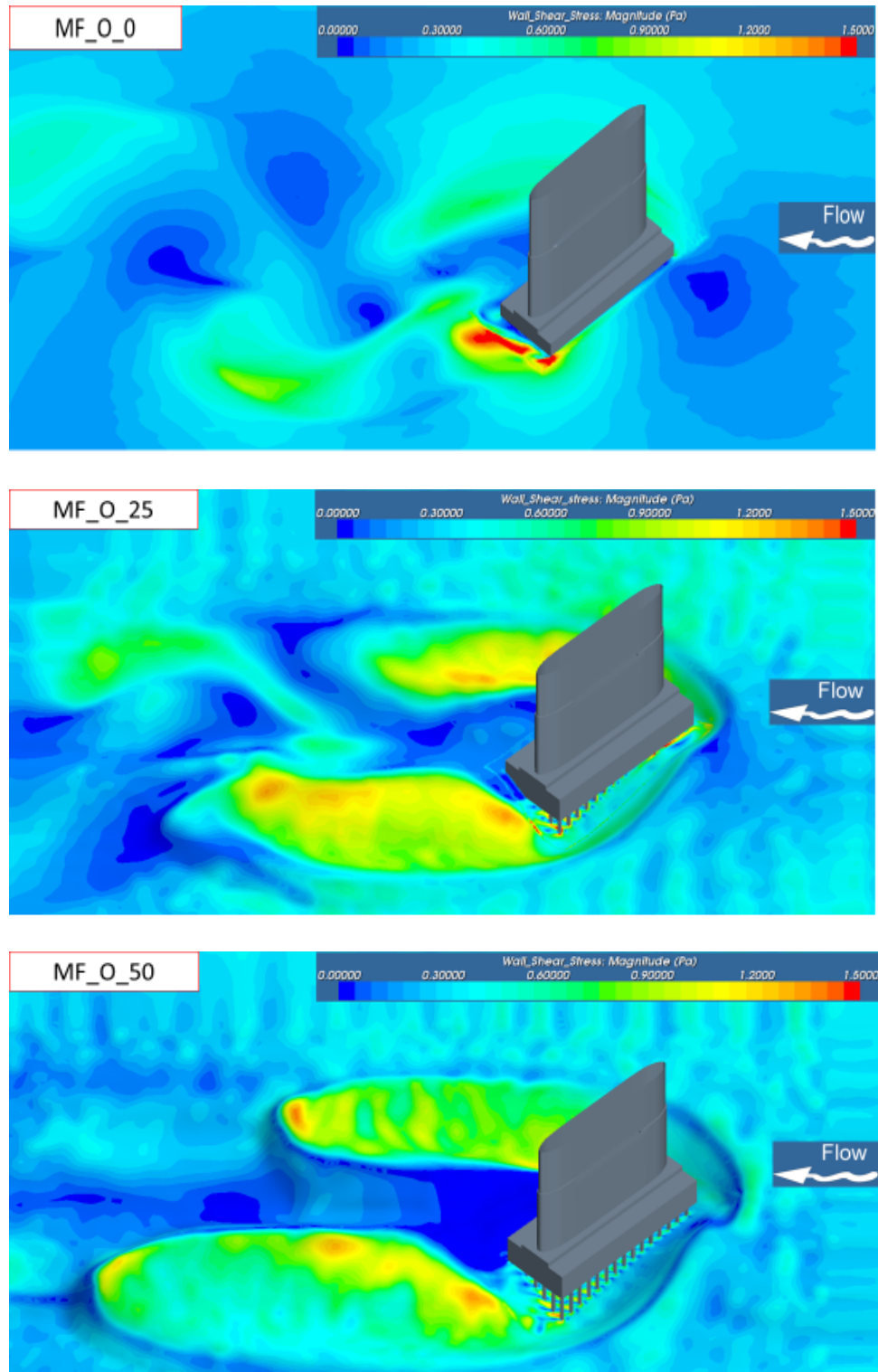


Figure 5.1 Wall shear stress distributions of MF_O

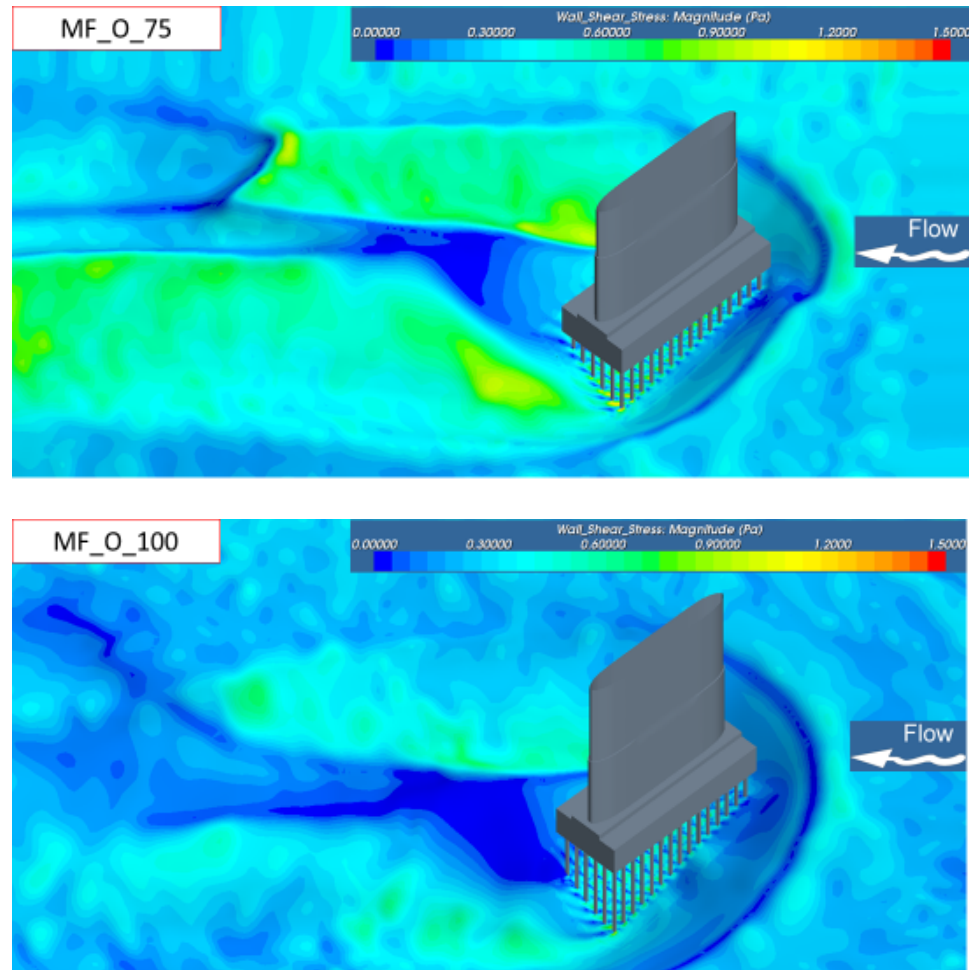


Figure 5.1 (continue) Wall shear stress distributions of cases in Group MF_O

The cases in this research can also be separated into two groups: cases with a flat bed and cases with a scoured bathymetry. For cases with a scoured bathymetry, the critical shear stress of clean non-cohesive sand is related not only to the d_{50} , but also to the location of the particle and the water flow direction. The bathymetries surveyed from the physical experiments shows that the particles in the area with the largest scour depth can be considered to be on a flat bed. So the critical shear stress of sand there is only related to the d_{50} . Moreover, the areas with the largest scour depth in cases with the same pier under the same flow conditions appear in nearly the same area. Therefore, the wall

shear stress values on these areas were picked as the final CFD simulation results of such cases. For cases with a flat bed, the maximum values of wall shear stress near the area, where the maximum scour depth would appear, were used as the final CFD simulation results. The given relative scour depth (Y_*) of MF_O and the wall shear stress amplification (τ_*) were plotted together to study the decay function of wall shear stress, which is also called the dimensionless wall shear stress. τ_* was calculated with Eq.5.1, where τ is the wall shear stress value of the final CFD simulation and τ_a was calculated with Eq.2.4.

$$\tau_* = \frac{\tau}{\tau_a} \quad (5.1)$$

The hydraulic radiuses (R_h) of MF and Q100 were given in Table 5.1.

Table 5.1 Hydraulic radiuses of MF and Q100

Flow Conditions	Water Depth (m)	Channel Width (m)	Hydraulic radiuses, R_h (m)
MF	0.16	1.82	0.136
Q100	0.26	1.82	0.202

Using the average approach velocity, Manning's n and initial flow depth, Eq.2.4 can be written as Eq.5.2.

$$\tau_a = \frac{(Vn)^2}{R_h^{1/3}} \rho g \quad (5.2)$$

The necessary data of Group MF_O is in Table 5.2 and the wall shear stress amplification and relative scour depth were plotted in Figure 5.2.

Table 5.2 Wall shear stress data of MF_O

	Y_*	τ_w (Pa)	τ_a (Pa)	τ_*
MF_O_0	0%	1.512	0.395	3.832
MF_O_25	29.04%	0.680	0.395	1.723
MF_O_50	45.19%	0.572	0.395	1.449
MF_O_75	60.49%	0.491	0.395	1.244
MF_O_100	100%	0.359	0.395	0.910

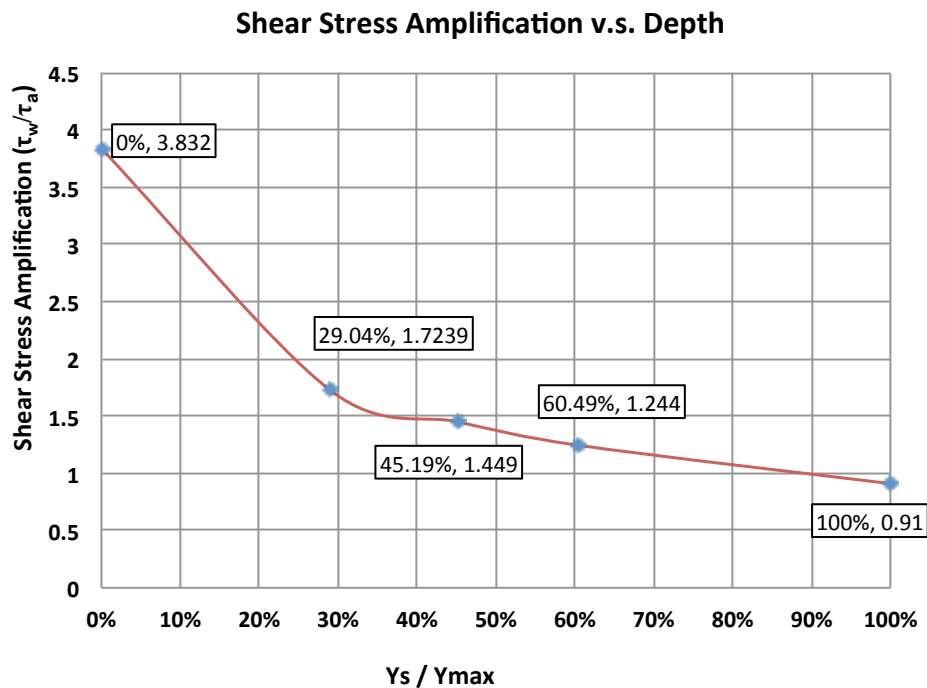


Figure 5.2 Decay Trend of wall shear stress of Group MF_O

The simulation results of Group MF_R reflect a similar decay trend of wall shear stress as that of Group MF_O. Figure 5.3 shows the geometry (left) and its wall shear stress distribution (right) of each case of Group MF_R. The scour first begins in the area with large wall shear stresses around the new cap of the retrofitted design of Case MF_R_0. And the shape change of the bathymetry increases the wall shear stress there in some areas. But the wall shear stress value around the retrofitted pier becomes smaller. Then the values of the wall shear stress around the pier decrease with the increase of scour depth. Finally, the wall shear stress around the pier is no longer large enough to keep moving earthen material particle. Therefore, it is very possible that scour stops at this moment. Other wall shear stress distributions are in Appendix B. The related data of Group MF_R are in Table 5.3.

Table 5.3 Wall shear stress data of MF_R

	Y_*	τ_w (Pa)	τ_a (Pa)	τ_*
MF_R_0	0%	2.176414	0.395	5.514
MF_R_25	44%	0.864434	0.395	2.190
MF_R_50	57.58%	0.774307	0.395	1.962
MF_R_75	76.38%	0.70098	0.395	1.776
MF_R_100	100%	0.541842	0.395	1.373

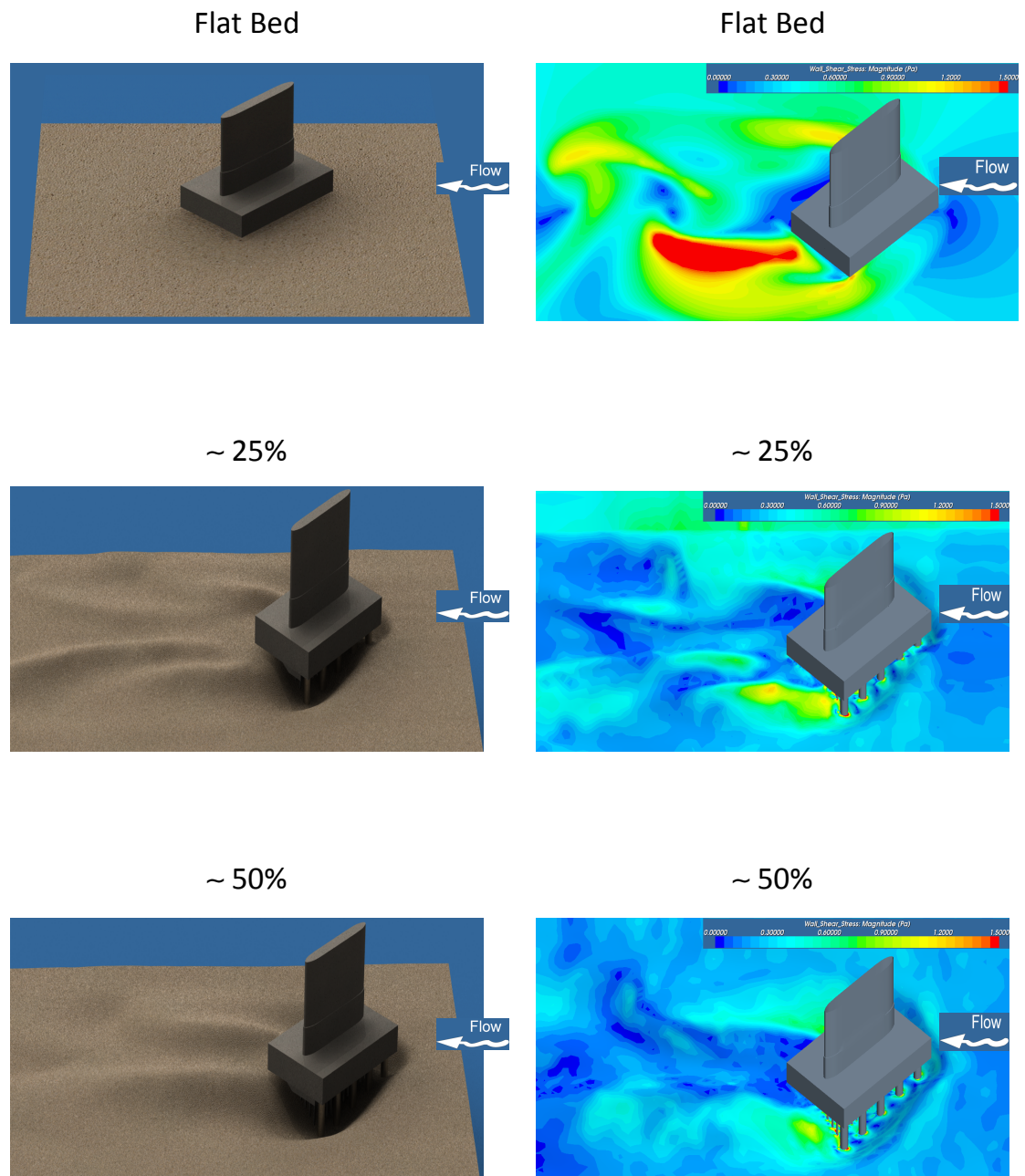


Figure 5.3 Geometries and wall shear stress distributions of cases in Group MF_R

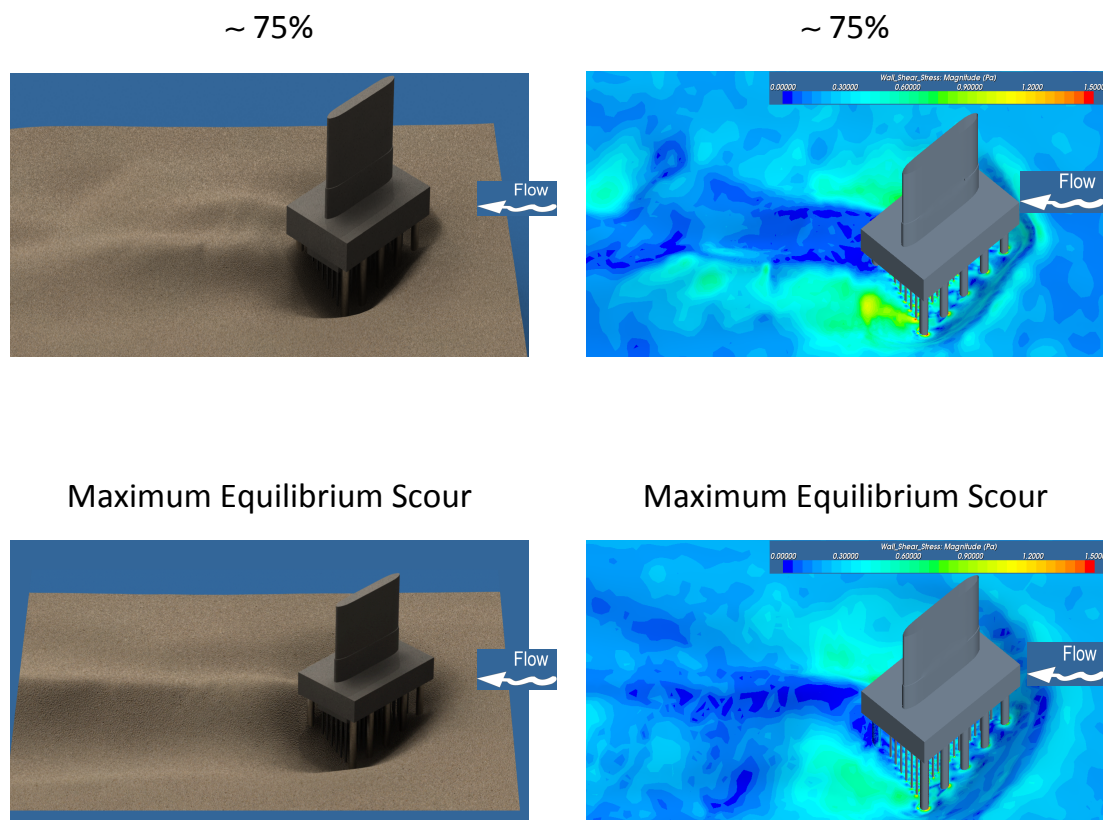


Figure 5.3(continue) Geometries and wall shear stress distributions of Case MF_R

The given relative scour depth (Y_*) of group MF_R and the wall shear stress amplifications (τ_*) were plotted together with the data of Group MF_O in Figure 5.4. The decay curves of Group MF_O and MF_R are similar to each other and share many similar properties. First, these two curves are nearly similar to each other by observing. This is evidence that they are controlled by the same mechanism. Both of these two curves rapidly decay initially and then the decay rate subsides.

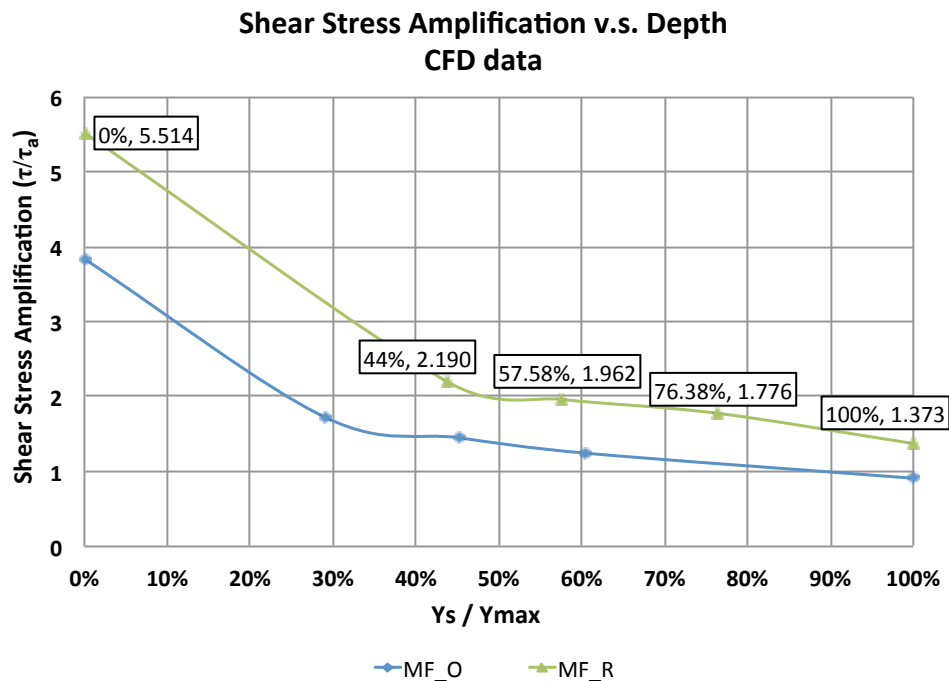


Figure 5.4 Decay trends of MF_O and MF_R

The influences of the retrofitted design and the flood event on the water erosion capacity were studied with these wall shear stress distributions. In order to eliminate the influence of different scour depths, the shear stress distributions of cases with a flat bed were used. The influence of the retrofitted design on the water erosion capacity was analyzed by comparing wall shear stress distributions of MF_O and MF_R, as shown in Figure 5.5. The area with large wall shear stresses around the retrofitted pier is obviously larger than that around the original pier. Therefore, this retrofitted design actually enhances the water erosion capacity under the same flow conditions and the same bathymetry. So the main purpose of this design is to restore the capacity of the stability of Pier 22, rather than to fix the pier scour problem.

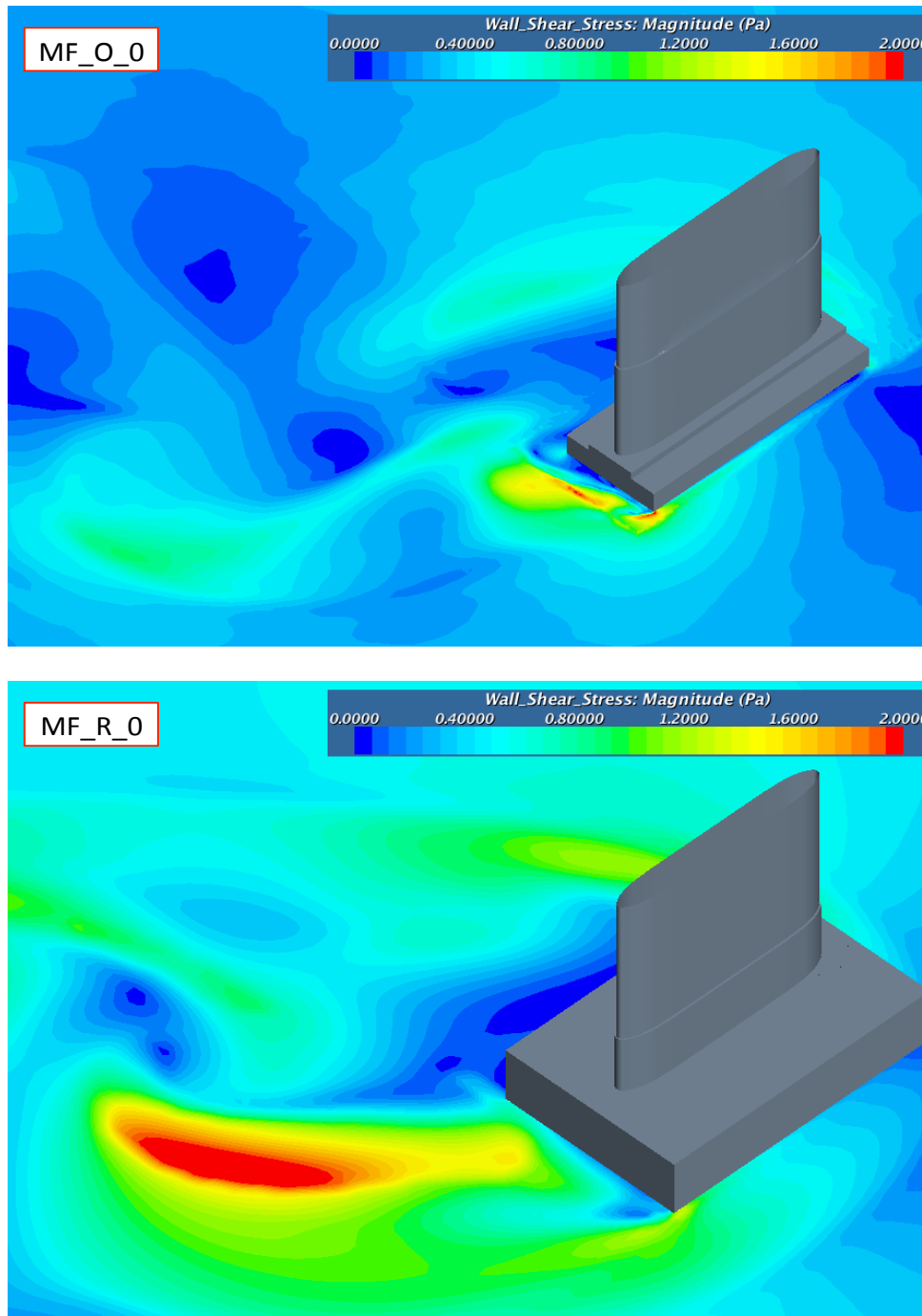


Figure 5.5 Wall shear stress distributions of MF_O and MF_R

Based on common sense, the flood event has a strong capacity to rapidly increase the water erosion capacity. Comparison of the wall shear stress distribution of MF_O_0

with that of Q100_O_0 (Figure 5.6) shows that the area with large wall shear stresses is markedly enlarged. It is very possible that the particles of earthen material in the area near the leading edge of the pier move faster and more easily when the flood event occurs.

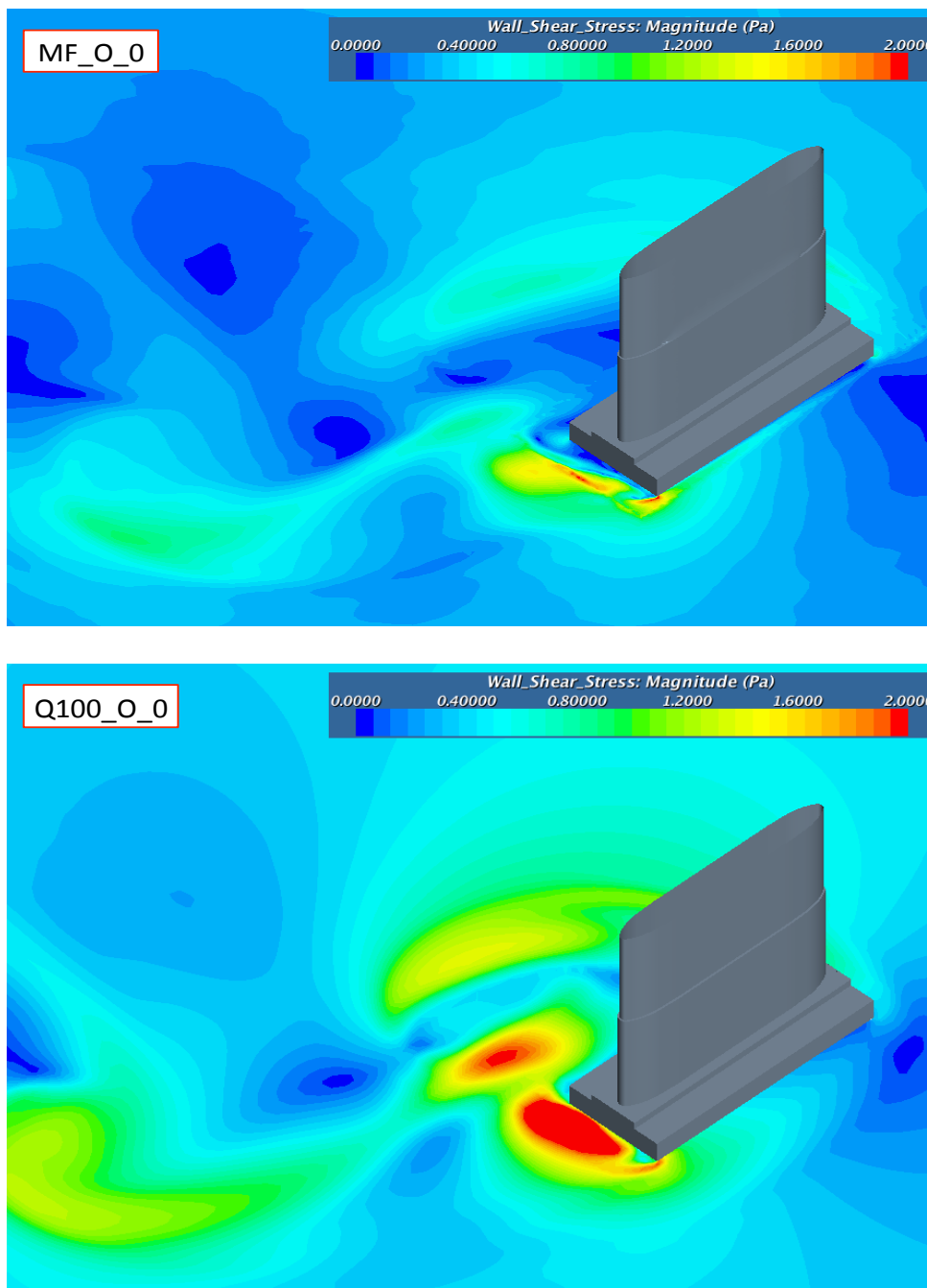


Figure 5.6 Wall shear stress distributions of Q100_O and Q100_R

5.2.2 Decay Function

Table 5.4 shows all necessary data to develop the decay function of wall shear stress amplification with relative scour depth. The relative scour depths were directly surveyed and calculated with the physical experiments. The wall shear stress amplification of each case was calculated with Eq.5.1 and Eq.5.2.

Table 5.4 Wall shear Stress Data

	Case	Y_*	τ_w (Pa)	τ_a (Pa)	τ_*
MF_O	MF_R_0	0.00%	1.512	0.395	3.832
	MF_R_25	29.04%	0.680	0.395	1.723
	MF_R_50	45.19%	0.572	0.395	1.449
	MF_R_75	60.49%	0.491	0.395	1.244
	MF_R_100	100.00%	0.359	0.395	0.910
MF_R	MF_R_0	0.00%	2.176	0.395	5.514
	MF_R_25	43.90%	0.864	0.395	2.190
	MF_R_50	57.58%	0.774	0.395	1.962
	MF_R_75	76.38%	0.701	0.395	1.776
	MF_R_100	100.00%	0.542	0.395	1.373

Table 5.4 (continue) Wall shear Stress Data

	Case	Y_*	τ_w (Pa)	τ_a (Pa)	τ_*
Q100_O	MF_R_0	0.00%	2.501	0.463	5.406
	MF_R_25	32.97%	1.410	0.463	3.048
	MF_R_50	50.14%	1.130	0.463	2.443
	MF_R_75	60.08%	0.981	0.463	2.121
	MF_R_100	100.00%	0.780	0.463	1.687
Q100_R	MF_R_0	0.00%	2.971	0.463	6.423
	MF_R_25	42.28%	0.673796	0.463	1.457
	MF_R_50	65.24%	0.588158	0.463	1.272
	MF_R_75	74.49%	0.321077	0.463	0.694
	MF_R_100	100.00%	0.360172	0.463	0.779

These data were plotted together in Figure 5.7 to develop the decay function. There are two basic requirements for this function. When the relative scour is 100%, the wall shear stress amplification should be equal to 1. When the relative scour is 0, the wall shear stress amplification was set as the average of value of cases with a flat bed, which is 5.056. Based on the literature review in Chapter 2 and the shape of the decay curve in Figure 5.4, the decay function was assumed to be an exponential function (Eq.5.3)

$$\frac{\tau}{\tau_a} = a * \exp \left(b * \frac{y_s}{y_{max}} \right) \quad (5.3)$$

And it should satisfy the following conditions:

$$\frac{\tau}{\tau_a} = a * \exp(b * 100\%) = 1$$

$$\frac{\tau}{\tau_a} = a * \exp(b * 0\%) = a = 5.056$$

Therefore, the decay function of wall shear stress is

$$\frac{\tau_w}{\tau_a} = 5.056 * \exp\left(-1.621 * \frac{y_s}{y_{max}}\right) \quad (5.4)$$

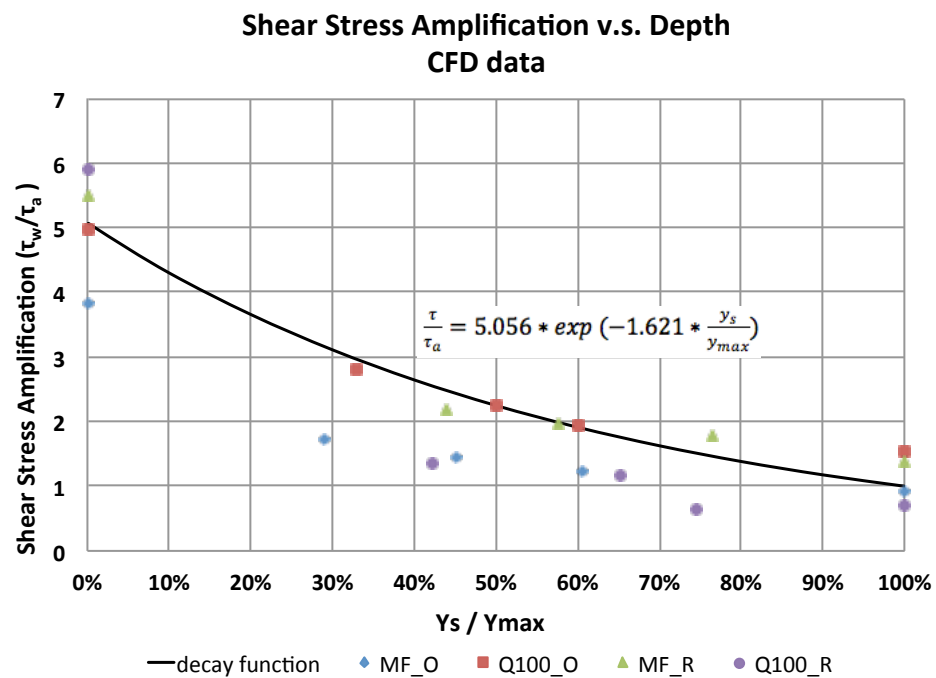


Figure 5.7 Decay function of wall shear stress

5.3 Calibration of the Decay Function

Even though the physical experimental method has a weak capacity to directly measure hydraulic loading indicators, a series of physical experiments was designed to indirectly calculate these indicators by Annandale to study the relation between hydraulic loading and scour. These physical experiments include cases with different regular-shape piers under different kinds of flow conditions. The bathymetries of these cases were non-cohesive clean sand with different d_{50} values. In this dissertation, these data are called Annandale data. In order to use these data to calibrate the developed decay function, the relative scour depth and wall shear stress amplification of each case of Annandale data needs to be calculated first and then plotted with the CFD data together.

5.3.1 Approach to Calculate Potential maximum Scour Depth

The Annandale data include the wall shear stress, inlet velocity, Darcy friction factor which can be converted into Manning n, flow depth and scour depth. However, the potential maximum flow depth of each case must be calculated with the following equation (Eq.2.5),

$$\frac{y_{max}}{y} = 2K_1K_2K_3\left(\frac{a}{y}\right)^{0.65}Fr^{0.43}$$

where y_{max} is the maximum scour depth, y is the approach flow depth, a is the width of the bridge and Fr is the Froude number. K_1 is the correction factor of pier nose shape.

Table 5.5 shows the values of K_1 of some kinds of common pier nodes, which are shown in Figure 5.8.

Table 5.5 K_1 values of some common pier nodes

Shape of Pier Nose	K_1
(a)	1.1
(b)	1
(c)	1
(d)	1
(e)	0.9

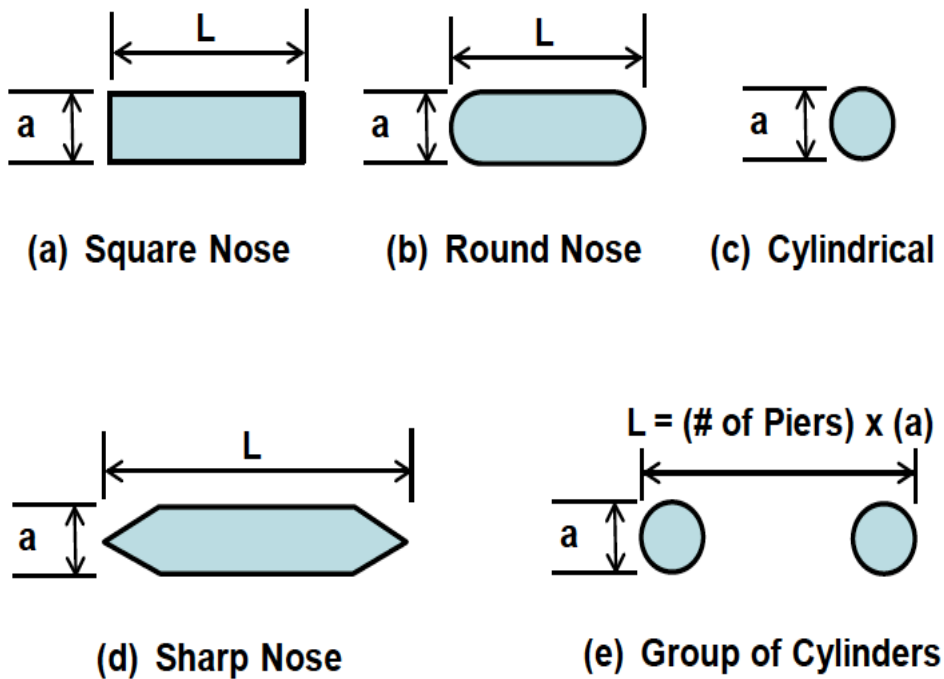


Figure 5.8 Common shapes of pier noses

K_2 is the correction factor of water flow with an attack angle (θ), which is also called as the hydraulic skew angle of water flow. The value of K_2 is calculated with Eq.5.5.

$$K_2 = (\cos \theta + \frac{L}{a} \sin \theta)^{0.65} \quad (5.5)$$

L is the length of the pier and a is the width of the pier node, which is shown in Figure 5.8. K_3 is the correction factor for the bed condition. Since the plane bed (flat bed) is the most common condition of the bridge sites for the flood frequencies employed in the scour design, the value of K_3 is obtained for the case of a plane bed. The value of K_3 is shown in Table 5.6. Since the bed condition of all cases in the table of the Annandale data is clear sand in a uniform water flow, the value of K_3 is 1.1.

Table 5.6 K_3 values

Bed Condition	Dune Height, H, (ft)	K_3
Clear-Water Scour	N/A	1.1
Plane Bed and Anti-Dune Flow	N/A	1.1
Small Dunes	$2 < H < 10$	1.1
Middle Dunes	$10 \leq H < 30$	1.2~1.1
Large Dunes	$H \geq 30$	1.3

Based on the equations and values above, the potential maximum scour depth of each case was calculated. The relative scour depth was calculated with the surveyed scour depth and the calculated maximum scour depth. The wall shear stress amplification τ_* of each case was calculated using the relevant physical quantities.

5.3.2 Envelope Decay Function

The wall shear stress amplification and relative scour depth of the Annandale data and CFD simulation results were plotted together in Figure 5.9. The Annandale data also clearly reflect a decay trend of wall shear stress with scour depth. When the scour depth is approximately the maximum depth, the shear stress amplification is approximately 1. Moreover, the CFD data are located in the range of the Annandale data, which is another evidence that these CFD models accurately simulate the water flows of the physical experiments.

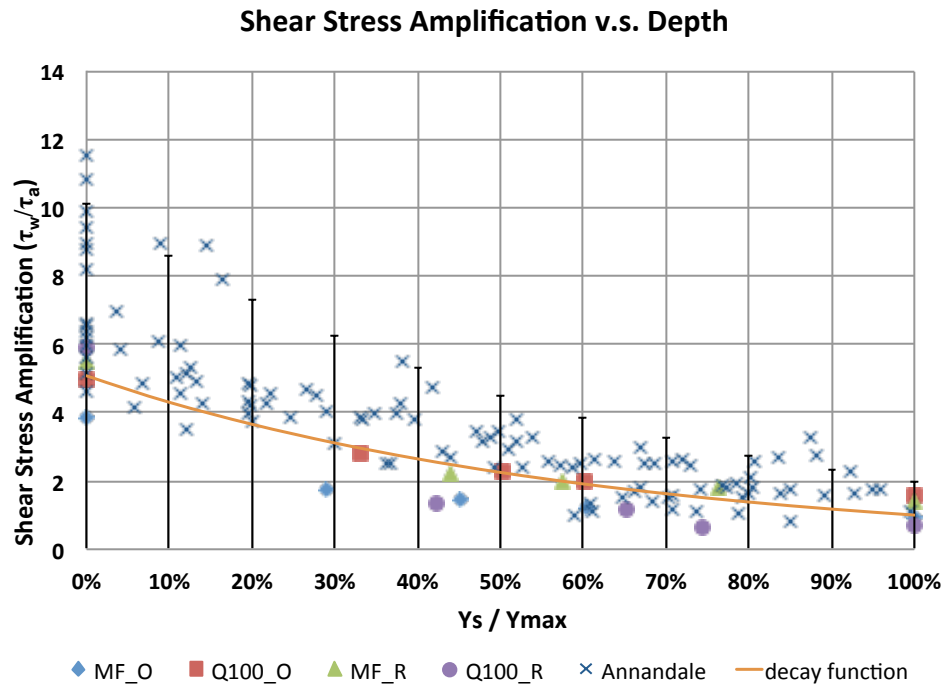


Figure 5.9 Shear stress amplification v.s. relative depth

On the other hand, the developed decay function does not have a good capacity to represent the decay trend of wall shear stress of both CFD data and Annandale data. While, the maximum difference between the data points and the decay function is about 100%. Therefore, an envelope decay function is a more appropriate option, which should cover most points in Figure 5.9. A safety factor 2 was imported into the decay function to develop the envelope function (Eq.5.6)

$$\frac{\tau_w}{\tau_a} = 10.112 * \exp\left(-1.621 * \frac{y_s}{y_{max}}\right) \quad (5.6)$$

Some conclusions can be obtained from Figure 5.10, which includes the envelope decay function, the decay function, CFD data and the Annandale data. First, this envelope decay function of wall shear stress covers almost all points (about 95%) of the Annandale data and CFD data. Second, when the relative scour depth is smaller than 40%, the envelope function has a relative large gap from CFD and most Annandale data. And when the relative scour depth is larger than 40%, the envelope decay function is close to CFD and Annandale data.

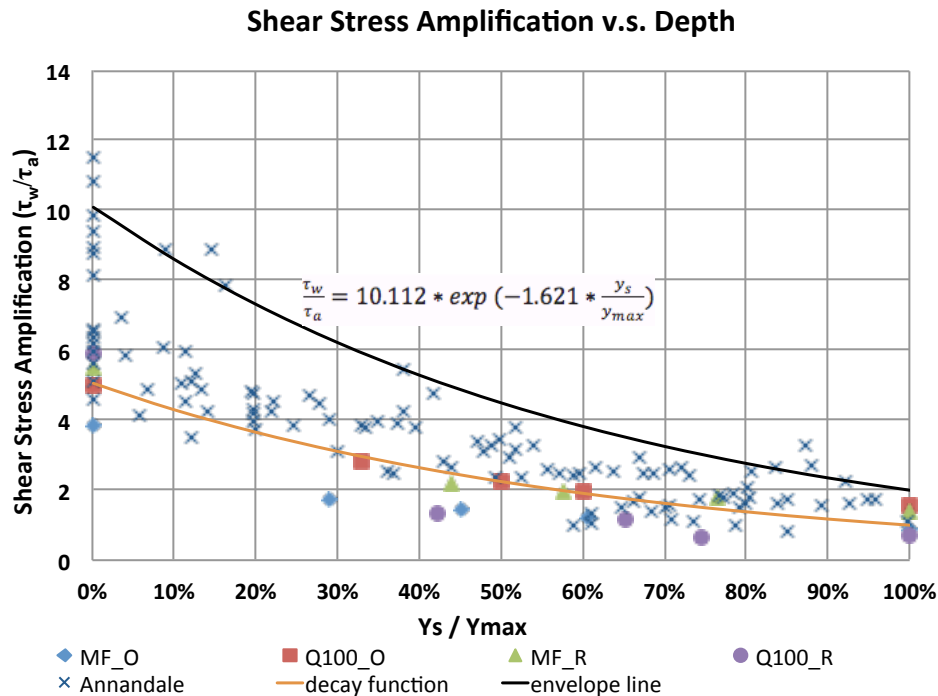


Figure 5.10 Decay function of wall shear stress of Annandale data and CFD data

5.4 Validation of the Decay Function

In Chapter 3, CFD models of water flows around the rectangular pier with a 30° attack angle were conducted to verify the physical models of these CFD models. The wall

shear stress values around this pier were used to verify the envelope decay function, and the relative scour depths of these cases were calculated with the bathymetry elevation values of these CFD models. These data were also plotted together with the Annandale data and the CFD data in Figure 5.11.

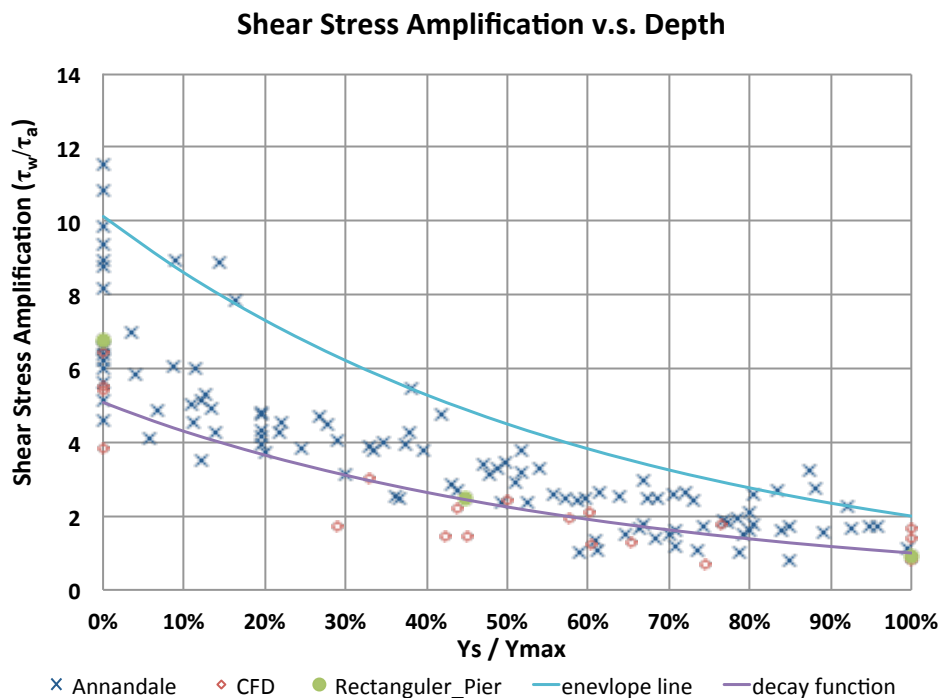


Figure 5.11 CFD data of rectangular pier with Annandale data and CFD data

As shown in Figure 5.11, the data of CFD modeling for the rectangular pier were enclosed by the envelope decay function and these data are also close to the decay function. This means the envelope decay function of wall shear stress adequately describes the relation between wall shear stress amplification and relative scour depth.

5.5 Summary

In this chapter, a decay function of wall shear stress was developed with the CFD modeling results for the physical experiments. In order to calibrate this decay function and more accurately describe the decay trend, the Annandale data were used to modify the decay function and develop an envelope function. Since the envelope function covers most of the CFD data and Annandale data, it was applied to describe the relation between wall shear stress amplification and relative scour depth. The envelope function and decay function were verified with the CFD modeling results of water flows around a rectangular pier with a 30° attack angle. In the next chapter, CFD models of the full-scale Feather River Bridge simulate water flows around the original pier and retrofitted design. These were developed to calculate wall shear stress distributions. And the developed envelope function and decay function were also applied to study the pier scour problem.

CHAPTER 6 Preliminary CFD Study of Pier Scour of the Feather River Bridge

6.1 Overview

In this research, the preliminary CFD study of pier scour of the Feather River Bridge is discussed. In order to apply the envelope decay function of wall shear stress to study the pier scour problems in the real world, there are two main questions that remain to be answered. First, full-scale CFD models need to be developed to verify the decay trend and decay function of wall shear stress. Second, the applications of the decay function need to be developed.

In this chapter, CFD models of the full-scale Feather River Bridge is developed to obtain wall shear stress distributions on the bathymetries, which were surveyed before and after the flood event. The flow conditions of the normal state (MF) and the flood event (Q100) were given by the Feather River Emergency Scour Study. The CFD simulation results are presented in this chapter to analyze the relation between wall shear stress and scour depth around Pier 22 of the Feather River Bridge and verify the decay function. The application of the decay function in the real world was developed by taking the Feather River scour study as an example.

6.2 Development of CFD Models

The development of CFD models of the full-scale Feather River Bridge also follows the procedure in Figure 4.1. The physical models in these CFD simulations are the same as those of CFD models of the physical experiments. Even though there are two piers (the original and retrofitted pier), two kinds of flow conditions (MF and Q100) and two bathymetries (surveyed before and after the flood event), only four cases were

simulated in this research. These CFD cases are shown in Table 6.1, in which B2007 is the bathymetry surveyed before the flood event and B2011 is the one surveyed after the flood event. These four cases were separated into two groups. Cases in Group A have already occurred in the real world. They are used to verify the decay trend of wall shear stress and find out the applications of the decay function. The case in Group B is used to study the influence of the retrofitted design.

Table 6.1 CFD models of full-scale Feather River Bridge

Group	Case	Bathymetry	Pier	Flow Condition
A	O_B2007_MF	B2007	Original	MF
	O_B2007_Q100	B2007	Original	Q100
	O_B2011_MF	B2011	Original	MF
B	R_B2007_MF	B2007	Retrofitted	MF

6.2.1 Geometry

Similar to the CFD models of the physical experiments in Chapter 4, the original CAD models of these four cases were created with data of the surveyed bathymetries and the CAD models of the original and retrofitted piers in SOLIDWORKS. Walls around the surveyed bathymetry and a top wall cover the flow domain were added to form a closure volume to satisfy the requirements of CFD method. Before importing these original CAD models into STAR-CCM+, some adjustments are strongly recommended to avoid potential problems caused by the geometry. Figure 6.1 is an example of the original CAD

model (B2011). The shape of this bathymetry was directly created with the surveyed data in SOLIDWORKS.

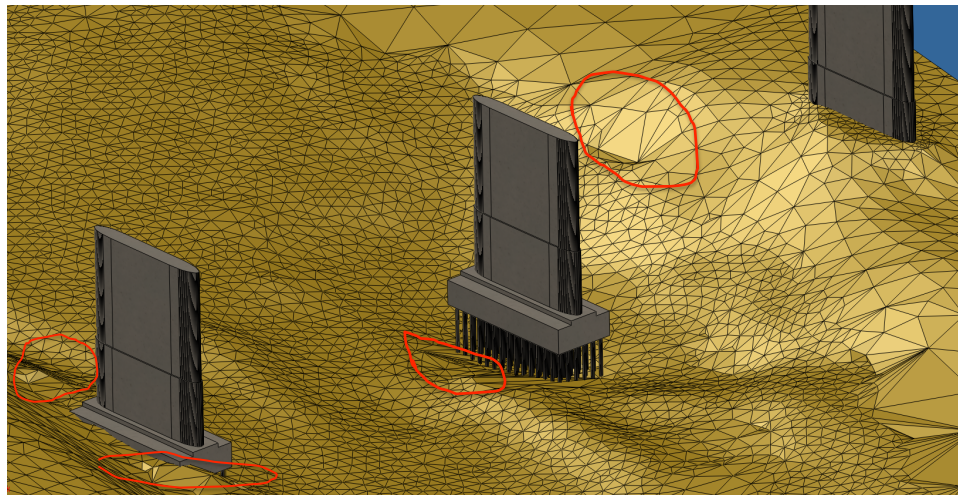


Figure 6.1 Original CAD model of B2011

This original CAD model exhibits the shapes of pier scour and the abutments of the Feather River Bridge. In order to reduce the time required to survey the bathymetry, the surveyor collected a large data point density around Pier 22 and a relative small one in other areas. The result of this action is intuitively reflected by the sizes of the triangles. This also results in some sharp curves in the shape of the bathymetry, some of which are identified by red circles. They may have a series negative influence on the convergence of the CFD model or even lead to a CFD model crash. Therefore, these sharp curves need to be eliminated to create the final CFD geometry. However the shape of the bathymetry must be maintained. Figure 6.2 is the final CFD geometry of B2011. The shapes of the bathymetry in the red circles are much smoother than those of the original CAD model,

which is the result of eliminating the sharp curves. Compared to the original CAD model, the final CFD geometry includes almost all details of pier scour and abutment scour.

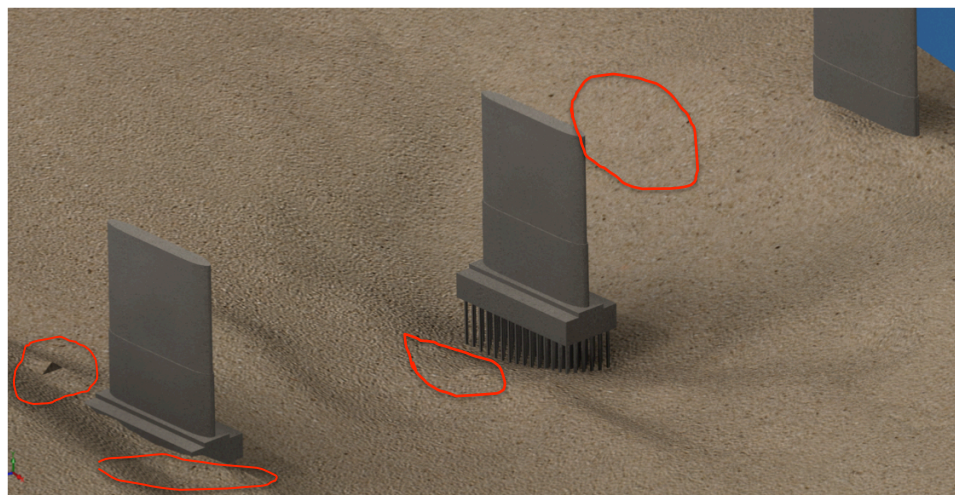


Figure 6.2 Final CFD geometry of B2011

B2011 was assumed as the scour bathymetry and B2007 was used as the bathymetry without scour. Figure 6.3 demonstrates the differences between elevations of these two bathymetries. At A and B, there are two obvious scour holes after the flood event. The reason of scour at B is a kind of abutment scour. Scour at A is pier scour, which is the focus of this research.

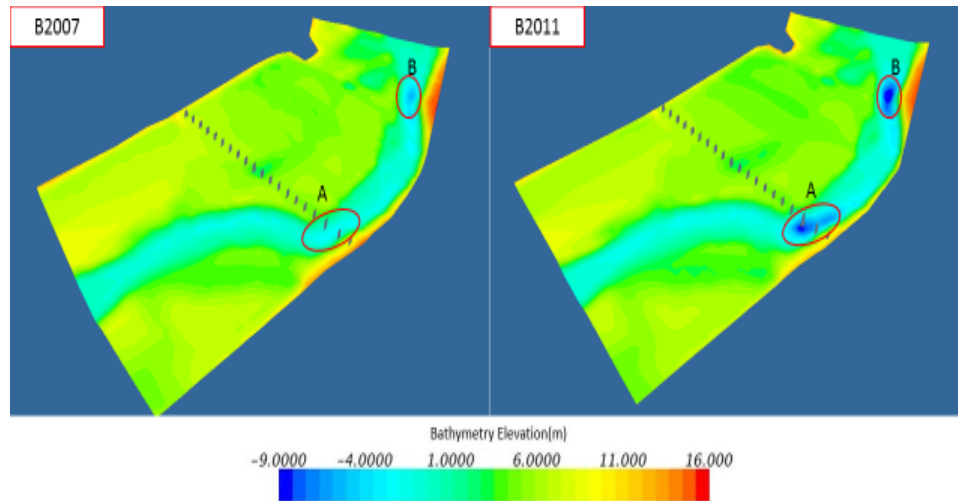


Figure 6.3 Bathymetries of B2007 and B2011

Figure 6.4 is an example of the final CFD geometry with the name of each surface (top surface is hidden). Table 6.2 shows the boundary type of each face specified in the CFD model. In this research, the earthen material was assumed as clean, non-cohesive and coarse sand ($d_{50}=2\text{mm}$) to simplify the research. The roughness height of the bathymetry of CFD geometry was empirically set as 4 mm.

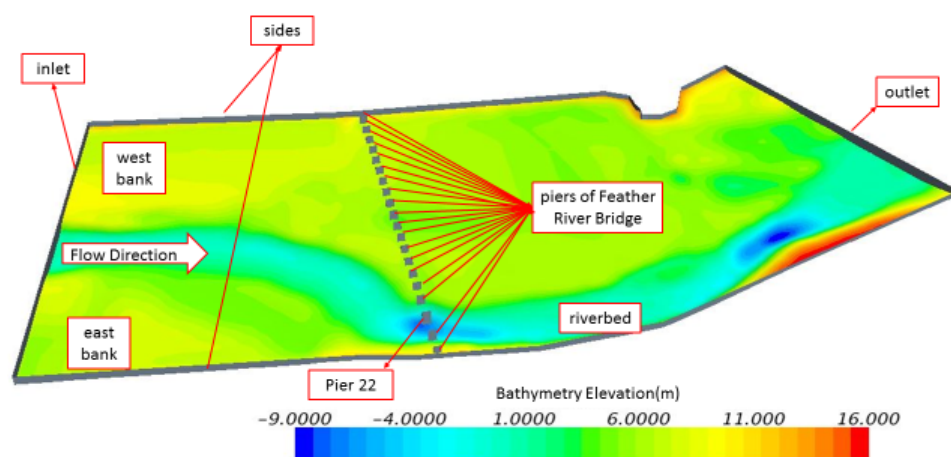


Figure 6.4 Final geometry of O_B2011_MF

Table 6.2 Boundary conditions

Boundary Name	Part of original CAD model	Type	Note
inlet	inlet	Velocity Inlet/ Mass Flow Inlet	-
outlet	outlet	Pressure Outlet	-
Top	Top	Symmetry Plane	-
sides	sides	Wall	Non-slip; Smooth
pier	piers of Feather River Bridge	Wall	Non-slip Smooth
	Pier 22	Wall	
bed	riverbed	Wall	Non-slip Rough Roughness Height = 4mm
	west bank		
	east bank		

6.2.2 Mesh

The challenges described in Section 4.3 also exist in the full-scale Feather River CFD models, while the huge size of the model makes it even more challenging. The size of the geometry is about 1500 m X 100m X 5m. Therefore, in order to restrict the number of mesh cells, the geometry was separated into two areas: a core area and non-core area. The core area is defined by volumetric control to set a denser mesh, as shown in Figure

6.5. This area covers Pier 22 and the river channel from about 400 m upstream of Pier 22 to about 250 m downstream of Pier 22. The wall shear stress distribution, water flow and free surface in this area were needed to be accurately simulated by these CFD models. The other area was defined as a non-core area, where a coarse mesh was set.

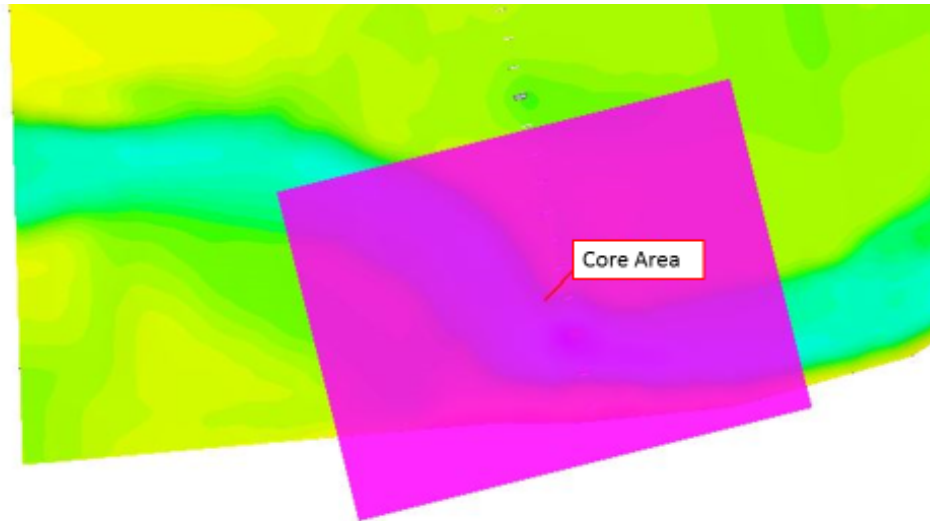


Figure 6.5 Core area of CFD model

Since the quality of the CAD models created in SOLIDWORKS is sufficient, “Surface Remesher” was activated to generate a surface mesh for these four cases. “Prism Layer Mesher” was selected to mesh the near-wall region. For Case O_B2011_MF, the H-piles are exposed in the water flow, which requires the volume mesh models to properly capture the solid material thickness. Therefore, “Thick Mesher” was used. For the other three cases, “Polyhedral Mesher” was utilized to mesh the irregular shape of the surveyed bathymetries. This model has the same function to set a prismatic layered volume mesh as “Thickness Mesher” and takes a relative short time to finish meshing for a similar number of mesh cells. Besides the volumetric control defined in the core area,

there are another two kinds of volumetric controls, as shown in Figure 6.6. A denser mesh was set in these cylinders to maintain the shapes of the leading and trailing edges. Block 2 defines a smaller volume in the core area, where an even denser mesh was set to more finely simulate the water flow. For Case MF_B2011_MF, another volumetric control (Block 3) was set to mesh the H-piles group.

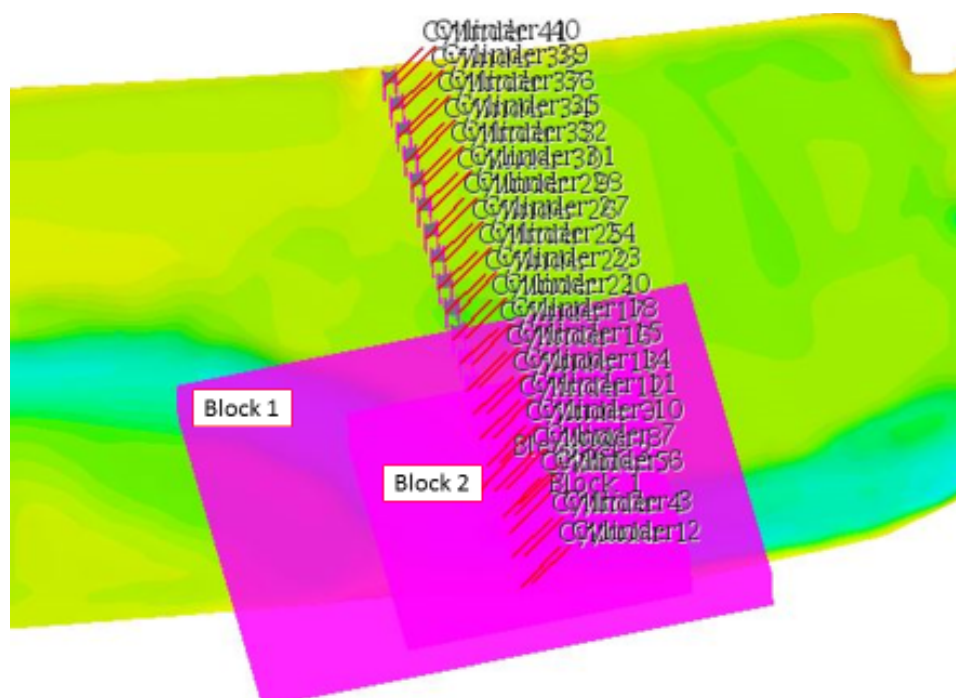


Figure 6.6 Volumetric Controls

The base size of the mesh is 10 m. For the cylinders and Block 3, the custom size is 1% of the base size and the custom sizes of Block 1 and Block 2 are 25% and 10% of the base size. The size of the refined cells are 0.1%~1% of the base size in the core area. Figure 6.7 shows the mesh of Case O_B2011_MF. Even though many actions were taken to restrict the number of mesh cells, the number of mesh cells was still about 10 million.

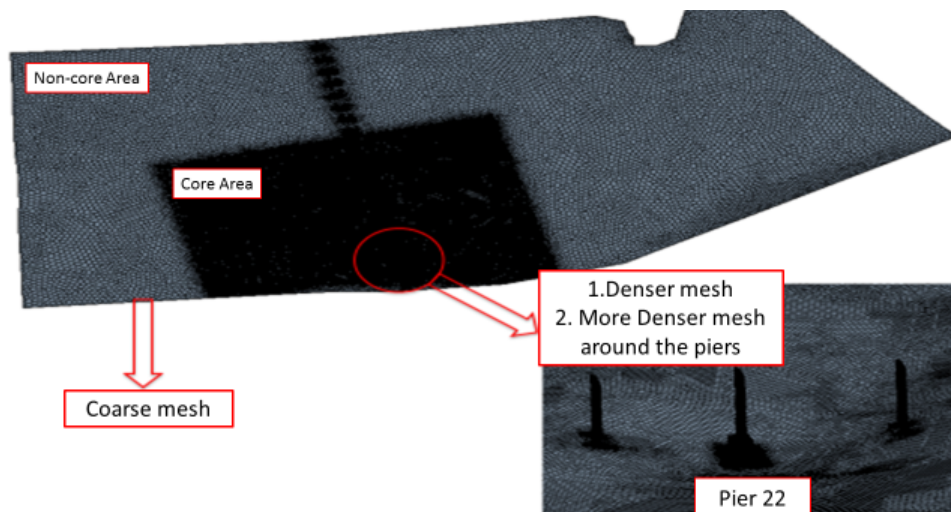


Figure 6.7 Mesh of Case O_B2011_MF

The roughness height of the bathymetry was set as 4 mm. Therefore, the height of the first cell on the surface edge is required to be larger than 4mm by the rough function in STAR-CCM+. The range of y^+ recommended by users to use “All y^+ Wall Treatment” is from 20 to 200. So the wall distances of MF and Q100 are estimated with Eq.4.2 (Table 6.3). However, the estimated wall distances and the requirements of the roughness function are conflictive.

Table 6.3 Estimation of wall distance

Flow Condition	Inlet Velocity (m/s)	Water Depth (m)	y^+	Re	H (mm)
MF	1.463	9.571	20~200	$1.57 * 10^7$	0.35~3.5
Q100	2.134	15.545	20~200	$3.7 * 10^7$	0.25~2.5

Since the requirement of the roughness function is more closely related to the accuracy of the CFD simulation results, y^+ of first cell on the bathymetry must be outside of its recommended range. The minimum y^+ values of these two kinds of flow conditions calculated with the roughness height is about 250 for MF and 350 for Q100, for which “High y^+ Wall Treatment” is more appropriate. STAR-CCM+ user guider points out that the “All y^+ Wall Treatment” is a hybrid method of “Low y^+ Wall Treatment” and “High y^+ Wall Treatment”. It is designed to give results similar to the low- y^+ treatment as $y^+ \rightarrow 0$ and to the high- y^+ treatment for $y^+ > 30$. Hence, “All y^+ Wall treatment” was still activated to maintain the consistency of physical models of all CFD models in this research. Moreover, the study of the wall function and y^+ conducted by CFD team of Leading Engineering Application Providers (LEAP) in Australia expresses that the simulation results by using the three current kinds of wall functions agree with each other very well in the overlapping range of y^+ , as shown in Figure 6.8. (<http://www.computationalfluidynamics.com.au/turbulence-part-3-selection-of-wall-functions-and-y-to-best-capture-the-turbulent-boundary-layer/>).

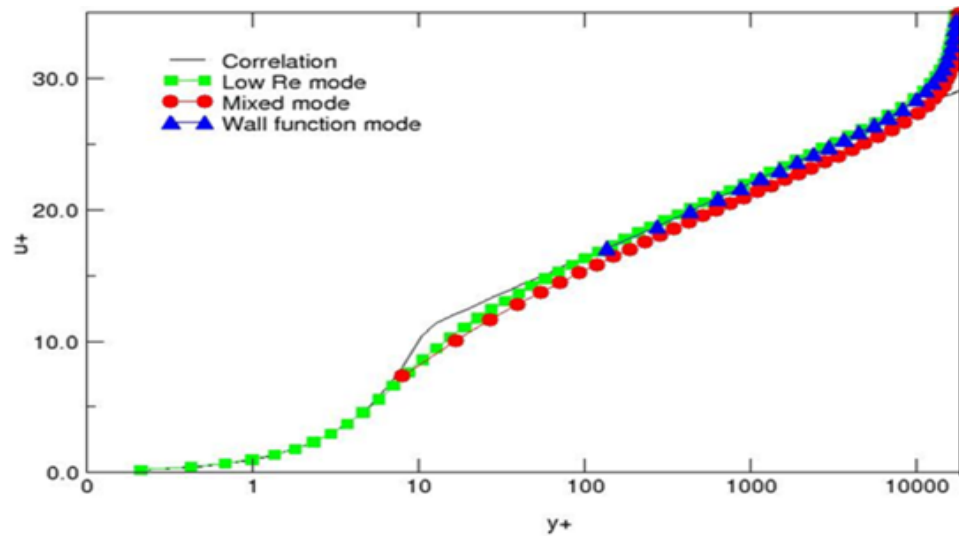


Figure 6.8 Comparison of different wall functions

6.2.3 Flow Conditions, Physical models and Necessary Setup

The flow conditions of the full-scale Feather River Bridge include water depth, flow rate and average velocity, as shown in Table 6.4. The water depth and flow rate are two physical quantities which can be directly measured in the field. The average velocities of these two kinds of flow conditions were calculated with the 2-D hydraulic modeling conducted by Flora. Even though the value of flow rate for each flow condition was directly surveyed and was considered to be closer to the real state, the calculated average velocity of the 2-D simulations conducted by Flora also describes the water flow. Therefore, the flow rate and the average velocity are considered to be equivalent. And the average velocity was used as the initial conditions for the physical models of these CFD models. The boundary type of the inlet surface can be set as “Velocity Inlet” or “Mass Flow Rate” to optimize each case. Figure 6.9 shows the initial free surfaces of MF and Q100.

Table 6.4 Flow conditions

Flow Condition	State	Flow Rate (m^3/s)	Flow Rate (Kg/s)	Flow Depth (m)	Average Velocity (m/s)
MF	Normal state	1260.1	$1.257 * 10^6$	6.98	1.463
Q100	Flood event	4454.3	$4.443 * 10^6$	15.545	2.134

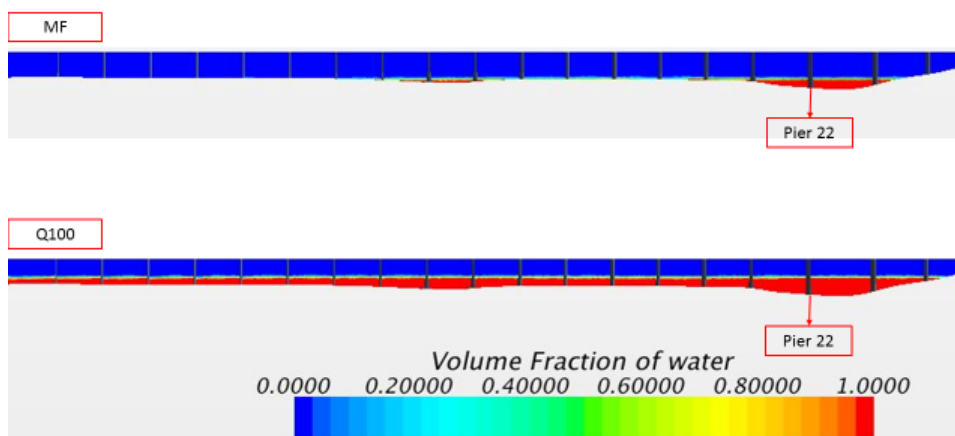


Figure 6.9 Initial free surface

The method used to calibrate the wall shear stress described in Section 4.5 was also used in these four CFD models. User defined functions were created to define the initial regions and initial flow velocity of air and water (Table 6.5). The average_velocity is the value of the physical quantities of flow conditions. But the water_depth is the water depth from water surface to the foundation of the original pier. The physical models of

these CFD models are exactly the same as the ones used in the CFD models of the physical experiments, which are shown in Figure 4.10.

Table 6.5 User defined function of CFD models of full-scale Feather River Bridge

Name	Function	Definition
water	Define water domain	\$\$Position[1] <=water_depth? 1 : 0
air	Define air domain	1-\$water
v	Define velocity	[\$\$Position[1]< water_depth? average_velocity:0,0,0]

6.3 CFD Simulation Results

As discussed in Chapter 4, only when the unsteady CFD simulation becomes quasi-steady, can the wall shear stress distributions around Pier 22 be used taken as the simulation result to analyze its relation with scour.

6.3.1 Physical Time

In order to ensure that unsteady CFD simulation results are close to the real situation, a relative long physical time is necessary for them to be quasi-steady. However, a long physical time also significantly increases the computational time, especially for these four cases. Therefore, an appropriate physical time is necessary not only to ensure that the CFD simulation is quasi-steady, but also restrict the computational time. Currently, the physical time was set to 600 seconds. As shown in Figure 6.10, the wall

shear stress distributions around Pier 22 of O_B2007_MF at different moments agree with each other very well, which means 600s physical time is long enough for the unsteady CFD simulation to be quasi-steady

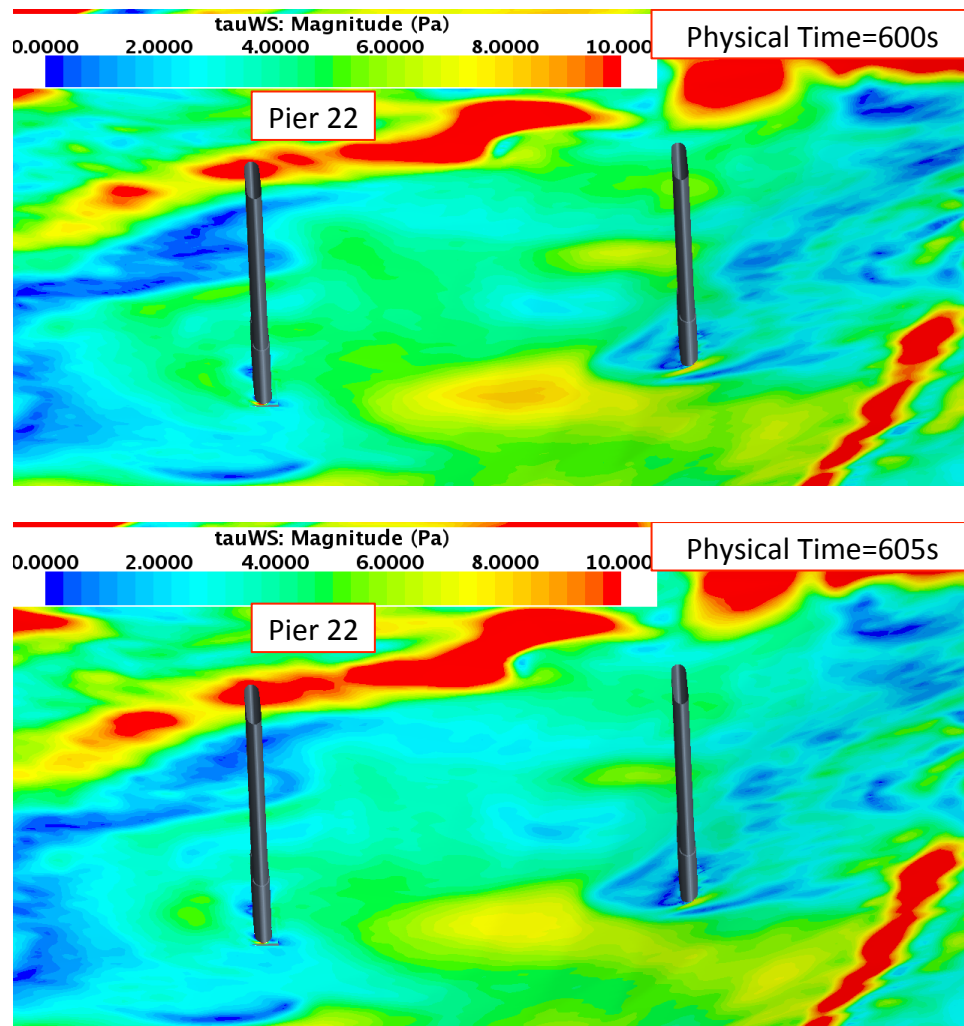


Figure 6.10 Wall shear stress distributions around Pier 22 at different moments

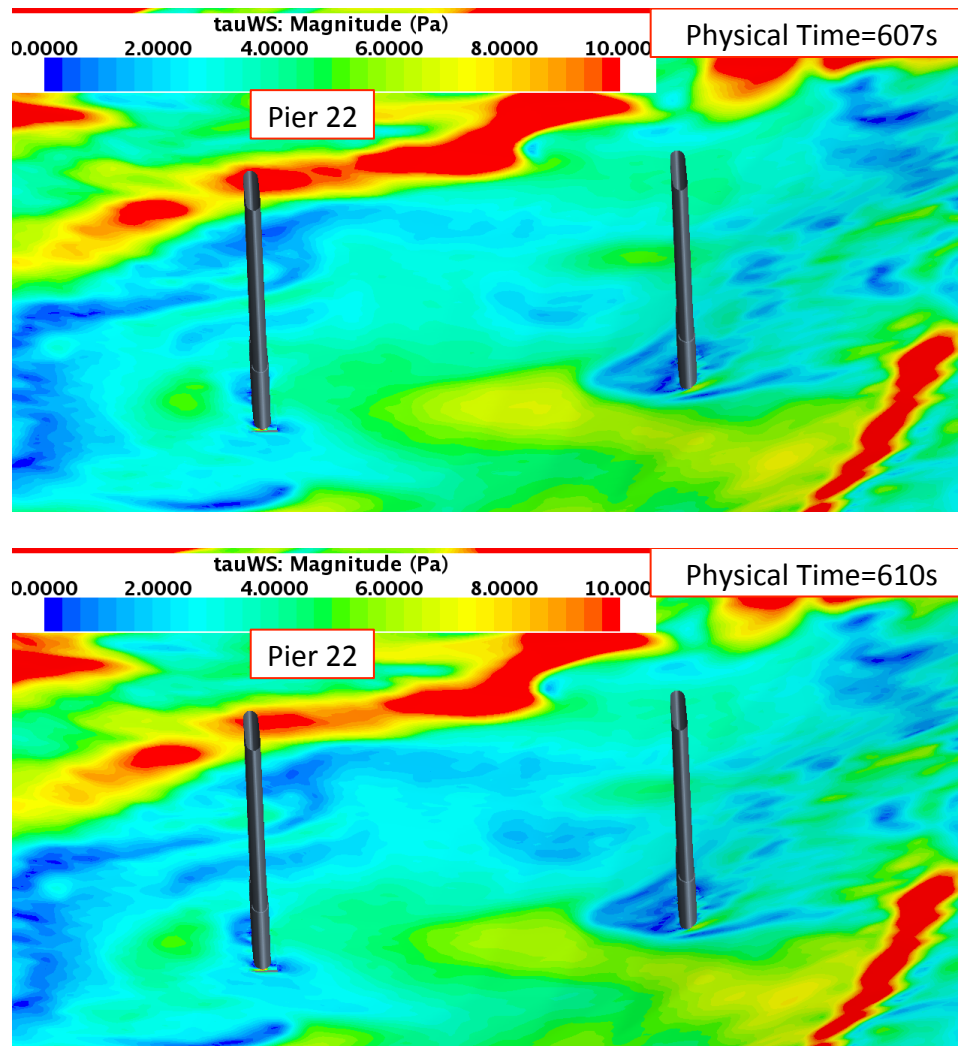


Figure 6.10 (continue) Wall shear stress distributions around Pier 22 at different moments

6.3.2 Wall Shear Stress Distributions

Figure 6.11 is the wall shear stress distribution of Case O_B2007_MF. Location A shows the high wall shear stress around Pier 22, which initiates pier scour. The form drag caused by the shape of the bathymetry increases the wall shear stress in some areas, like location C. The reason for the high wall shear stress in locations B and D is that the width of Feather River becomes narrow there. It is also a reason that leads to high wall

shear stress at location E. The other reason is the interaction between the hydraulic structures and the water flow. The water flow direction changes downstream of the bridge. So interactions between the water flow and the bank in location F are intense and the wall shear stress there is obviously larger. The high wall shear stress in location G is mainly due to the coarse mesh. Since the mesh in location G is not fine enough, the VOF model has a negative influence on the wall function, which makes CFD simulations of wall shear stress unreliable in that location. Since area G is distant from Pier 22, its potential negative influence on the shear stress distribution around Pier 22 is negligible.

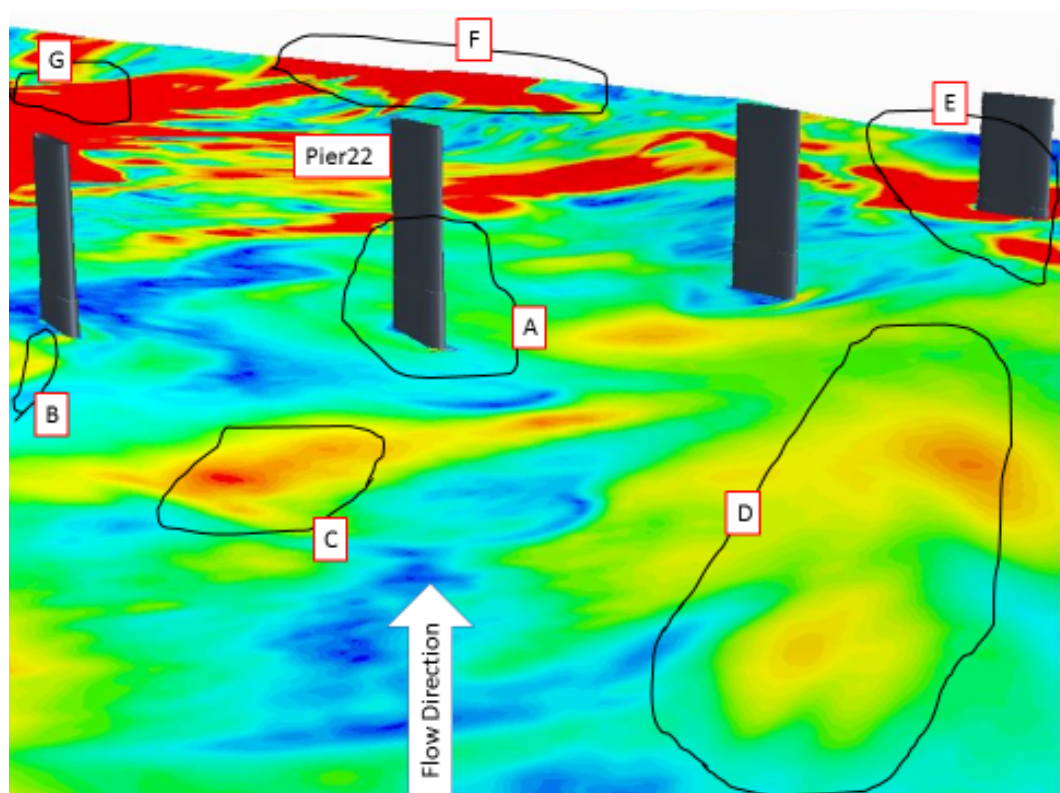


Figure 6.11 Wall shear stress distribution of Case O_B2007_MF

Figure 6.12 shows a comparison between wall shear stress distributions around Pier 22 using B2007 and B2011 under normal flow conditions. Before the flood event, the wall shear stress is large around the pier and leads to pier scour. During the flood event, the wall shear stress on the entire bathymetry rapidly increases, as shown in Figure 6.13. Therefore, the flood event speeds up the process of pier scour and produces the bathymetry surveyed in 2011. After the flood event, even though wall shear stress in some small areas become larger, the wall shear stress distribution around Pier 22 still shows a clear decay trend. Changes in the bathymetry increase the wall shear stress in some areas.

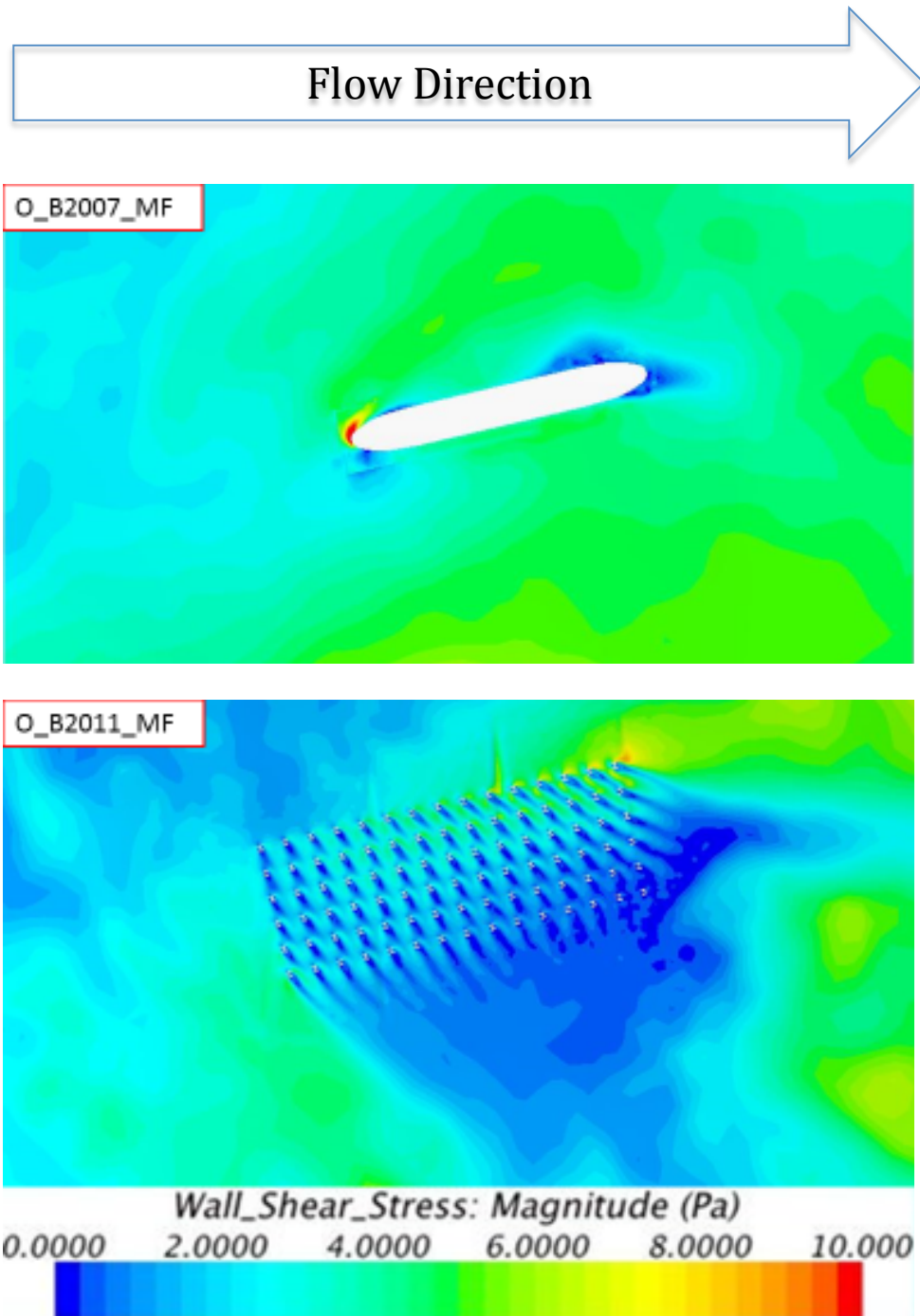


Figure 6.12 Wall shear stress distributions of O_B2007_MF and O_B2011_MF

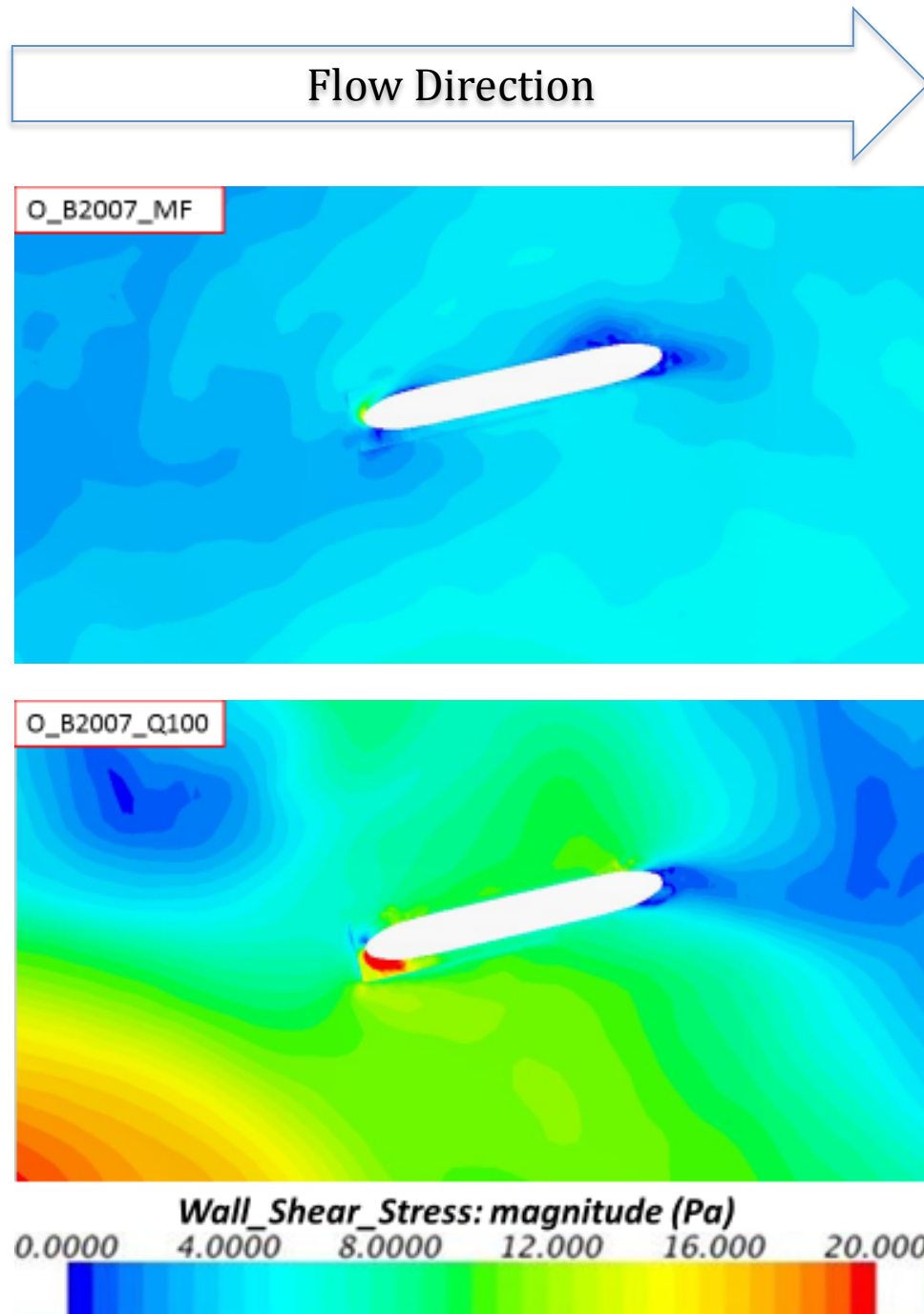


Figure 6.13 Wall shear stress distributions of O_B2007_MF and O_B2007_Q100

In chapter 4, the simulation results reveal that the retrofitted design actually enhances the erosion capacity of water flow. The simulation results of the full-scale Feather River Bridge also demonstrate this. Figure 6.14 is a comparison between wall shear stress distributions around Pier 22 of O_B2007_MF and R_B2007_MF. The influence of the shape of the bathymetry and flow conditions have already been eliminated by using the same conditions for both cases. Therefore, the main source of the differences between the wall shear stress distributions is the pier shape. The area with high wall shear stress is obvious larger around the retrofitted pier and the maximum shear stresses are also much larger.

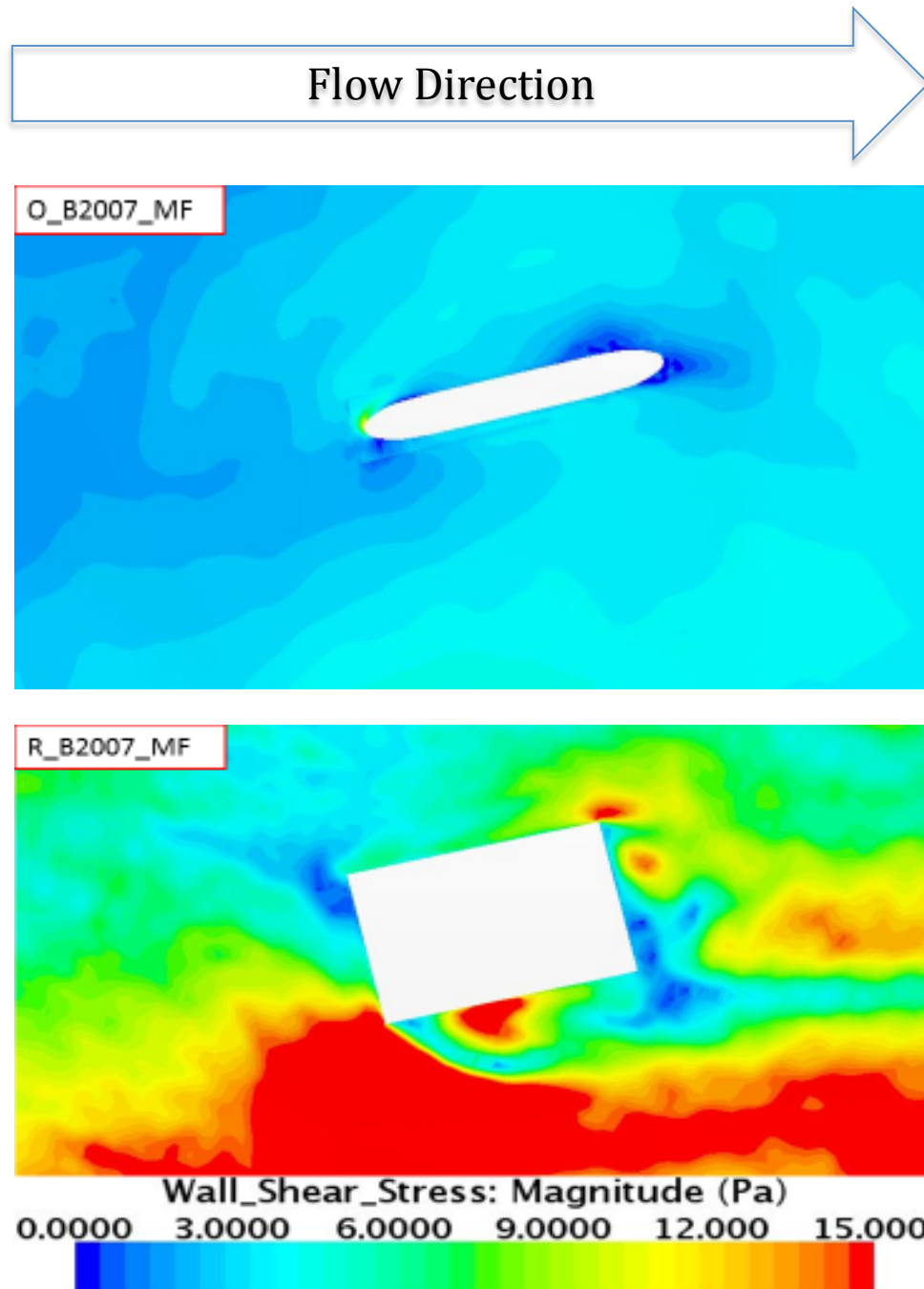


Figure 6.14 Wall shear stress distribution of O_B2007_MF and R_B2007_MF

6.4 Application of Decay Function of Wall Shear Stress

Application of the envelope decay function requires two tasks. First, the decay function of the wall shear stress (both of the decay function and enveloped function) needs to be verified with the simulation results of the CFD models of the full-scale Feather River Bridge. Second, an approach needs to be developed to apply the decay function to resolve engineering problems about pier scour.

6.4.1 Validation of Decay Function

As shown in Figure 6.3, the bathymetry around Pier 22 surveyed before the flood event (B2007) is almost flat, so it was considered as the one without any scour hole. This means the relative scour depth of B2007 is 0%. Two follow-up surveys after the flood event confirmed the scour depth. Therefore, the bathymetry surveyed after the flood event (B2011) was considered to be the scoured bathymetry. Thus, the relative scour depth of this bathymetry was considered to be close to 100%. This means the local wall shear stress is close to the approach wall shear stress. The simulation results of Case O_B2007_MF and Case O_B2011_MF represent the change of wall shear stress with scour in the real world.

The approach to used wall shear stress data is the same as the one described in Chapter 5. For the cases with B2007, the maximum wall shear stress around Pier 22 was used for future analysis. The locations of these points also need to be close to each other. And for the case with B2011, the wall shear stress value of the point with the maximum scour depth around Pier 22 was used.

Table 6.6 Wall shear stress data

Case	Wall Shear Stress (Pa)	Scour Depth (m)
O_B2007_MF	21.103	0
O_B2007_Q100	39.396	0
O_B2011_MF	2.723	7.695

The method of calculating the approach wall shear stress values for MF and Q100 are as followed. Since the width of the river is much larger than the water depth and the convenient approach to accurately calculate the hydraulic radius of river is not fully developed, the hydraulic radius is replaced with the water depth. Even though the average velocity of each flow condition in this research was calculated by previous 2-D hydraulic simulations and the flow rate was directly surveyed, they are considered to be equivalent and the average velocity was used. Moreover, there are many convenient and accurate approaches to survey average velocity, like the Acoustic Doppler Current Profiler (ADCP) method (Yao, 2002).

The approach to determine the Manning n of sand ($d_{50} = 4\text{mm}$) is complex. Since the value of Manning n mainly relates with the surface roughness, the amount of vegetation and channel irregularity (Chaudhry, 2007), this value of given sand can be treated as a constant. Annandale data gives Darcy friction factors of different kinds of

sand with different hydraulic radiuses. The values of Manning n for the sand were calculated with Eq.6.1 (Yen, B. C. 1992).

$$n = 0.0926f^{0.5}R_h^{0.17} \quad (6.1)$$

The calculated data of Annandale data is shown in Table 6.7. With these data, the linear interpolation method was applied to estimate the Manning n of the sand ($d_{50} = 4$ mm).

Table 6.7 Manning n of sand

	d_{50} (mm)	Manning n
Annandale Data	1.2	0.0134
	2.4	0.0139
	5.0	0.0155
Estimated data	4.0	0.0147

Therefore, the values of approach wall shear stress of these two kinds of flow condition were calculated with Eq.5.2 and are shown in Table 6.8.

Table 6.8 Approach wall shear stress

Flow Condition	Water Depth (m)	Average Velocity (m/s)	Manning n ($d_{50} = 4$ mm)	τ_a (Pa)
MF	9.571	1.463	0.0147	2.137
Q100	15.545	2.134	0.0147	3.868

The wall shear stress amplification and relative scour depth of cases in Group A are shown in Table 6.9. These data was plotted together with the decay function and the envelope decay function in Figure 6.15. There are three conclusions. First, since these three data are covered by or very close to the envelope decay function, the enveloped decay function does a good job of representing the relation between wall shear stress and scour depth. Second, the cases with non-scoured bathymetry are not accurately predicted with the decay function. Finally, the value of the wall shear stress amplification of O_B2011_MF is close to 1. Therefore, it is very possible that the process of scour around Pier 22 stops there, which also confirms the assumption of this bathymetry.

Table 6.9 Wall shear stress amplification and relative scour depth

Case	Wall Shear Stress Amplification	Estimated Relative Scour Depth
O_B2007_MF	9.875	0
O_B2007_Q100	10.185	0
O_B2011_MF	1.274	About 100%

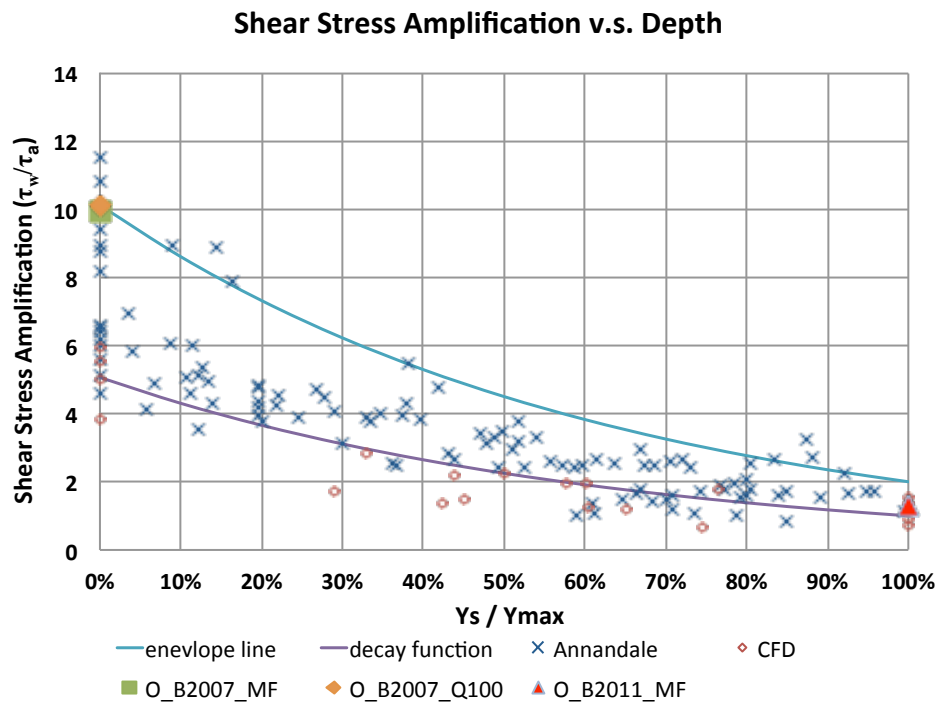


Figure 6.15 Validation of decay function

6.4.2 Applications of the Decay Function

There are two possible applications of the decay functions given information of soil constituting of each layer near the given pier. First, the necessary depth of the foundation can be estimated when designing a new bridge. Second, the local wall shear stress estimated with the decay function can be used to compare with the critical shear stress of the earthen material to determine whether actions are necessary to fix the pier scour problem. In fact, these two kinds of potential application share the same approach to apply the decay function. The pier scour study of Feather River Bridge was taken as an example to show these two applications.

The information about what soils constitute each layer near Pier 22 was given by the report of Feather River Emergency Scour Study. The value of critical shear stress of earthen material in each layer was calculated with Guo's equations (Eq.2.1 and Eq.2.2).

Table 6.10 Erodibility of the soil at Pier 22

Elevation (ft)	Depth, y_s (m)	d_{50} (mm)	Critical Shear Stress (Pa)
12.92	6.730	2	1.529
-0.68	10.875	2	1.529
-2.68	11.485	12	11.239
-5.98	12.491	12	11.239
-10.98	14.015	0.25	0.182
-15.68	15.447	0.2	0.166
-18.68	16.362	100	92.838
-21.48	17.215	150	139.190
-21.68	17.276	150	139.190
-40.98	23.159	178	165.147
-45.68	24.591	-	0.000

Note: (1) Elevation of the foundation of the original pier is 35ft;

(2) column 2=|column 1 -35|*0.3048(m).

Based on the calculated critical shear stress of the soil and the CFD simulations of the wall shear stress, the critical shear stress at the elevation of -18.68ft is obviously

larger than the local shear stress. Therefore, it is very possible that the pier scour stops in this layer. The scour depth at this elevation was used as the maximum scour depth (y_{\max}). So the relative scour depth of each layer can be calculated with $\frac{y_s}{y_{\max}}$. The approach wall shear stress of MF and Q100 are shown in Table 6.8. With the envelope decay function of wall shear stress (Eq.5.6), local shear stress value around Pier 22 of different flow conditions were calculated and shown in Table 6.11.

Table 6.11 Estimated local wall shear stress with the envelope function

Elevation (ft)	Depth, y_s (m)	Relative Scour Depth	Local Wall Shear Stress of MF (Pa)	Local Wall Shear Stress of Q100 (Pa)
12.92	6.730	41.13%	12.742	20.751
-0.68	10.875	66.47%	8.323	13.555
-2.68	11.485	70.19%	7.818	12.732
-5.98	12.491	76.34%	7.051	11.482
-10.98	14.015	85.66%	6.029	9.818
-15.68	15.447	94.41%	5.204	8.474
-18.68	16.362 (y_{\max})	100.00%	4.737	7.715

As shown in Figure 6.16, the decay curve of the local wall shear stress of MF has three intersections with the curve of the critical shear stress (A, B and C). Point A and B

mean that the scour depth around Pier 22 under MF can reach the elevation of -0.68 ft. However, the thickness of this layer is only 2 feet, which may be not enough for water flow to be uniform and steady. Moreover, the estimated local wall shear stress value is not much smaller than the critical shear stress ($\frac{\tau_w}{\tau_c} \approx 67\%$). Hence, the soil of this layer was considered to be removed, but the speed of scour is slow. Point C clearly shows that the pier scour stops at the elevation of -18.68 ft. For Q100, the estimated local wall shear stress becomes close to the critical shear stress at elevation of -6 ft (Point E). With appropriate actions to enlarge the critical shear stress of soil in this layer, the pier scour can be stopped here. Moreover, since the estimated wall shear stress and critical shear stress are very close to each other at Point E, an economic design to fix the scour problem is feasible. Point D shows that pier scour also stops at the elevation of -18.68 ft. The Feather River Emergency Scour Study Report gives similar conclusions with a much more complex method, as shown in Figure 6.17.

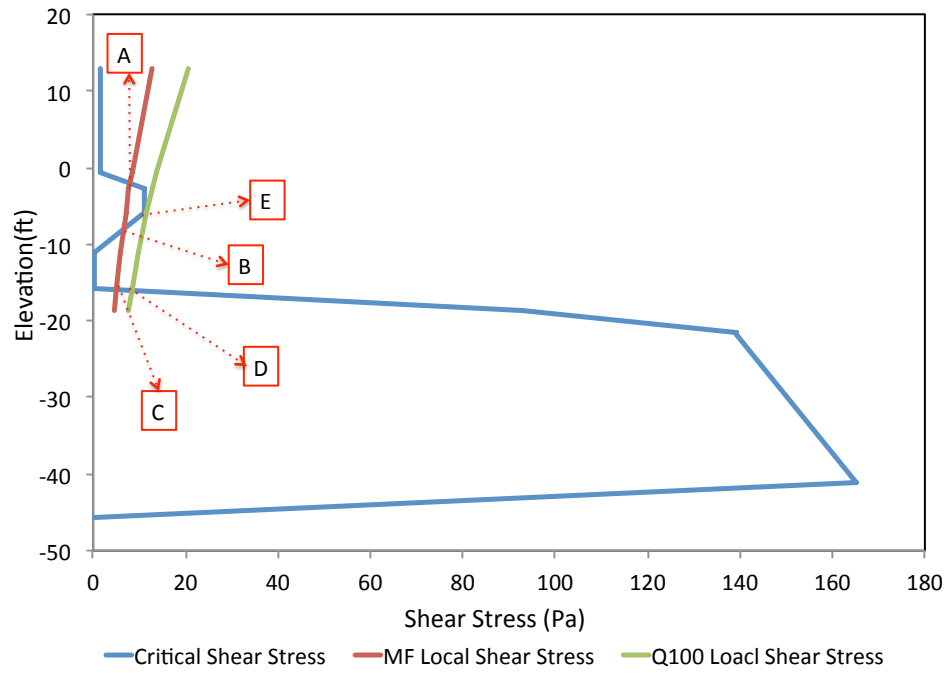


Figure 6.16 Erodibility of the soil at Pier 22

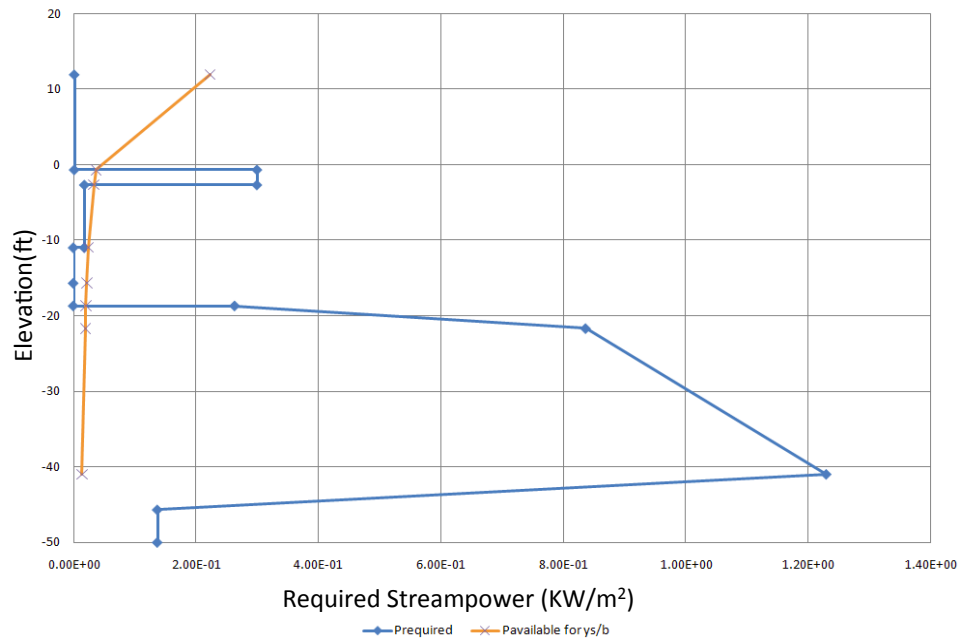


Figure 6.17 Erodibility of the soil at Pier 22 in the emergency study

6.5 Summary

In this chapter, the CFD models of the full-scale Feather River Bridge were developed. Wall shear stress distributions around Pier 22 on the bathymetries before and after the flood event under the same flow conditions were used to verify the decay trend of wall shear stress. The simulation results of O_B2007_MF, O_B2007_Q100 and O_B2011_MF were plotted with the decay function and envelope decay function. The envelope decay function covers all three data points. So, the envelope function is sufficient to the relation between wall shear stress and scour in the real world. The possible applications of the envelope function were also discussed in this chapter. However, limited by the number of the full-scale CFD models, this research is a kind of preliminary research.

Chapter 7 Conclusion and Future Work

7.1 Overview

Since scour has already been the biggest single reason of bridge failure in the United States, the study of pier scour and abutment scour attracts many researchers. The previous physical experiments conducted by Annandale states that there is a decay trend of hydraulic loading with scour. However, the current technology of physical experimental method faces problems of directly measure the hydraulic loading on a dynamic bed. CFD method cannot accurately simulate the scour process. A hybrid approach using a physical experimental method and a CFD method was developed to study the relation between wall shear stress and scour. In this dissertation, the development, validation and calibration of CFD models of this hybrid approach were discussed in detail. Based on the results of the developed hybrid approach, an envelope decay function of dimensionless wall shear stress and relative scour depth was developed and applied to analyze the pier scour problems. In this chapter, the conclusions of this dissertation are listed. The limitations of this research method are discussed. Future related works are discussed at the end of this chapter.

7.2 Conclusions

This dissertation can be generally separated into three parts: (1) CFD modeling for the physical experiments; (2) the development of the decay function of wall shear stress; and (3) development of CFD models of the full-scale Feather River Bridge to verify the decay function and discuss its applications.

7.2.1 CFD Modeling for Physical Experiments

With the surveyed bathymetries of a set of physical experiments, a series of CFD models were developed to simulate these cases. There are several conclusions achieved in this process. First, with an appropriate physical time, the unsteady CFD model developed in STAR-CCM+ represents the steady state results well. Second, the wall shear stress distributions around the pier clearly show a decaying trend of hydraulic loading (wall shear stress) with scour. The comparison between CFD simulation results using a DES model and unsteady RANS model shows that the wall shear stress distribution of these two kinds of models generally agree with each other, even though the results of the DES model include more details. During this process, a hybrid approach that combines a physical experimental method (to survey the scoured bathymetry) with a CFD method (to simulate water flow and calculate local shear stress) was finally developed to study pier the scour problem.

7.2.2 Decay Function and Envelope Function

To simplify the research, the bathymetry was formed with non-cohesive, clean and coarse sand ($d_{50} = 1\text{mm}$). In order to eliminate the potential influence of form drag caused by the shape change of the bathymetry, the value of wall shear stress on the point with the largest scour depth of each case was used to develop a decay function of dimensionless wall shear stress ($\frac{\tau_w}{\tau_a}$) with relative scour depth ($\frac{y_s}{y_{\max}}$). Even though this decay function was developed with the CFD simulation results of complex-shape piers, the CFD modeling results for a rectangular pier with a 30° attack angle indicate that this function also is good for describing the decaying trend of wall shear stress around a

regularly-shaped pier. The previous physical experimental data was used in this research to verify and calibrate this decay function. These data show that an envelope function is a safer option for describing the decaying trend. Therefore, a safety factor (2) was imported into the decay function to produce an envelope function, which includes almost all points (95%) of the current CFD data and previous experimental data.

7.2.3 CFD modeling for full-scale Feather River Bridge

The developed hybrid approach developed in this research was applied to study pier scour problem around Pier 22 of the Feather River Bridge. The bathymetries around Pier 22 before and after the flood event were surveyed with a sonar system. With these bathymetries, CFD models were developed to simulate water flows in the real world and calculate wall shear stress distributions around Pier 22. The bathymetry surveyed before the flood event was assumed to be non-scoured and the bathymetry after the flood event was assumed to be scoured. The wall shear stress distributions of CFD models were used to verify the decaying trend. The data points collected during these simulations are also within the envelope decay function. This suggests the envelope decay function can be applied to study other pier scour problems. With the analysis of the constituents of earthen material in each layer, this function can be applied to estimate the necessary depth of the foundation of a new pier or used to determine whether actions are needed to fix the pier scour problem around a given pier under given flow conditions.

7.3 Limitations

After this research, a hybrid approach to study pier scour was finally developed and an envelope decay function was developed to describe the relation between wall shear stress and scour. However, there are still some limitations of this research. First, this research does not actually develop the theories of scour. The developed method in this dissertation is still a kind of empirical method. Second, the figure, which includes the previous physical experimental data and CFD data, shows that the CFD wall shear stress values may be smaller than the true-values, even though this potential error is not obvious. This may be caused by the setting of the boundary type and the algorithm of the wall function and roughness function in STAR-CCM+. For CFD models of the full-scale Feather River Bridge, the extensive domain requires a relatively large base size to restrict the number of mesh cells. Generally speaking, a CFD model with denser mesh will provide more accurate simulation results. But, a denser mesh also requires more computer capacity. In this research, the mesh of the full-scale Feather River Bridge is not very fine. And the number of CFD models with a full-scale surveyed bathymetry around a bridge pier is not large enough. So, the study of application of the decay function in the real world is preliminary.

7.4 Future Work

In the future, there are some recommended studies to update the current research projects. There are also some studies in relation to the current research projects.

(1) The hybrid approach developed to study the scour problem in the research are still needs to be verified and improved. Therefore, additional similar physical

experiments and CFD models are recommended to be designed to better establish this hybrid approach. Moreover, more data are needed to verify and calibrate the decay function of wall shear stress.

(2) The current CFD simulation results, not only the CFD simulations of this research, express a potential problem. Even though the simulated wall shear stress distribution is reliable in STAR-CCM+, it is very possible that the calculated value of this software may be smaller than the truth-value. Therefore, more accurate wall functions and roughness functions are needed. Other kinds of turbulent models are worth to use to verify and calibrate the CFD models.

(3) In the current research, there are only two kinds of bathymetries surveyed in the field. In order to develop a better approach to apply the decay function to study pier scour problems, more bathymetries around bridge piers need to be surveyed to develop full-scale CFD models.

In summary, the future research should focus on two aspects. First, better physical models, especially wall functions and roughness function, are necessary to more accurately simulate water flows around piers. Second, more data are needed to make the conclusions and approach in this dissertation more established. The purpose of this research and potential future studies focus on developing a kind of empirical method for engineering applications to study pier scour problems.

References:

1. Ahmad, M. F., Dong, P., Mamat, M., Wan Nik, W. B., & Mohd, M. H. (2011). "The critical shear stresses for sand and mud mixture." *Applied Mathematical Sciences*, 5(2), 53-71.
2. Annandale, G. W. (1993). "Risk analysis of river bridge failure." *Proceedings of Hydraulic Engineering'93*, ASCE, San Francisco, CA
3. Annandale, G. (2006). "Scour technology: mechanics and engineering practice [M]." New York: McGraw-Hill.
4. Annandale, G., & Smith, S. P. (2001). "Calculation of Bridge Pier Scour Using the Erodibility Index Method (No. CDOT-DTD-R-2000-9)." Colorado Department of Transportation [Division of Transportation Development].
5. Arneson, L. A., Zevenbergen, L. W., Lagasse, P. F., & Clopper, P. E. (2012). "Evaluating scour at bridges (No. FHWA-HIF-12-003)."
6. Breusers, H. N. C., Nicollet, G., & Shen, H. W. (1977). "Local scour around cylindrical piers." *Journal of Hydraulic Research*, 15(3), 211-252.
7. Brezzi, F., Lipnikov, K., Shashkov, M., & Simoncini, V. (2007). "A new discretization methodology for diffusion problems on generalized polyhedral meshes." *Computer Methods in Applied Mechanics and Engineering*, 196(37), 3682-3692.
8. Chabert, J., & Engeldinge, J. (1956). "Etude des affouillements autour des piles de ponts[M]." *Laboratoire National d'Hydraulique*.
9. Chaudhry, M. H. (2007). "Open-channel flow." Springer Science & Business Media.

10. Chen, S., Johnson, D. B., Raad, P. E., & Fadda, D. (1997). The surface marker and micro cell method. *International Journal for Numerical Methods in Fluids*, 25(7), 749-778.
11. Dancey, C. L., Diplas, P., Papanicolaou, A., & Bala, M. (2002). "Probability of individual grain movement and threshold condition." *Journal of Hydraulic Engineering*, 128(12), 1069-1075.
12. Davidson, L. (2006). "MTF270 turbulence modeling." *The SST Model*, Chalmers University.
13. Dey, S. (2003). "Threshold of sediment motion on combined transverse and longitudinal sloping beds." *Journal of Hydraulic Research*, 41(4), 405-415.
14. Einstein, H. A., & Li, H. (1958). "The viscous sublayer along a smooth boundary." *Transactions of the American Society of Civil Engineers*, 123(1), 293-313.
15. Ettema, R. (1980). "Scour at bridge piers (No. 216 Monograph)."
16. Evans, M. W., Harlow, F. H., & Bromberg, E. (1957). "The particle-in-cell method for hydrodynamic calculations (No. LA-2139)." LOS ALAMOS NATIONAL LAB NM.
17. Ferreira, E. A., Dimakopoulos, A. S., & Ferreira, R. M. (2011). "CFD modeling of rough-bed open-channel flows." In *Congresso de Métodos Numéricos em Engenharia*.
18. Fromm, J. E., & Harlow, F. H. (1963). "Numerical solution of the problem of vortex street development." *Physics of Fluids (1958-1988)*, 6(7), 975-982.

19. Gentry, R. A., Martin, R. E., & Daly, B. J. (1966). "An Eulerian differencing method for unsteady compressible flow problems." *Journal of Computational Physics*, 1(1), 87-118.
20. Gilley, J. E., Elliot, W. J., Laflen, J. M., & Simanton, J. R. (1993). "Critical shear stress and critical flow rates for initiation of rilling." *Journal of Hydrology*, 142(1), 251-271.
21. Guo, J. (2002). "Hunter rouse and shields diagram." *Advances in Hydraulic and Water Engineering*, 2, 1096-1098.
22. Harlow, F. H. (1957). "Hydrodynamic problems involving large fluid distortions." *Journal of the ACM (JACM)*, 4(2), 137-142.
23. Harlow, F. H., & Welch, J. E. (1965). "Numerical calculation of time-dependent viscous incompressible flow of fluid with free surface." *Physics of fluids*, 8(12), 2182.
24. Hess, J. L., & Smith, A. O. (1967). "Calculation of potential flow about arbitrary bodies." *Progress in Aerospace Sciences*, 8, 1-138.
25. Hirt, C. W., & Nichols, B. D. (1981). "Volume of fluid (VOF) method for the dynamics of free boundaries." *Journal of computational physics*, 39(1), 201-225.
26. Hofland, B., Battjes, J. A., & Booij, R. (2005). "Measurement of fluctuating pressures on coarse bed material." *Journal of Hydraulic Engineering*, 131(9), 770-781.
27. Iaccarino, G., Ooi, A., Durbin, P. A., & Behnia, M. (2003). "Reynolds averaged simulation of unsteady separated flow." *International Journal of Heat and Fluid Flow*, 24(2), 147-156.

28. Jones, J. S., Kilgore, R. T., & Mistichelli, M. P. (1992). Effects of footing location on bridge pier scour. *Journal of Hydraulic Engineering*, 118(2), 280-290.
29. Kim, H. T., Kline, S. J., & Reynolds, W. C. (1971). "The production of turbulence near a smooth wall in a turbulent boundary layer." *J. Fluid Mech*, 50(1), 133-160.
30. Kim, J. Y., Ghajar, A. J., Tang, C., & Foutch, G. L. (2005). "Comparison of near-wall treatment methods for high Reynolds number backward-facing step flow." *International Journal of Computational Fluid Dynamics*, 19(7), 493-500.
31. Kolmogorov, A. N. (1941, January). "The local structure of turbulence in incompressible viscous fluid for very large Reynolds numbers." In *Dokl. Akad. Nauk SSSR* (Vol. 30, No. 4, pp. 301-305).
32. Landahl, M. T., & Mollo-Christensen, E. (1992). "Turbulence and random processes in fluid mechanics." Cambridge University Press.
33. Léonard, J., & Richard, G. (2004). "Estimation of runoff critical shear stress for soil erosion from soil shear strength." *Catena*, 57(3), 233-249.
34. Melville, B. W. (1984). "Live-bed scour at bridge piers." *Journal of Hydraulic Engineering*, 110(9), 1234-1247.
35. Melville, B. W. (1997). "Pier and abutment scour: integrated approach." *Journal of Hydraulic Engineering*, 123(2), 125-136.
36. Melville, B. W., & Chiew, Y. M. (1999). "Time scale for local scour at bridge piers." *Journal of Hydraulic Engineering*, 125(1), 59-65.
37. Melville, B. W., & Sutherland, A. J. (1988). "Design method for local scour at bridge piers." *Journal of Hydraulic Engineering*, 114(10), 1210-1226.

38. Milne-Thomson, L. M. (1973). "Theoretical aerodynamics, 4th." Dover Publications, New York
39. Müller, P. (2006). "The equations of oceanic motions." Cambridge University Press.
40. National Transportation Safety. (1988). "Collapse of New York Thruway (1-90) Bridge over the Schoharie Creek, near Amsterdam, New York, April 5, 1987." Highway Accident Report: NTSB/HAR-88/02, Washington, DC.
41. Nezu, I. (2005). "Open-channel flow turbulence and its research prospect in the 21st century." *Journal of Hydraulic Engineering*, 131(4), 229-246.
42. Noh, W. F., & Woodward, P. (1976). "SLIC (simple line interface calculation)." In *Proceedings of the Fifth International Conference on Numerical Methods in Fluid Dynamics June 28–July 2, 1976 Twente University, Enschede* (pp. 330-340). Springer Berlin Heidelberg.
43. Offen, G. R., & Kline, S. J. (1974). "Combined dye-streak and hydrogen-bubble visual observations of a turbulent boundary layer." *Journal of Fluid Mechanics*, 62(02), 223-239.
44. Offen, G. R., & Kline, S. J. (1975). "A proposed model of the bursting process in turbulent boundary layers." *Journal of Fluid Mechanics*, 70(02), 209-228.
45. Oliveto, G., & Hager, W. H. (2002). "Temporal evolution of clear-water pier and abutment scour." *Journal of Hydraulic Engineering*, 128(9), 811-820.
46. Orszag, S. A. (1970). "Analytical theories of turbulence." *Journal of Fluid Mechanics*, 41(02), 363-386.

47. Otsubo, K., & Muraoka, K. (1988). "Critical shear stress of cohesive bottom sediments." *Journal of Hydraulic Engineering*, 114(10), 1241-1256.
48. Pagan-Ortiz, J. E. (2002). "Impact of the Federal Highway Administration's Scour Evaluation Program in the United States of North America's Highway Bridges." In *First International Conference on Scour of Foundations*.
49. Papanicolaou, A. N., Diplas, P., Evaggelopoulos, N., & Fotopoulos, S. (2002). "Stochastic incipient motion criterion for spheres under various bed packing conditions." *Journal of Hydraulic Engineering*, 128(4), 369-380.
50. Parola, A. C., Mahavadi, S. K., Brown, B. M., & El Khoury, A. (1996). "Effects of rectangular foundation geometry on local pier scour." *Journal of Hydraulic Engineering*, 122(1), 35-40.
51. Pope, S. B. (2000). "Turbulent Flows." Cambridge University Press.
52. Richardson, E. V. and Davis, S. R. (2001). "Evaluating scour at bridges, 4nd ed." FHWA NHI 01-001 HEC-18, National Technical Information Service, Spring, VA.
53. Rodi, W., Constantinescu, G., & Stoesser, T. (2013). "Large-eddy simulation in hydraulics." CRC Press.
54. Samir Muzaferija and Milovan Perić. (2013). "Simulation of Free-Surface Flows With STAR-CCM+."
55. Shen, H. W., Schneider, V. R., & Karaki, S. S. (1966). "Mechanics of Local Scour: Supplement, Methods of Reducing Scour." Civil Engineering Department, Engineering Research Center, Colorado State University.

56. Shields, A. (1936). "Application of similarity principles and turbulence research to bed-load movement." Soil Conservation Service.
57. Shih, T. H., Liou, W. W., Shabbir, A., Yang, Z., & Zhu, J. (1995). A new $k-\epsilon$ eddy viscosity model for high Reynolds number turbulent flows. *Computers & Fluids*, 24(3), 227-238.
58. Smagorinsky, J. (1963). "General circulation experiments with the primitive equations: I. the basic experiment*." *Monthly weather review*, 91(3), 99-164.
59. Smith, S. P., & Annandale, G. W. (1997). "Scour in Erodible Rock II: Erosive Power at Bridge Piers." In *North American Water and Environment Congress & Destructive Water* (pp. 1349-1357). ASCE.
60. Spalart, P. R., Jou, W. H., Strelets, M., & Allmaras, S. R. (1997). "Comments on the feasibility of LES for wings, and on a hybrid RANS/LES approach." *Advances in DNS/LES*, 1, 4-8.
61. Squires, K. D. (2004). "Detached-eddy simulation: current status and perspectives." In *Direct and large-eddy simulation V* (pp. 465-480). Springer Netherlands.
62. Suaznabar, O., Chen, L., & Kerényi, K. (2014). "Feather River Bridge Pier Scour Study." National Hydraulic Engineering Conference, Iowa City, IA.
63. Szymkiewicz, R. (2010). "Numerical modeling in open channel hydraulics (Vol. 83)." Springer Science & Business Media.
64. Tulimilli, B. R., Lottes, S. A., Majumdar, P., & Kostic, M. (2011, January). "Three-Dimensional Scouring Analysis for Open Channel Pressure Flow Scour Under Flooded Bridge Decks." In *ASME 2011 International Mechanical*

Engineering Congress and Exposition (pp. 975-981). American Society of Mechanical Engineers.

65. Vanoni, V. A. (1964). "Measurements of critical shear stress for entraining fine sediments in a boundary layer."
66. Wardhana, K., & Hadipriono, F. C. (2003). "Analysis of recent bridge failures in the United States." *Journal of Performance of Constructed Facilities*, 17(3), 144-150.
67. Wu, W., Rodi, W., & Wenka, T. (2000). "3D numerical modeling of flow and sediment transport in open channels." *Journal of Hydraulic Engineering*, 126(1), 4-15.
68. Xie, Z. (2011). "Theoretical and numerical research on sediment transport in pressurised flow conditions." Ph.D. thesis, Univ. of Nebraska-Lincoln, Lincoln, NE.
69. Yao Z, (2002). "Application of Acoustic Doppler Current Profiler in River Flow Measurement [J]." *Pearl River*, 23(06): 23. (In Chinese)
70. Zhai, Y. (2012). "CFD modeling of fish passage in large culvert and assistance for culvert design with fish passage." Ph.D. thesis, Univ. of Nebraska-Lincoln, Lincoln, NE.
71. STAR-CD Version 7.06 User Guide, CD-ADAPCO Inc, 2012
72. ANSYS-Fluent Version 12.0 User Guide, ANSYS Inc, 2009
73. http://en.wikipedia.org/wiki/Volume_of_fluid_method
74. <http://www.fhwa.dot.gov/publications/research/infrastructure/hydraulics/12022/004.cfm>

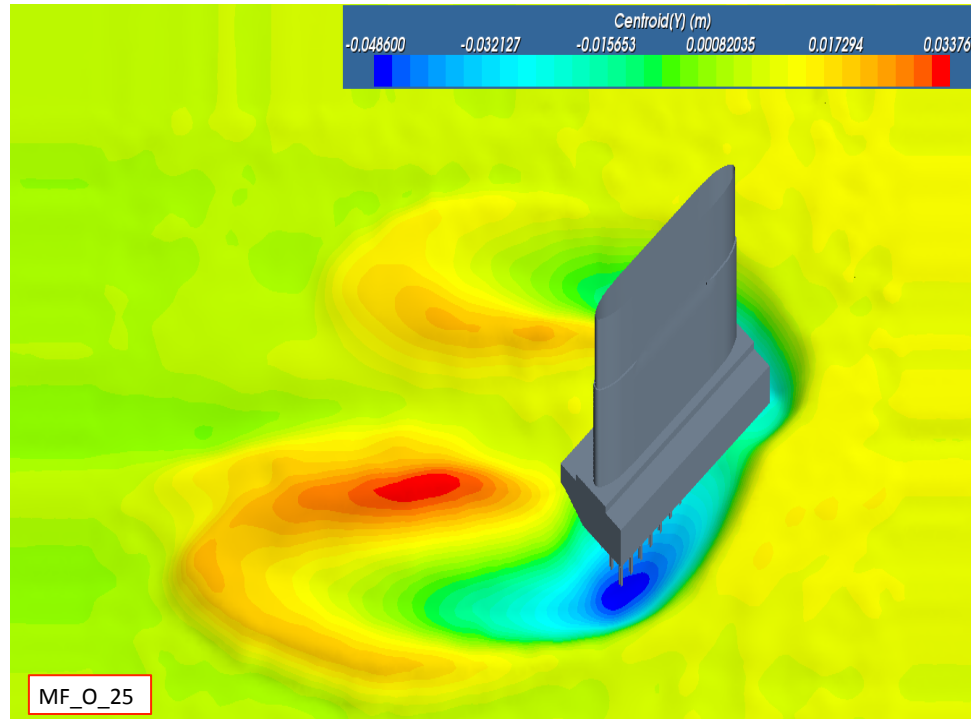
75. https://wiki.anl.gov/tracc/STAR-CCM%2B_Technical_Notes
76. <http://www.computationalfluidynamics.com.au/turbulence-part-3-selection-of-wall-functions-and-y-to-best-capture-the-turbulent-boundary-layer/>

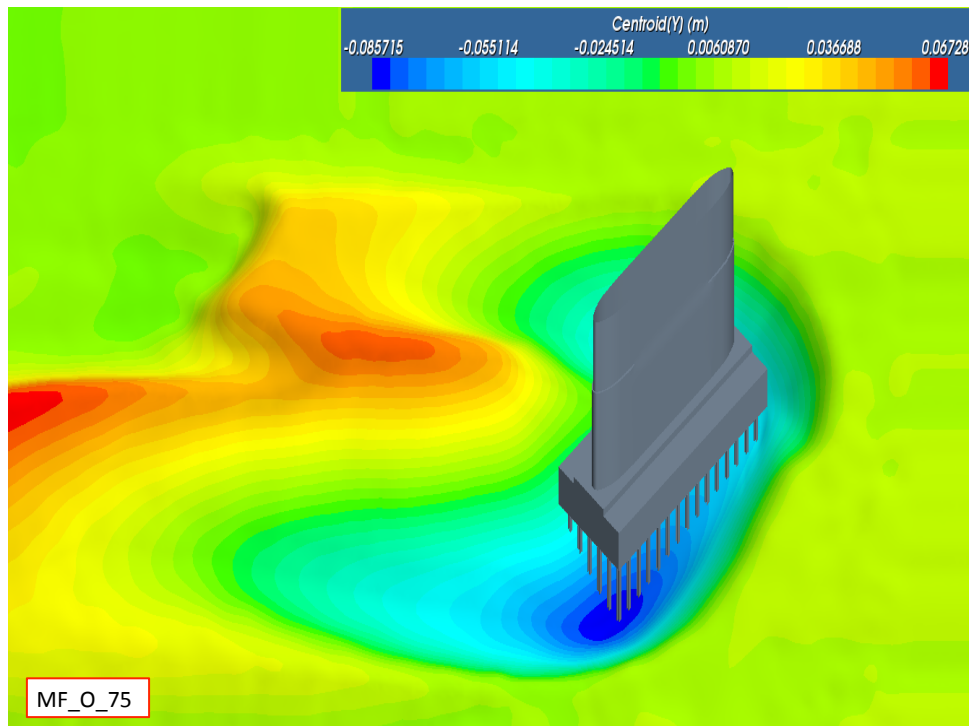
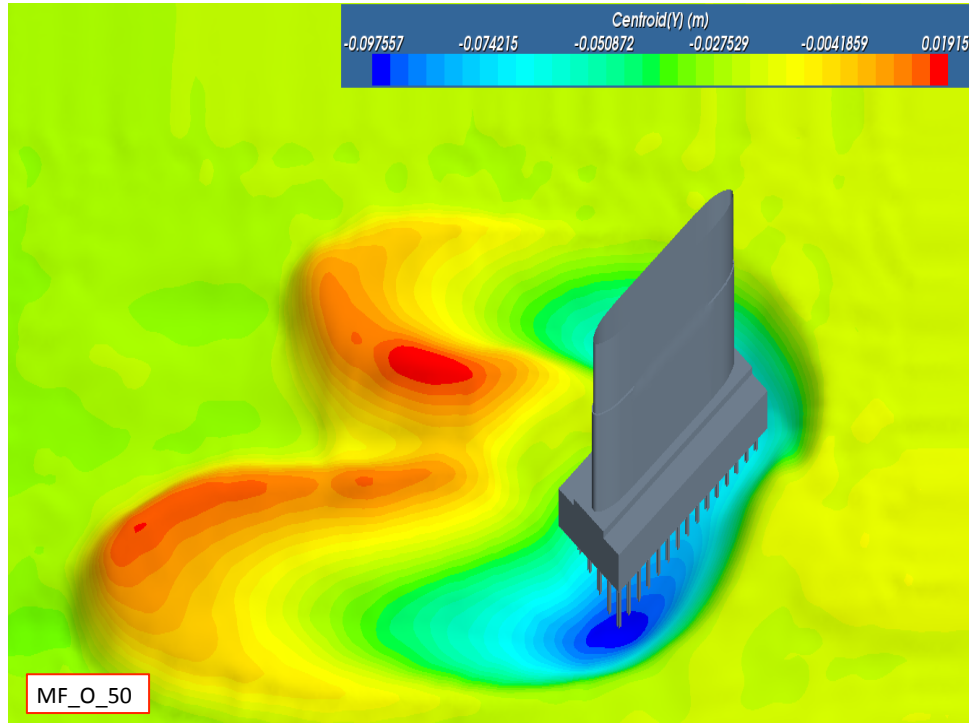
APPENDIX A. Scour Bathymetries around Piers

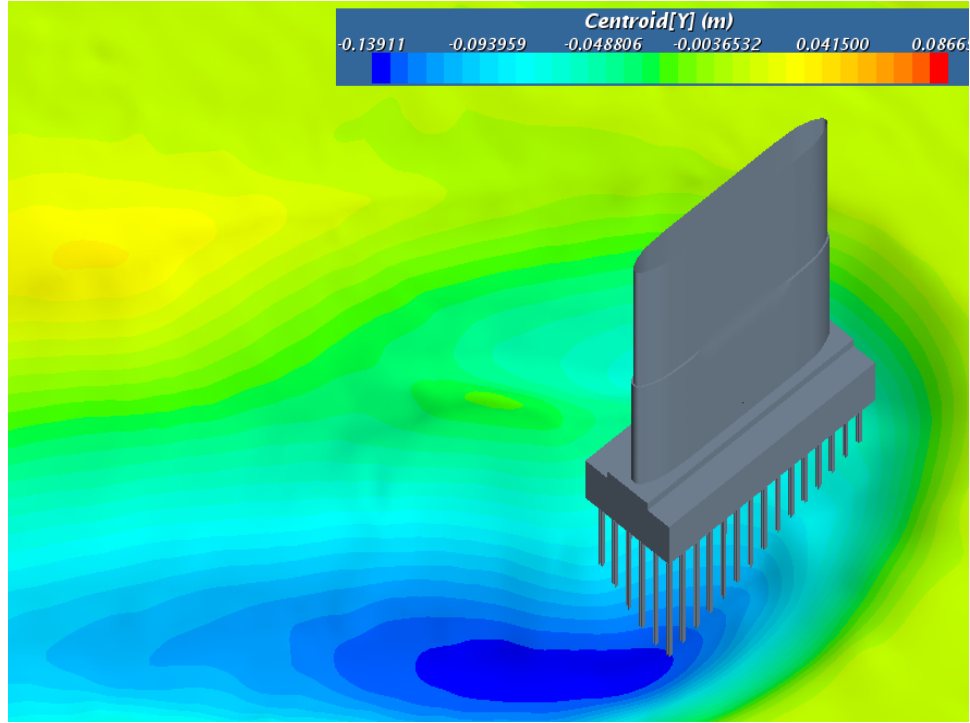
Scoured bathymetries around the original pier under the normal flow condition

(Cases in Group MF_O)

Note: the scale of each picture is different



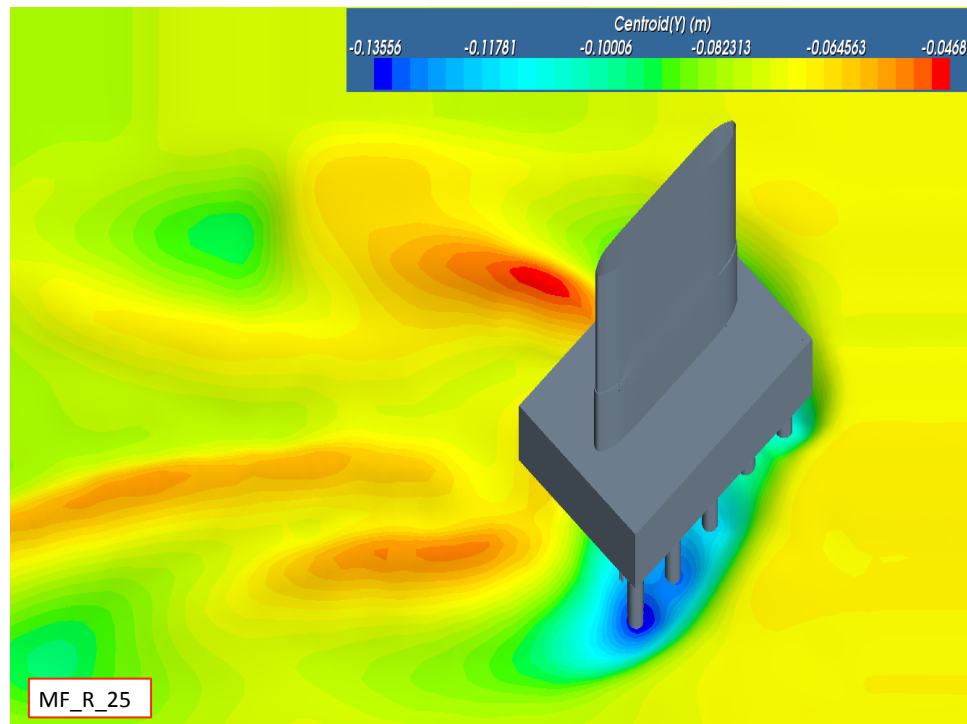


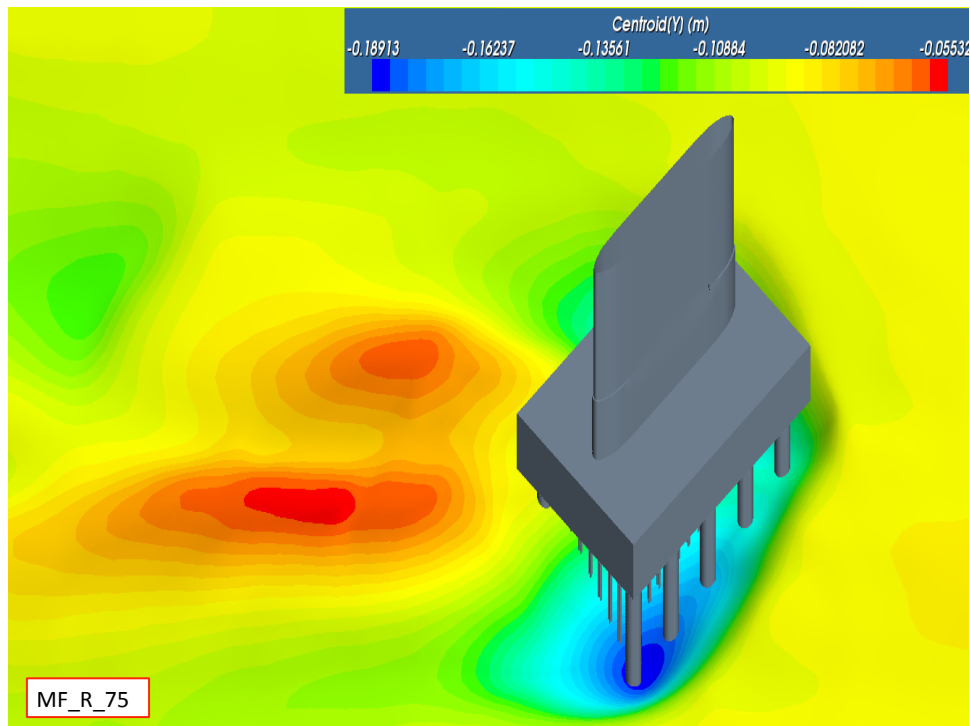
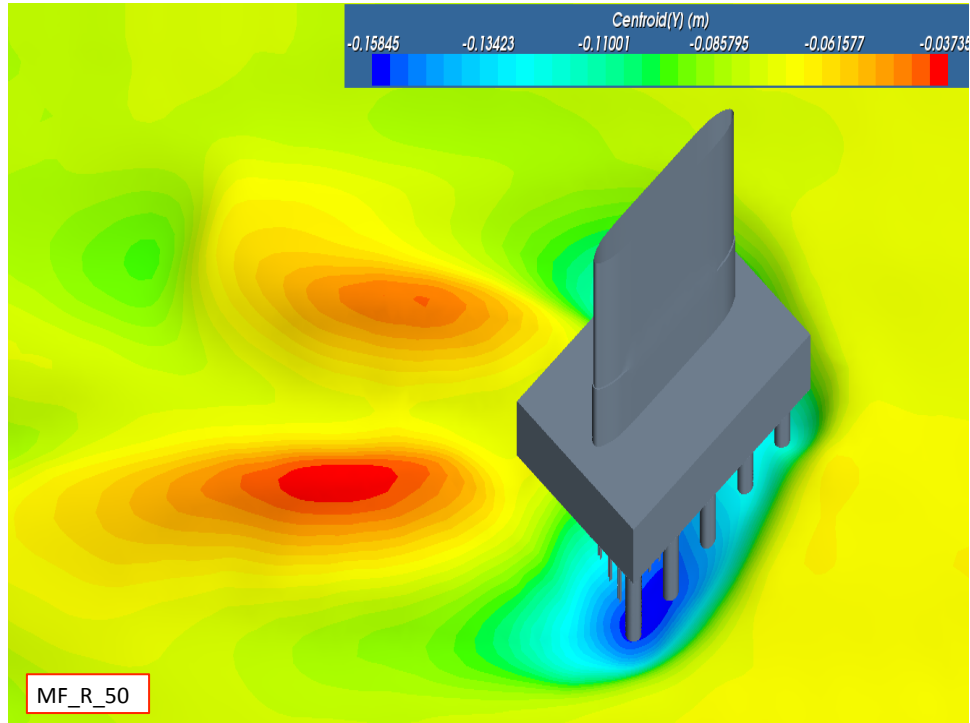


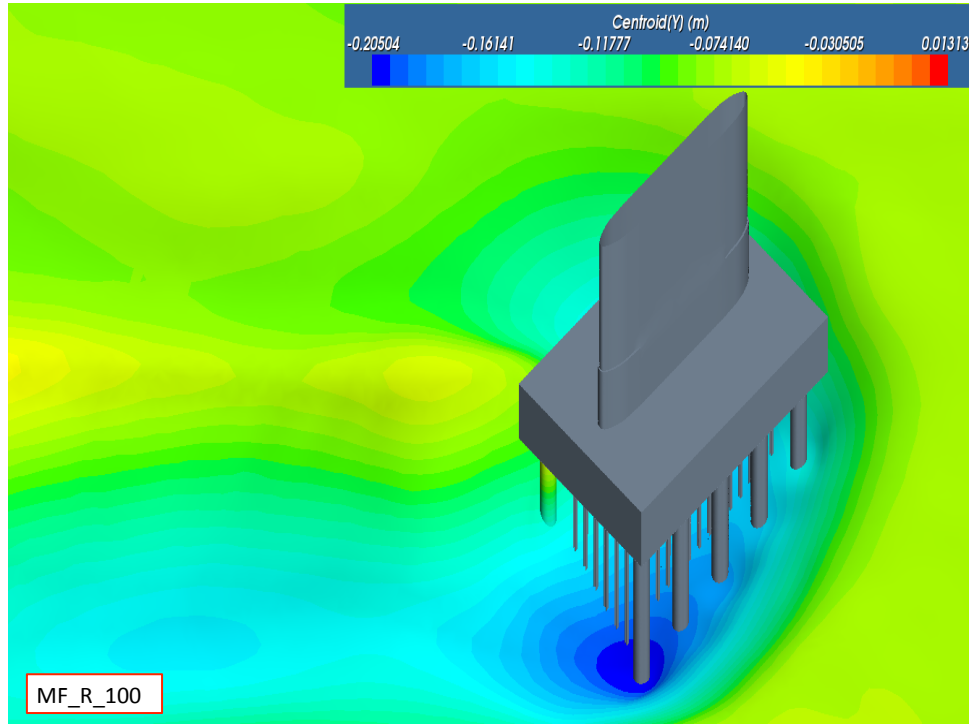
Scoured bathymetries around the retrofitted pier under the normal flow condition

(Cases in Group MF_R)

Note: the scale of each picture is different



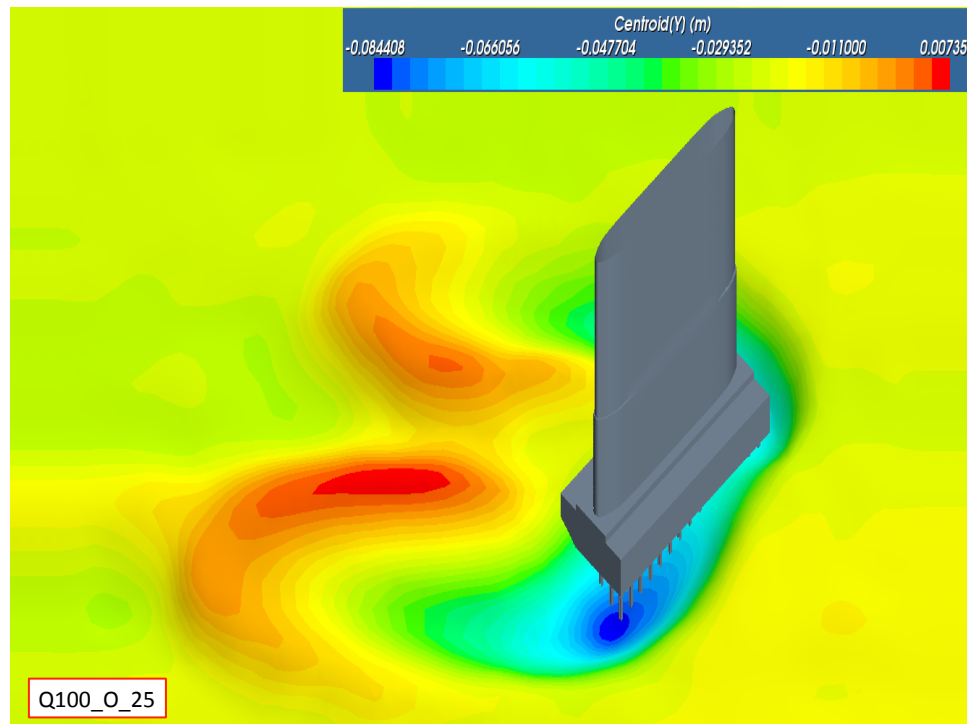


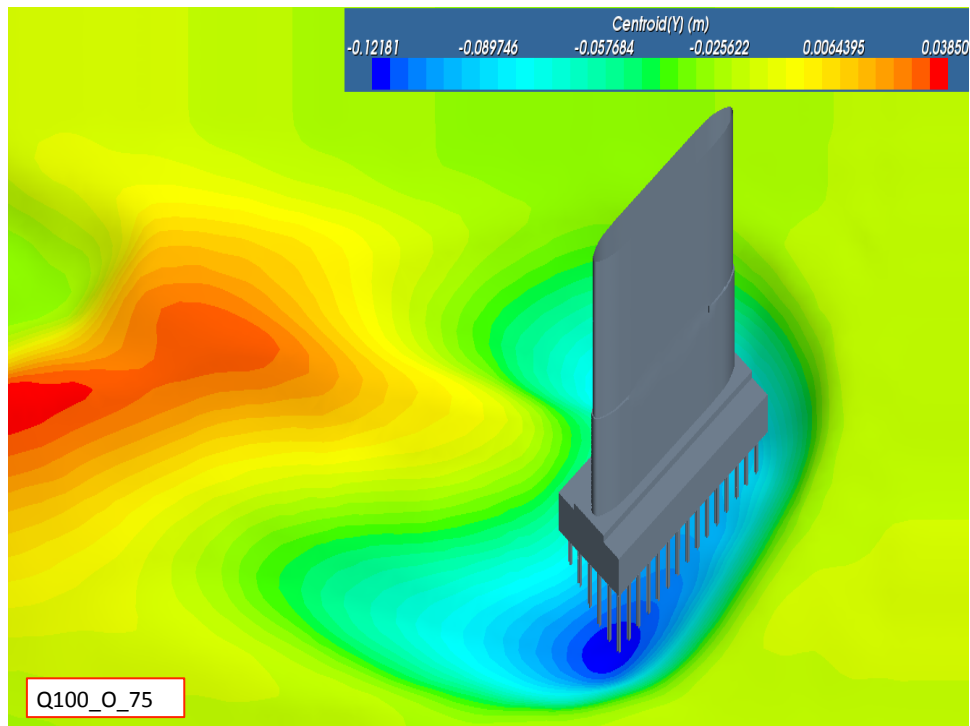
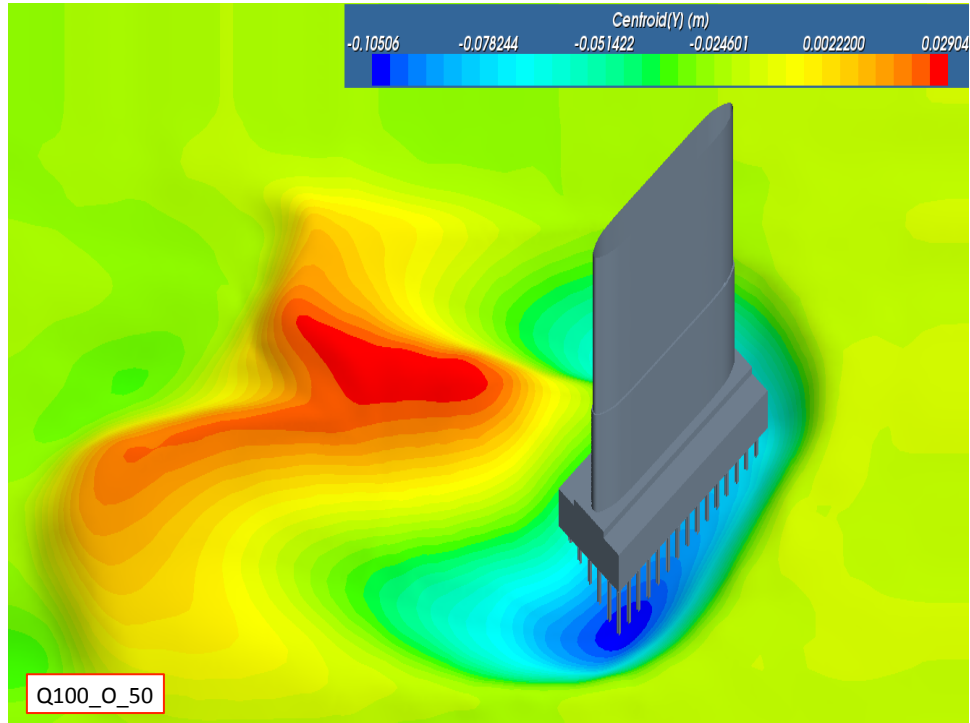


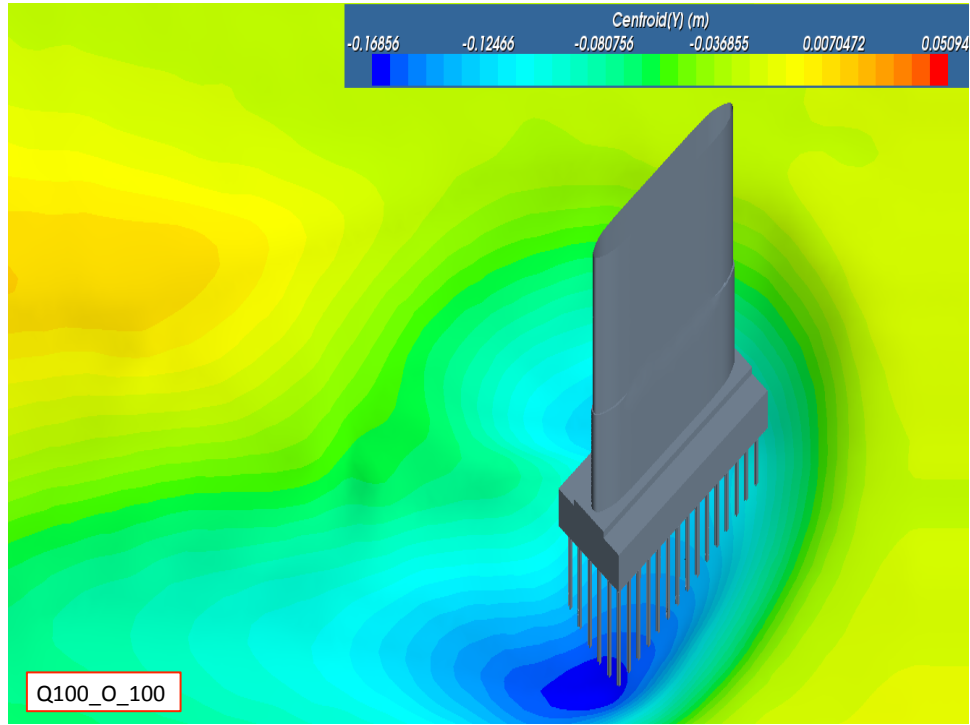
Scoured bathymetries around the original pier under the flow condition of the flood event

(Cases in Group Q100_O)

Note: the scale of each picture is different



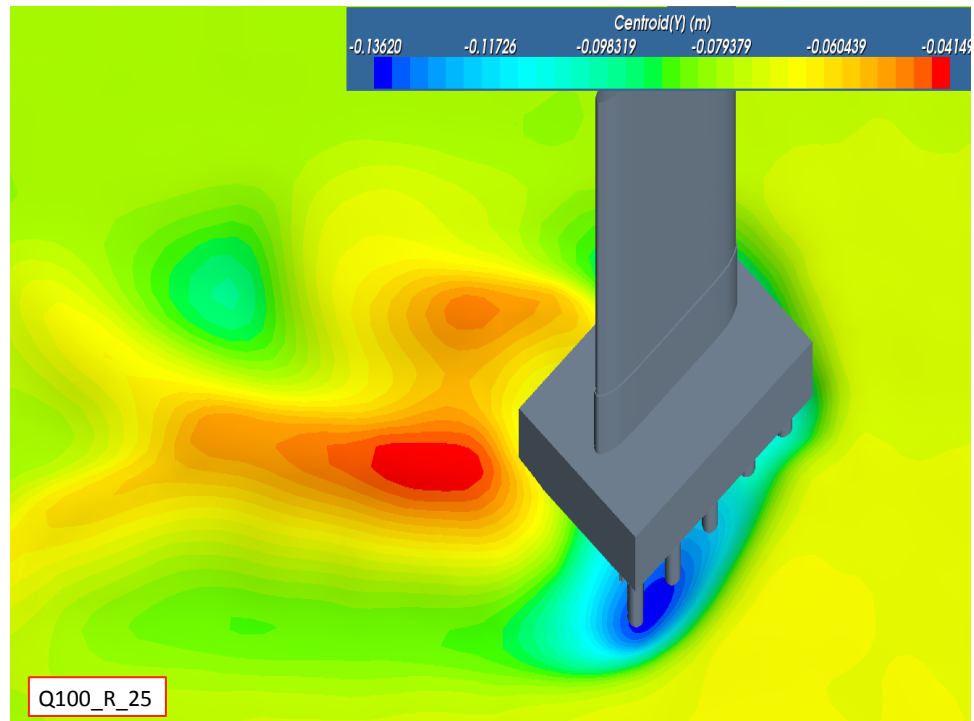


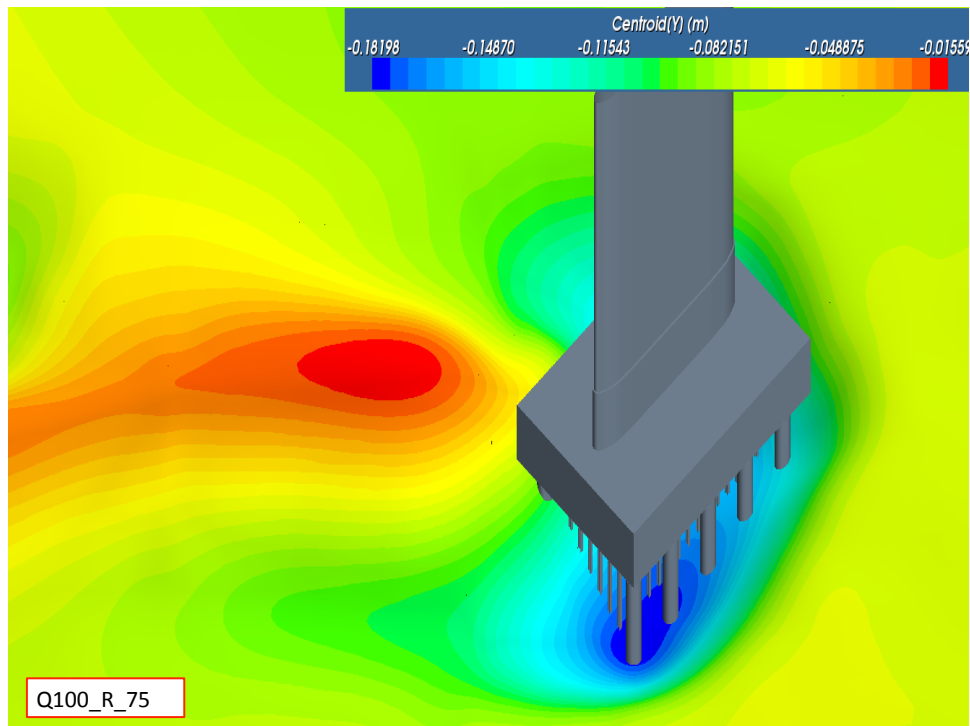
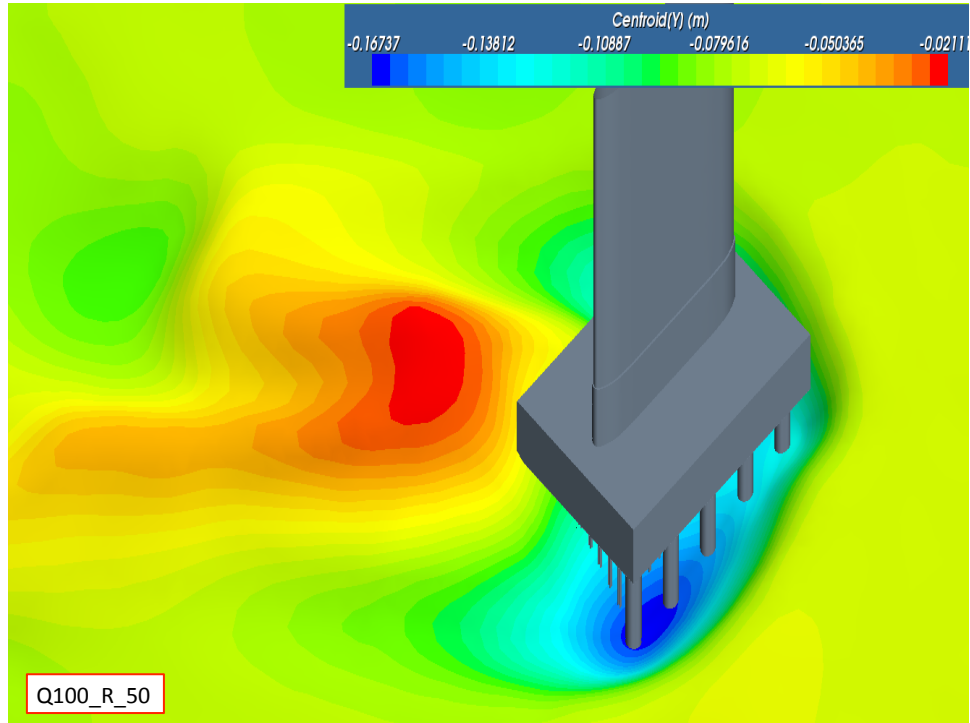


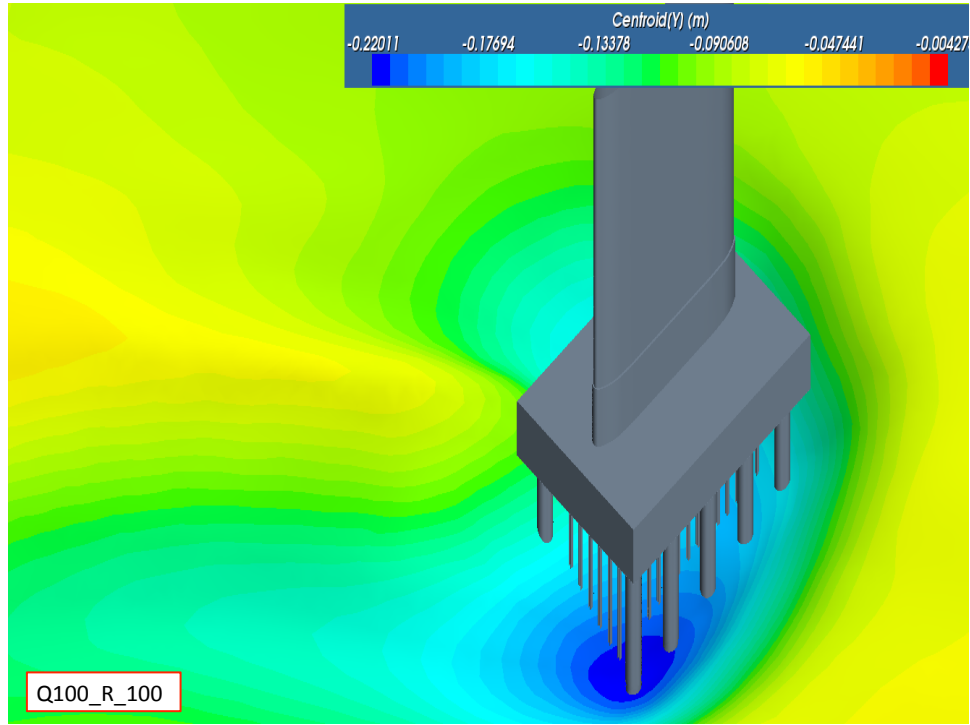
Scoured bathymetries around the retrofitted pier under the flow condition of the flood event

(Cases in Group Q100_R)

Note: the scale of each picture is different



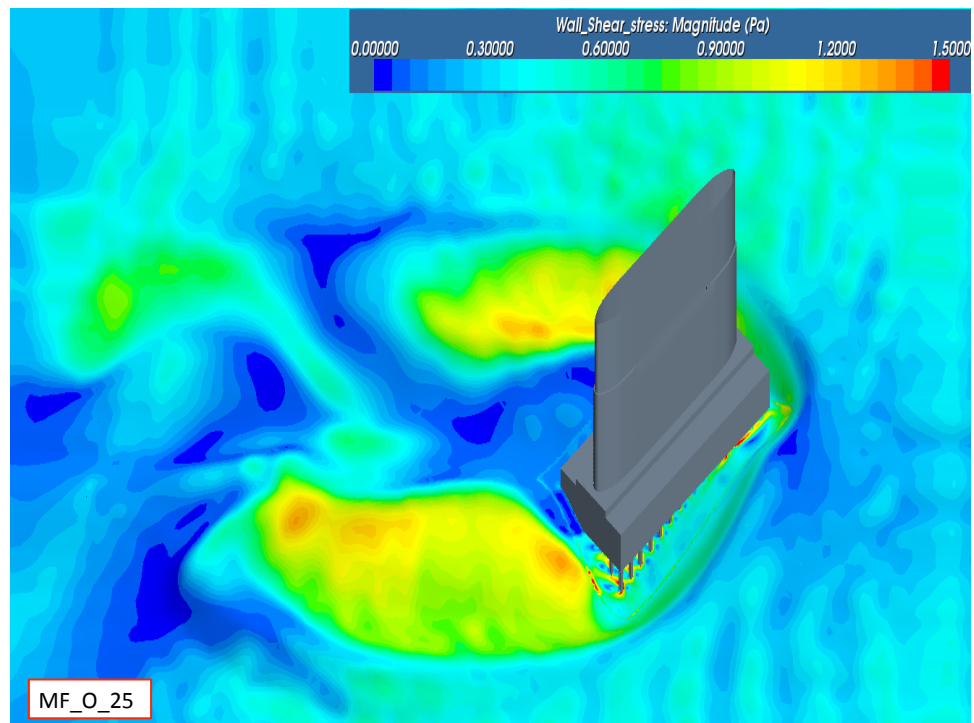
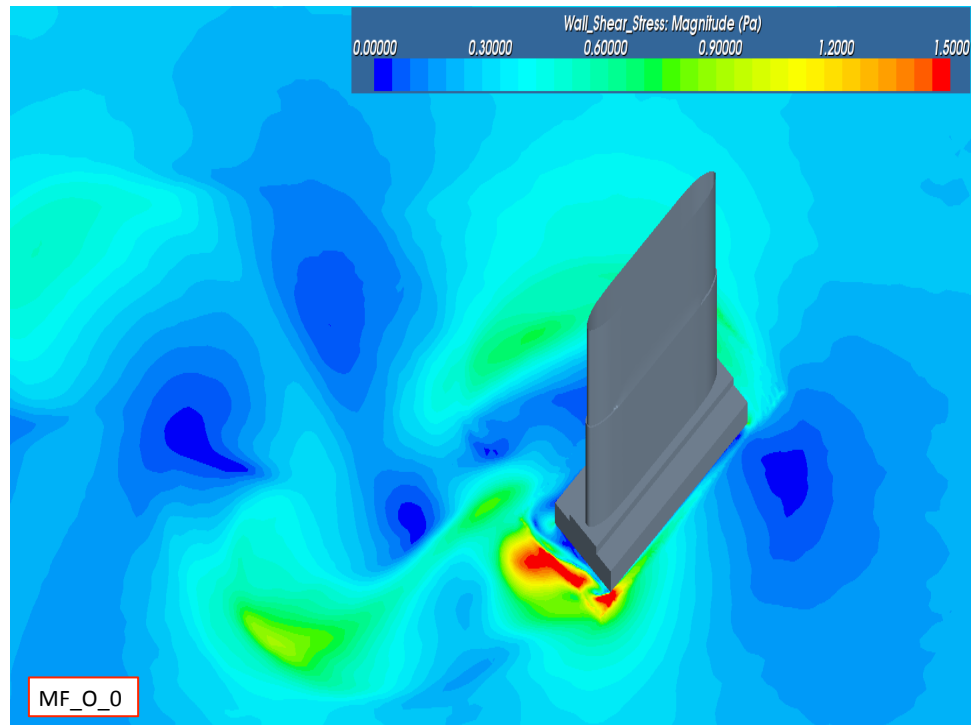


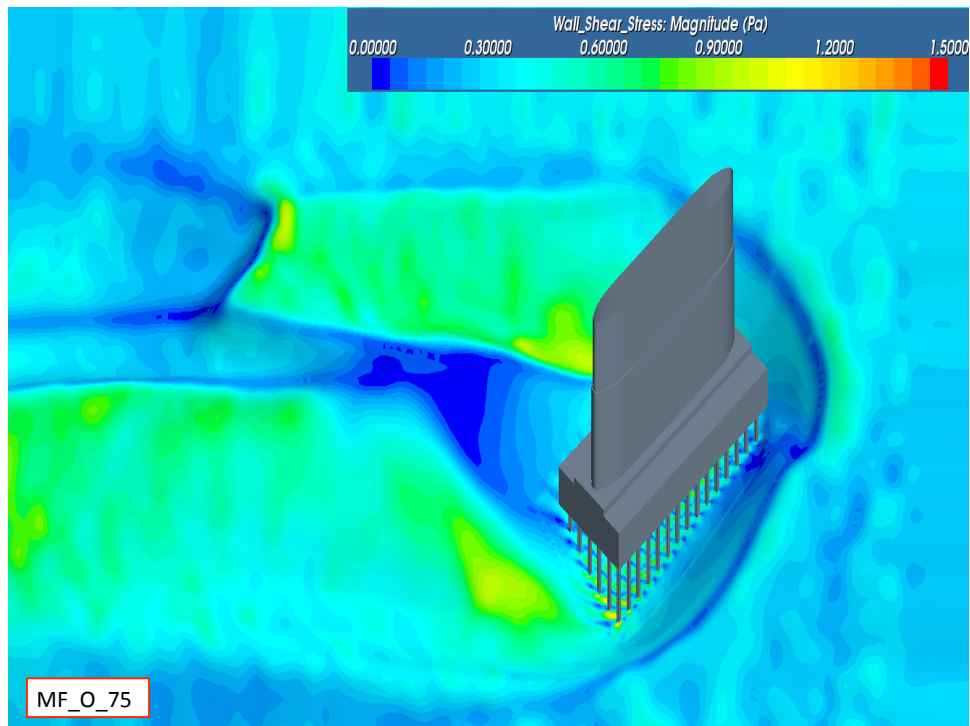
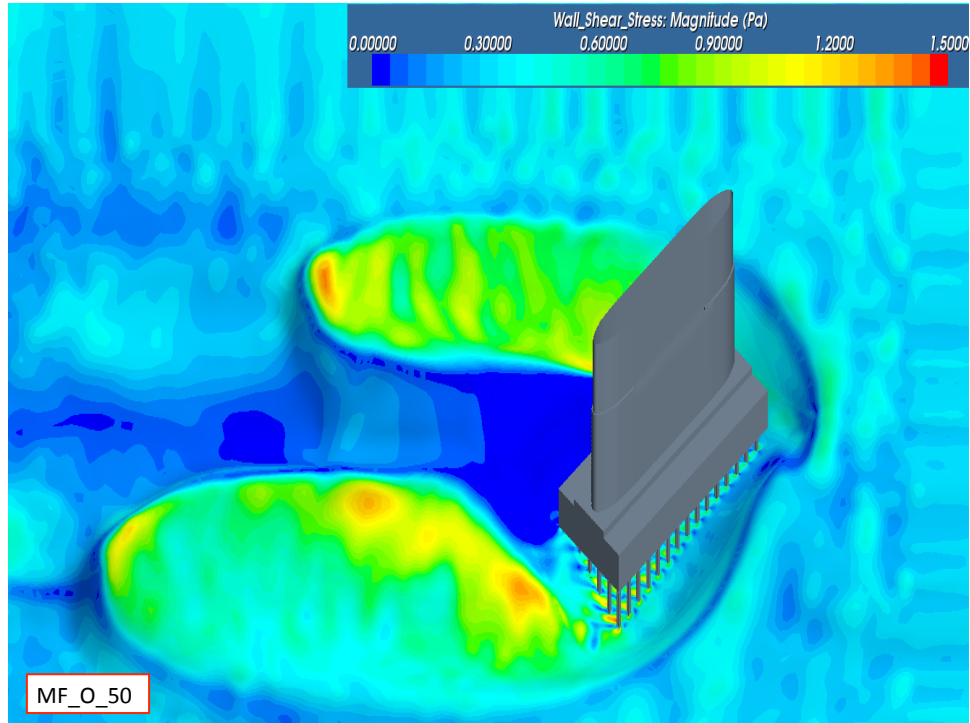


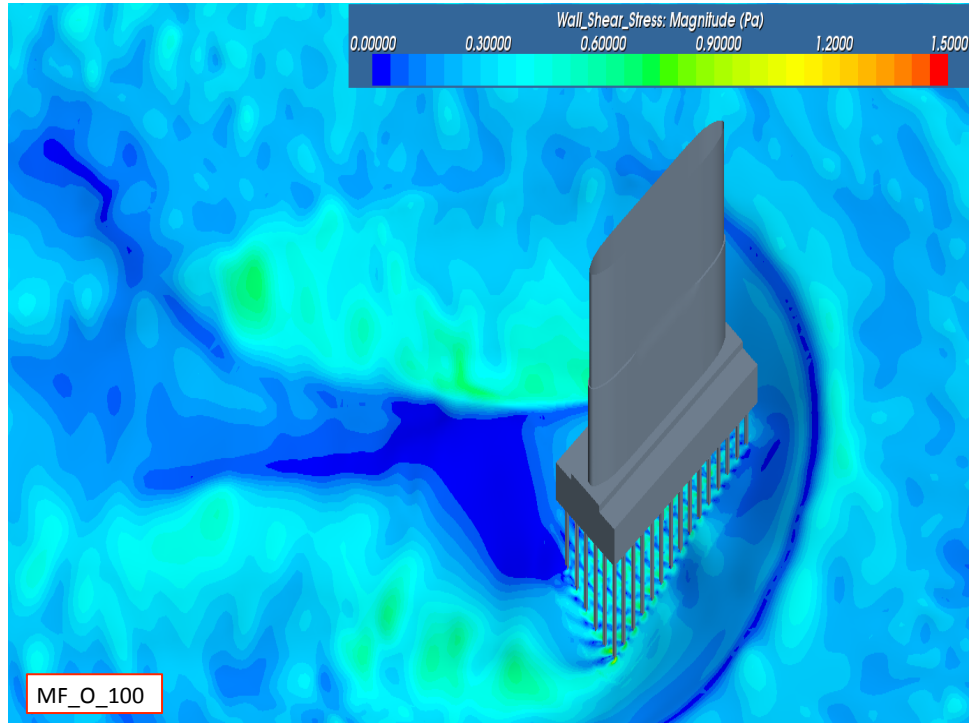
APPENDIX B. Wall Shear Stress Distribution of Cases of the Physical Experiment

Wall shear stress distributions around the original pier under the normal flow condition

(Cases in Group MF_O)

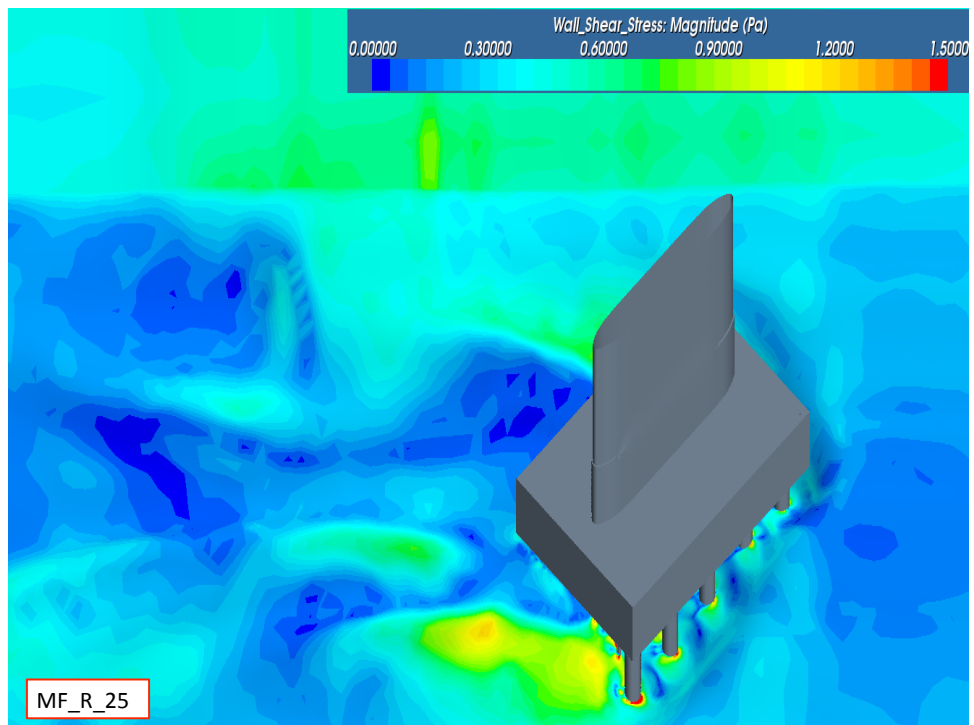
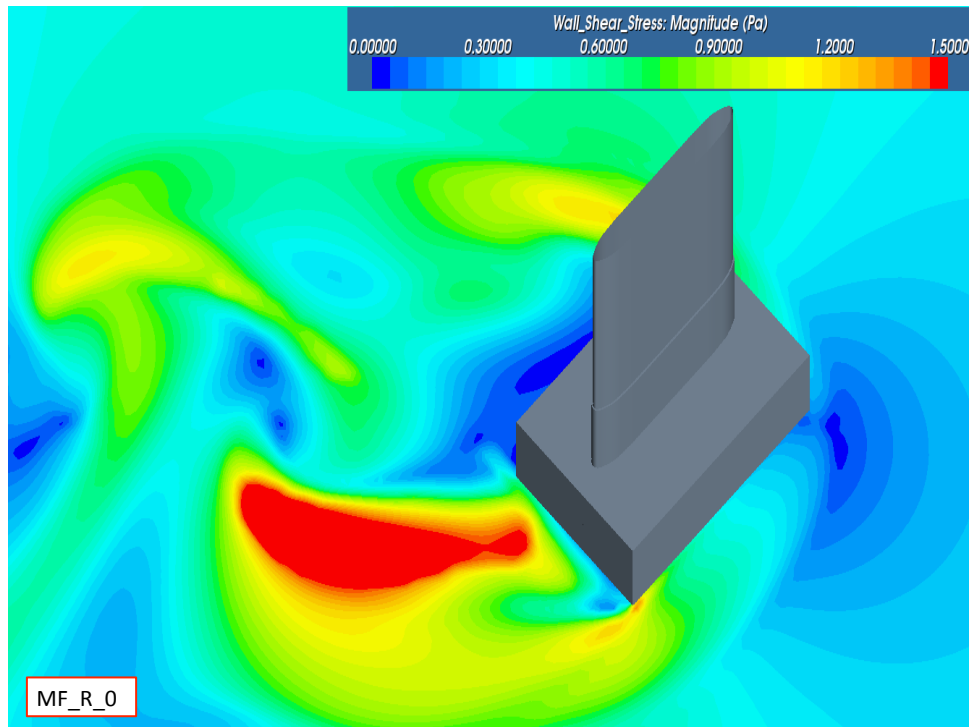


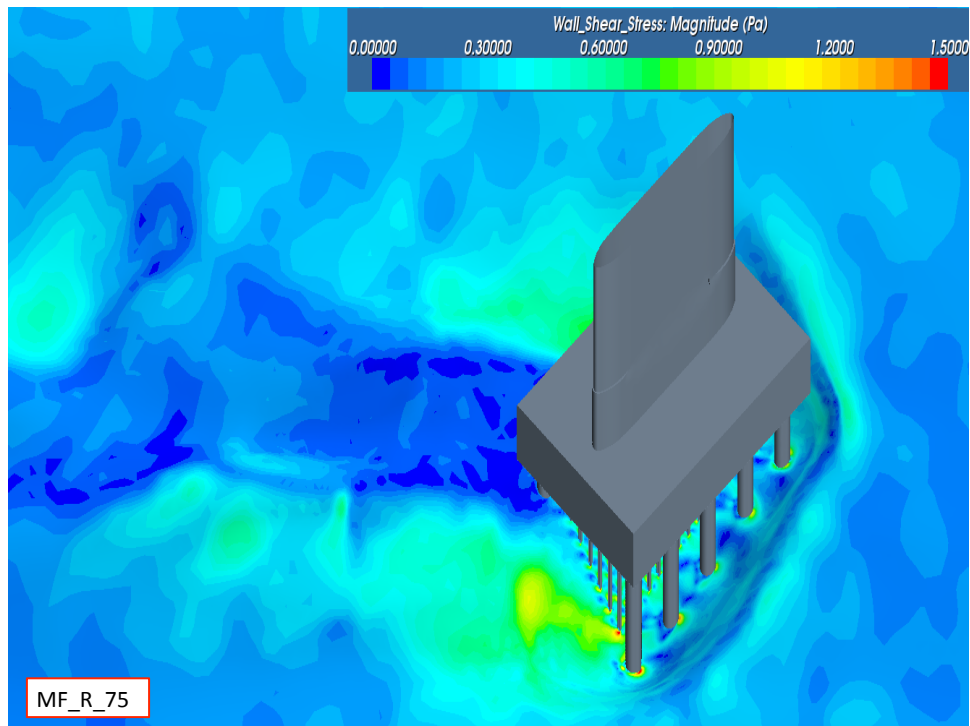
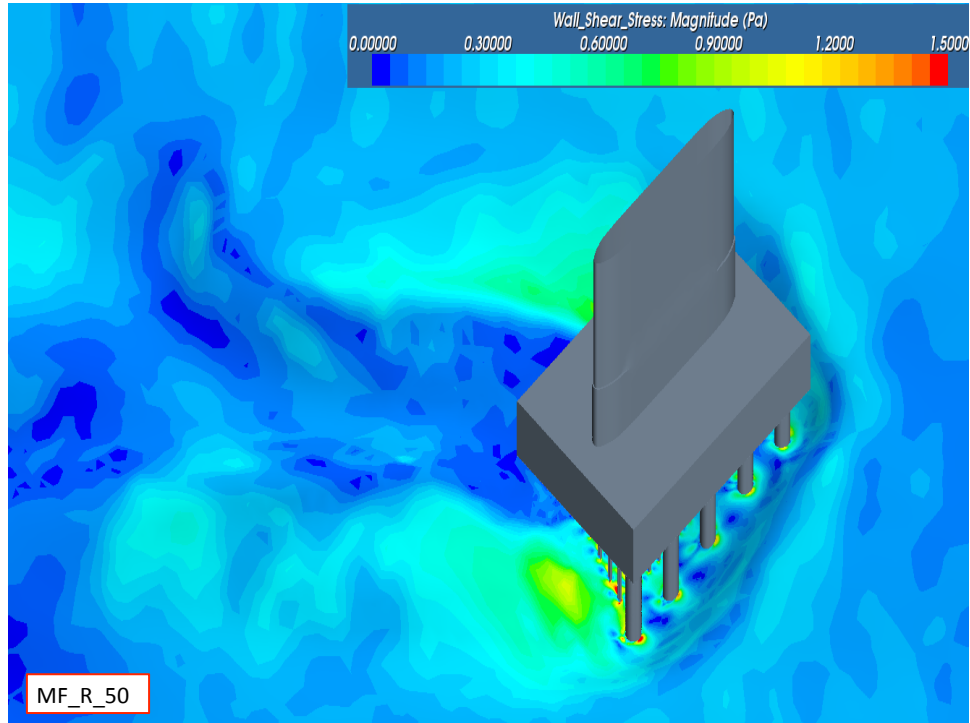


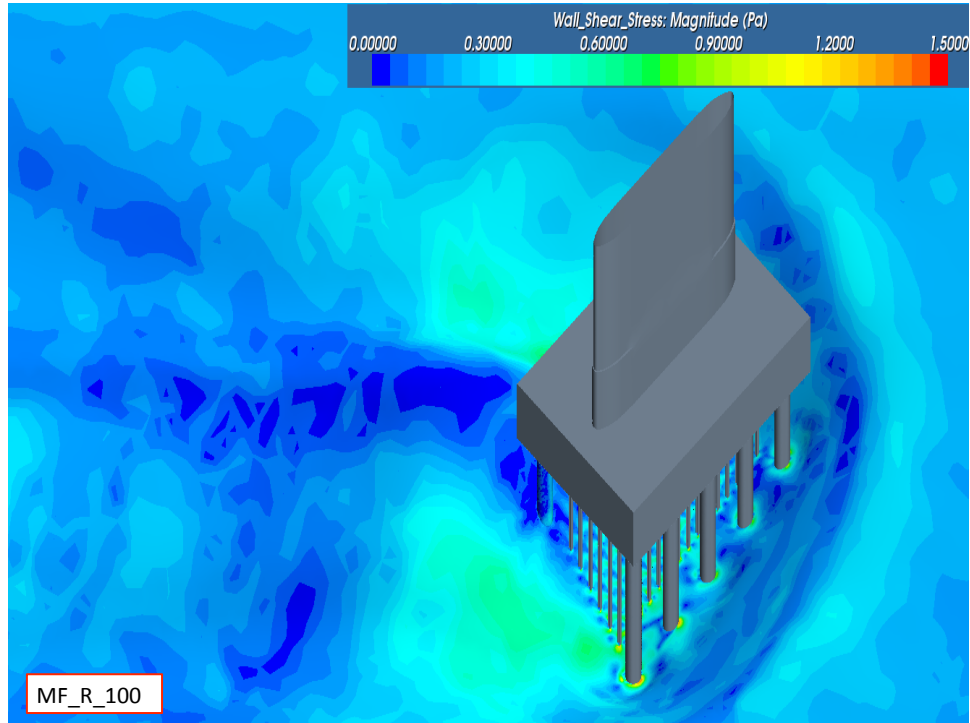


Wall shear stress distributions around the retrofitted pier under the normal flow condition

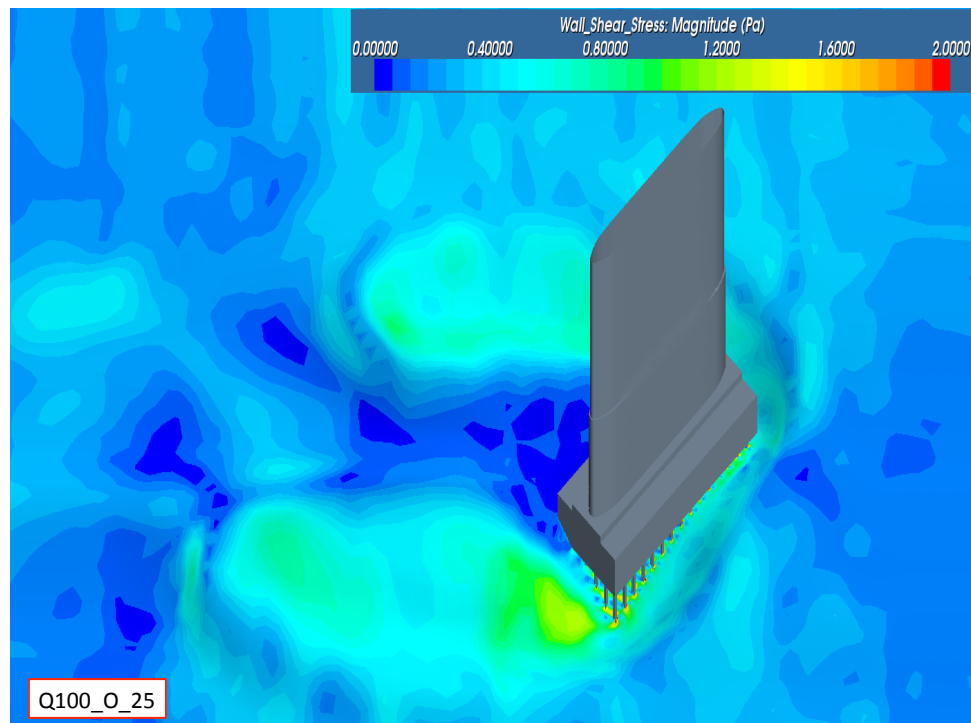
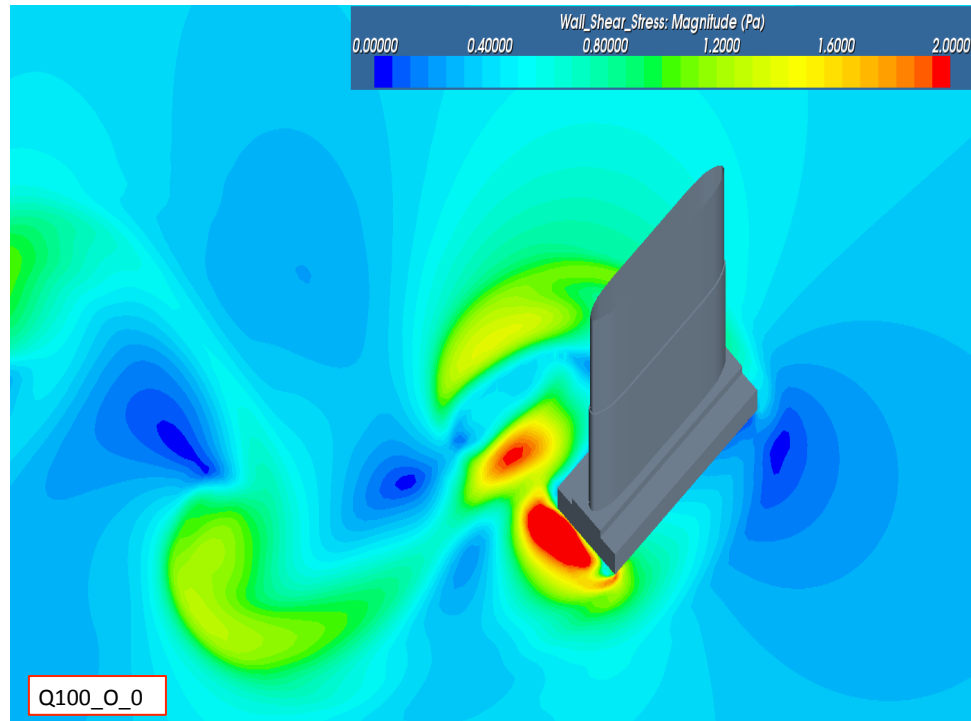
(Cases in Group MF_R)

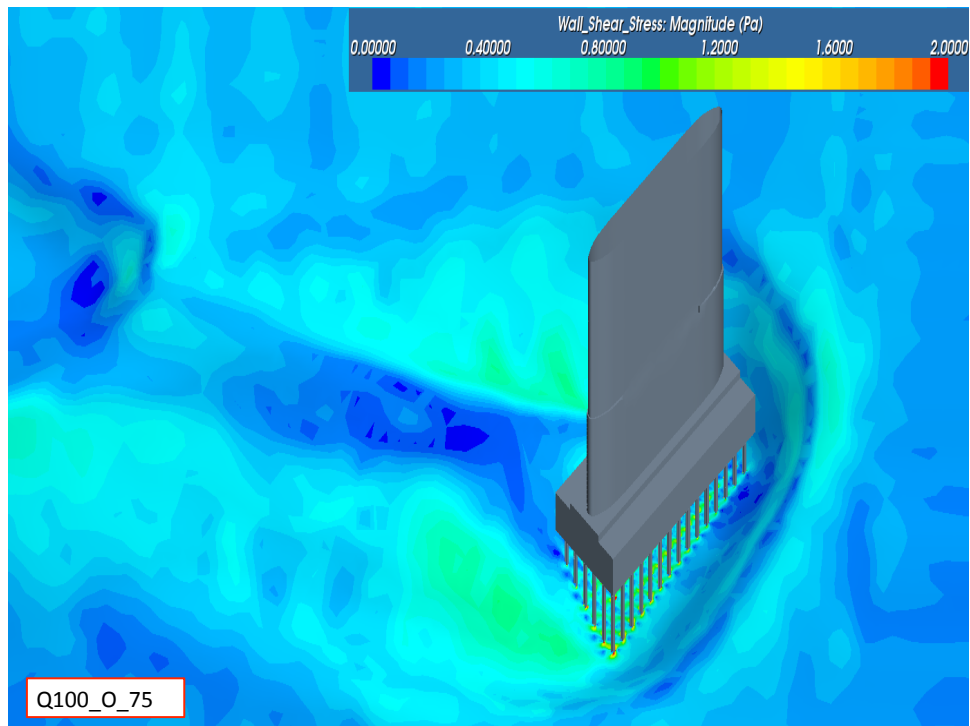
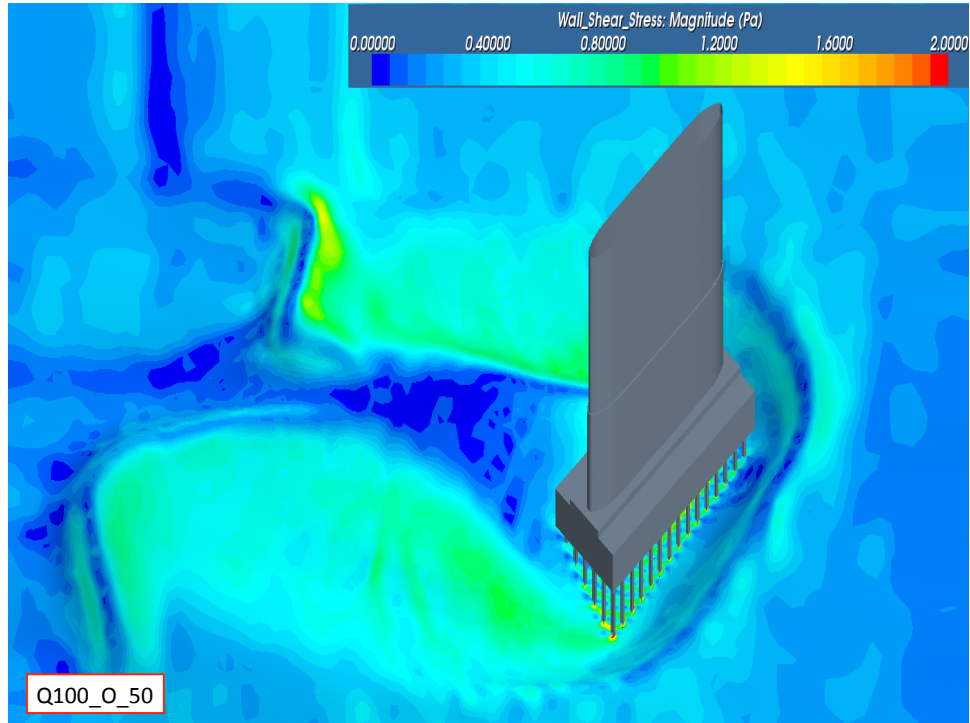


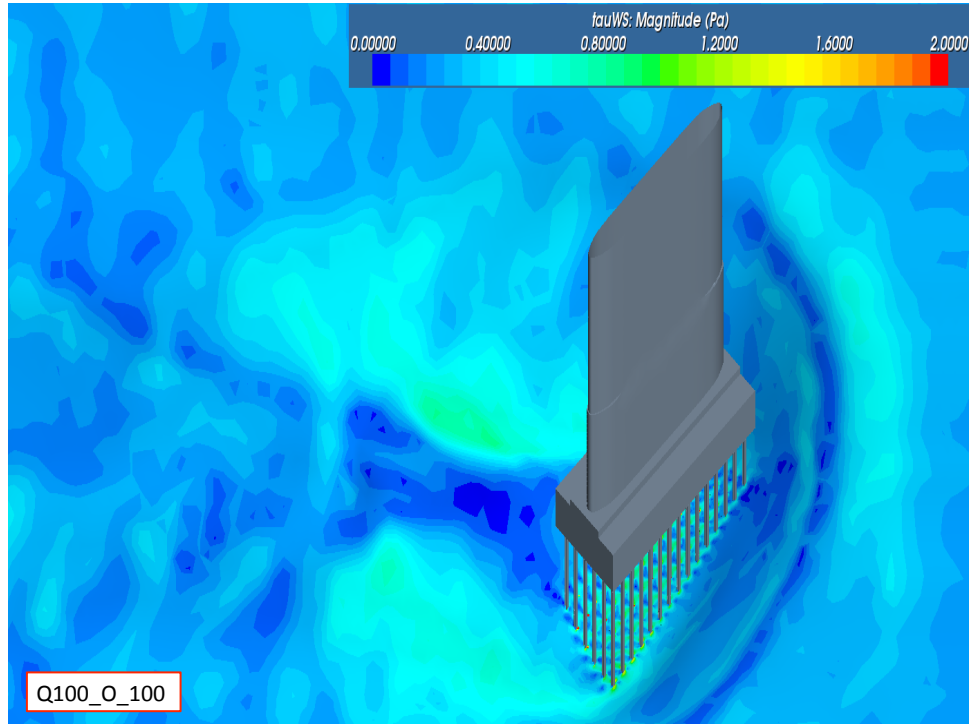




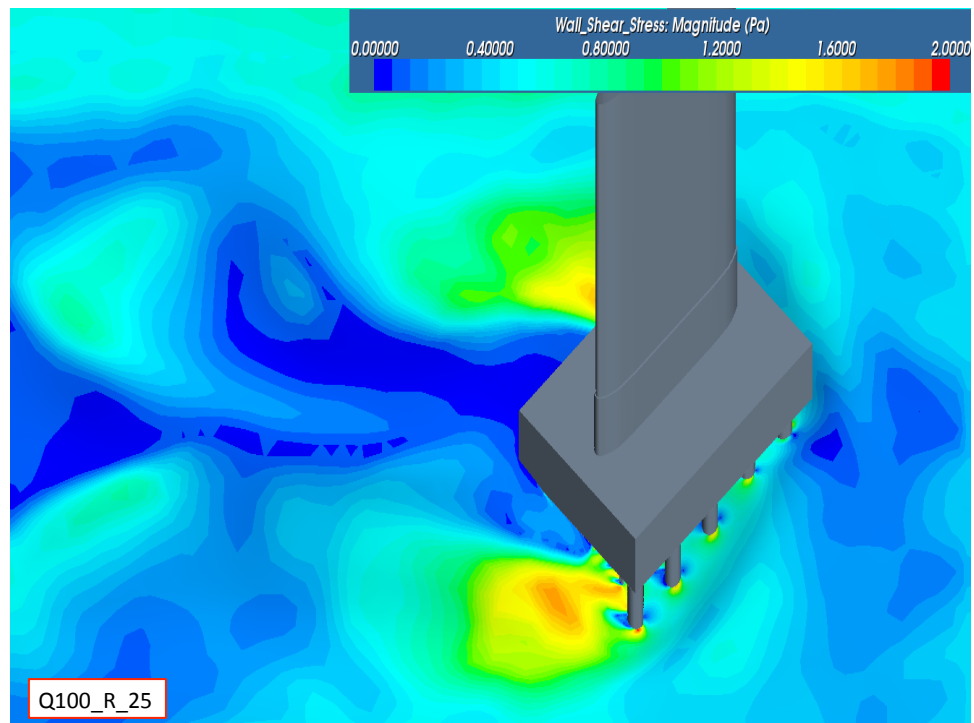
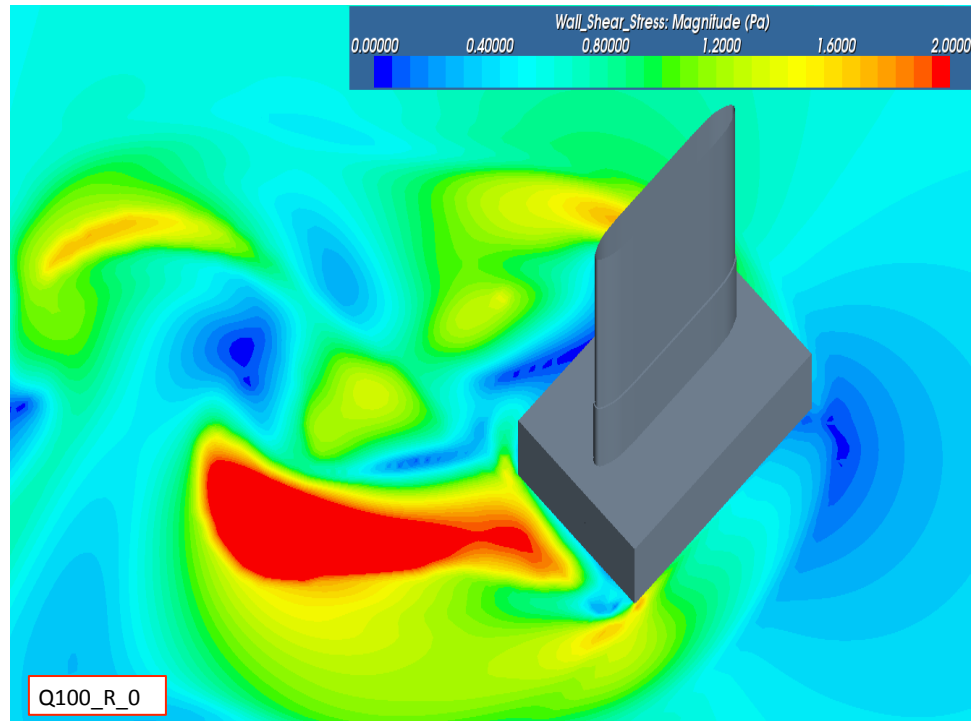
Wall shear stress distributions around the original pier under the flow condition of the
flood event
(Cases in Group Q100_O)

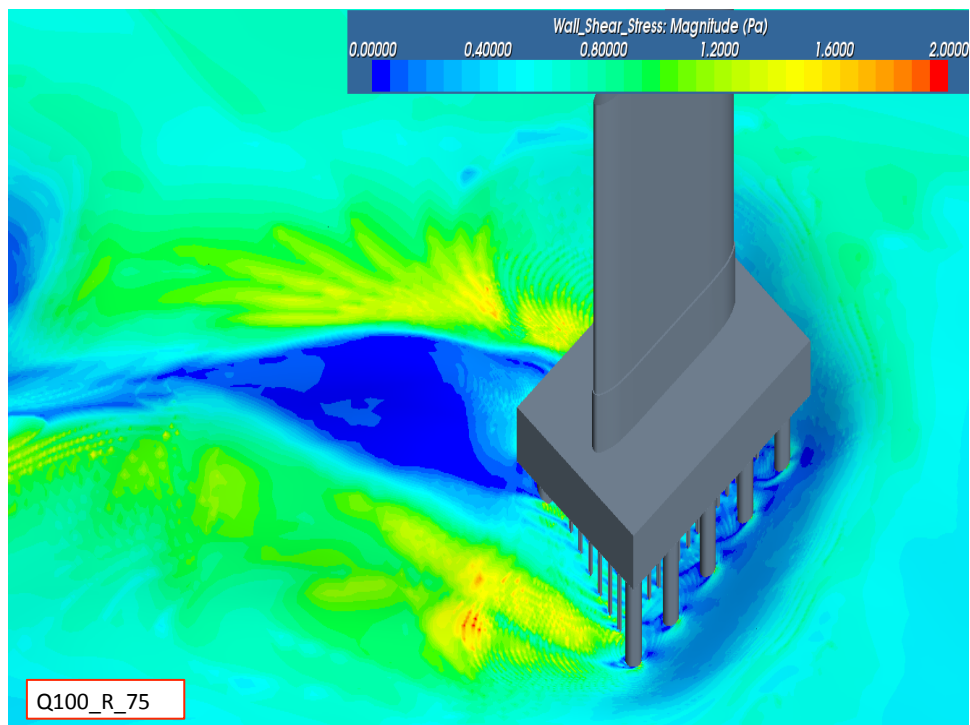
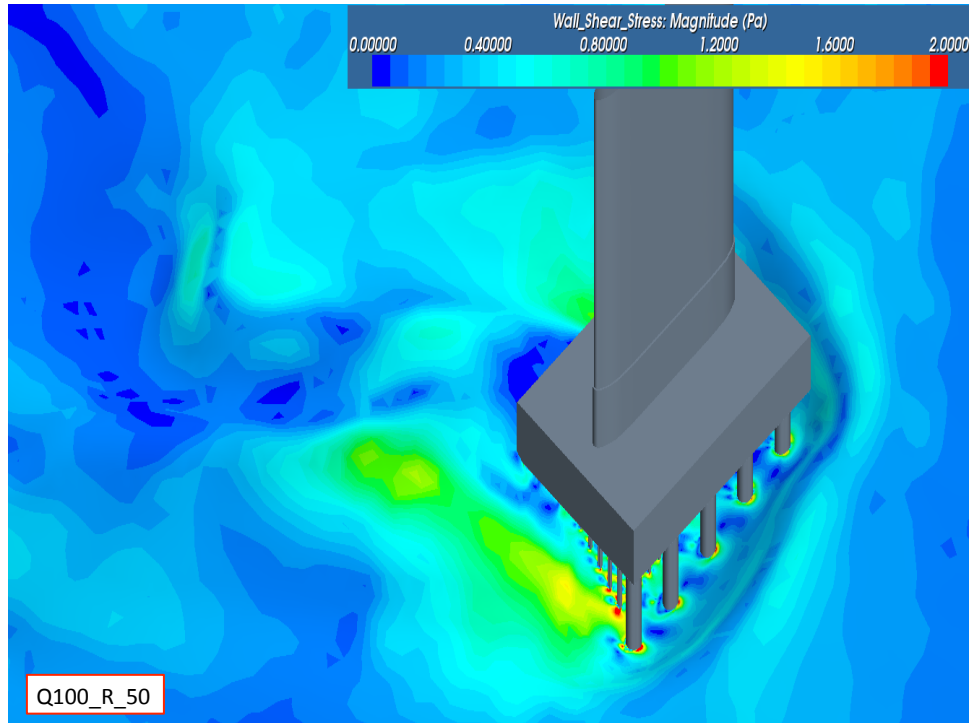


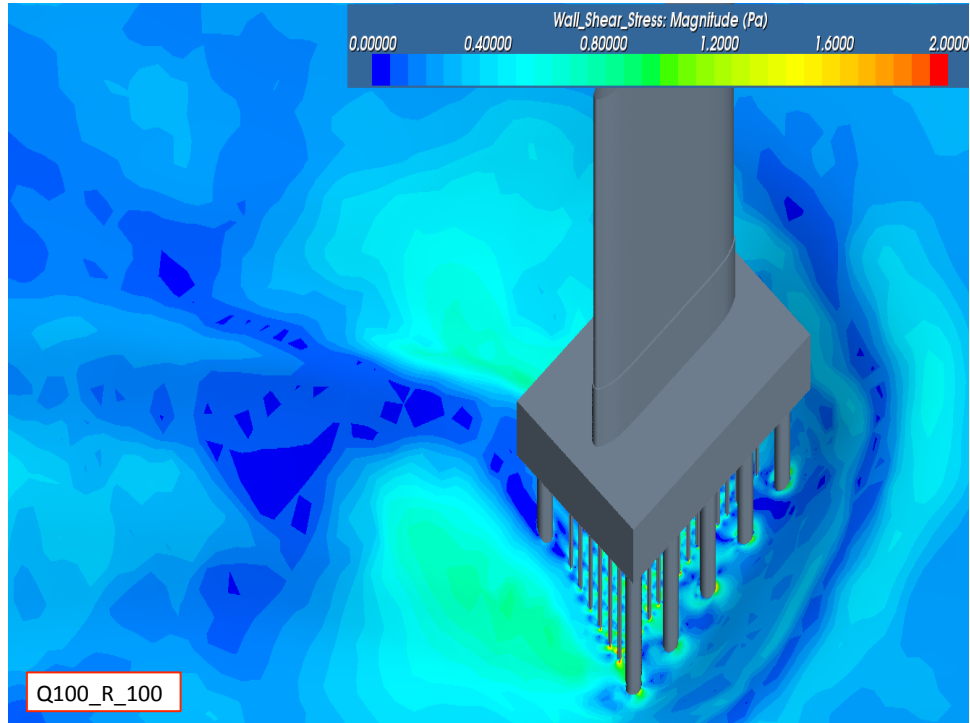




Wall shear stress distributions around the retrofitted pier under the flow condition of the
flood event
(Cases in Group Q100_R)







Glossary

$ A $	=	Area of mesh cell;
a	=	Width of the pier node
dA	=	Area vector;
d_{50}	=	Mean diameter of sediment;
d_*	=	Dimensionless diameter;
D_M	=	Model flow depth;
D_P	=	Prototypic flow depth;
Fr	=	Froude number;
f	=	Darcy friction factor
g	=	Gravitational acceleration;
h	=	Height of the first cell on the bathymetry;
K_1	=	Correction factor of pier nose shape;
K_2	=	Correction factor of water flow;
K_3	=	Correction factor of bed condition;
L	=	Length of the pier;
P	=	Stream power;
P_a	=	Approach stream power
Q_M	=	Model flow rate;
Q_P	=	Prototypic flow rate;
R_h	=	Hydraulic radius;
\bar{U}	=	Average velocity;

U_{∞}	=	Average inlet velocity;
V_M	=	Model average velocity;
V_P	=	Prototypic average velocity;
y	=	Water depth;
y_s	=	Scour depth;
y^+	=	Dimensionless wall distance;
y_{\max}	=	Maximum possible scour depth;
ϵ	=	Average rate of dissipation;
τ	=	Stress tensor on the wall;
τ_a	=	Approach wall shear stress;
τ_c	=	Critical shear stress;
τ_w	=	Local wall shear stress;
η	=	Smallest eddy length;
θ	=	Attack angle;
λ	=	Length scale factor;
μ	=	Dynamic viscosity;
ν	=	Kinetic viscosity of water;
ρ	=	Density of water;
ρ_s	=	Density of sediment;